

SCUOLA DI SCIENZE

Dipartimento di Chimica Industriale "Toso Montanari"

Corso di Laurea Magistrale in

## **Chimica Industriale**

Classe LM-71 - Scienze e Tecnologie della Chimica Industriale

# **Synthesis, Characterization, and Applications of a Novel Cu(II)-MOF Based on a Propargylcarbamate-Functionalized Isophthalate Ligand**

Tesi di laurea sperimentale

### **CANDIDATO**

Riccardo Castagnoli

### **RELATORE**

**Prof.** Daniele Nanni

### **CORRELATORE**

**Prof.ssa** Maria Cristina Cassani

**Prof.ssa** Barbara Ballarin

**Dott.ssa** Francesca Gambassi



## ABSTRACT

This work describes the synthesis of a propargylcarbamate-functionalized isophthalate ligand and its use in the solvothermal preparation of a new copper(II)-based metal organic framework named [Cu(1,3-YBDC)] $\cdot$  $x$ H<sub>2</sub>O (also abbreviated as Cu-MOF).

The characterization of this compound was performed using several complementary techniques such as infrared (ATR-FTIR) and Raman spectroscopy, X-ray powder diffraction spectroscopy (PXRD), scanning electron microscopy (SEM), X-ray photoelectron spectroscopy (XPS), atomic absorption spectroscopy (AAS) as well as thermal and surface area measurements. Synchrotron X-ray diffraction analysis revealed that this MOF contains a complex network of 5-substituted isophthalate anions bound to Cu(II) centers, arranged in pairs within paddlewheel (or “Chinese lantern”) structure with a short Cu–Cu distance of 2.633 Å. Quite unexpectedly, the apical atom in the paddlewheel structure belongs to the carbamate carbonyl oxygen atom. Such extra coordination by the propargylcarbamate groups drastically reduces the MOF porosity, a feature that was also confirmed by BET measurements. Indeed, its surface area was determined to be low ( $14.5 \pm 0.8$  m<sup>2</sup>/g) as its total pore volume (46 mm<sup>3</sup>/g).

Successively the Cu-MOF was treated with H<sub>2</sub>AuCl<sub>4</sub> with the aim of studying the ability of the propargylcarbamate functionality to capture the Au(III) ion and reduce it to Au(0) to give gold nanoparticles (AuNPs). The overall amount of gold retained by the Cu-MOF/Au was determined by AAS while the amount of gold and its oxidation state on the surface of the MOF was studied by XPS.

A glassy carbon (GC) electrode was drop-casted with a Cu-MOF suspension to electrochemically characterize the material through cyclic voltammetry (CV) and electrochemical impedance spectroscopy (EIS). The performance of the modified electrodes towards nitrite oxidation was tested by CV and chronoamperometry. Because of the low surface area and semiconductor behavior of the Cu-MOF, the electrode coated with it showed a worse nitrite sensing performance than that of a bare GC electrode. Upon electrodeposition of AuNPs on the modified electrode, the sensibility and limit of detection towards nitrite was improved beyond that of the GC electrode.



## INDEX

<b>CHAPTER 1</b>	1
<b>1. INTRODUCTION</b>	1
<b>1.1 Context of the work</b>	1
<b>1.2 Objectives</b>	2
<b>1.3 Introduction to Metal Organic Frameworks (MOFs)</b>	4
<b>1.3.1 Definition</b>	4
<b>1.3.2 Brief history</b>	4
<b>1.3.3 The linker-metal bond and framework structure</b>	5
<b>1.4 Stability of MOFs</b>	7
<b>1.4.1 Chemical stability</b>	7
<b>1.4.2 Thermal stability</b>	8
<b>1.4.3 Mechanical stability</b>	8
<b>1.5 Methods of synthesis</b>	9
<b>1.5.1 Solvothermal synthesis</b>	9
<b>1.5.2 Microwave-assisted synthesis</b>	9
<b>1.5.3 Solvent-free mechanochemical synthesis</b>	9
<b>1.5.4 Interfacial synthesis</b>	10
<b>1.5.5 Sonochemical synthesis</b>	10
<b>1.6 Activation of MOFs</b>	11
<b>1.6.1 Thermal activation</b>	12
<b>1.6.2 Supercritical CO<sub>2</sub> drying</b>	12
<b>1.6.3 Freeze drying</b>	13
<b>1.7 Au nanoparticles</b>	14
<b>1.7.1 AuNPs catalytic activity</b>	14
<b>1.7.3 AuNPs stability</b>	15
<b>1.7.4 AuNPs synthesis and stabilization</b>	15
<b>1.8 MOF-based electrochemical sensors</b>	17
<b>1.8.1 Introduction</b>	17
<b>1.8.2 MOF-based nitrite sensors</b>	18
<b>CHAPTER 2</b>	20
<b>2 EXPERIMENTAL</b>	20
<b>2.1 Materials</b>	20
<b>2.2 Instrumentation</b>	20
<b>2.3 Linker synthesis</b>	24

2.3.1 Step 1: Synthesis of prop-2-yn-1-yl <i>N</i> -(2-bromoethyl)carbamate (3)	24
2.3.2 Step 2: Synthesis of dimethyl 5-(2-{{(prop-2-yn-1-yloxy)carbonyl}amino}ethoxy) isophthalate (1,3-Me <sub>2</sub> YBDC) (5)	26
2.3.3 Step 3: Synthesis of 5-(2-{{(prop-2-yn-1-yloxy)carbonyl}amino}ethoxy)isophthalic acid (1,3-H <sub>2</sub> YBDC) (6)	29
2.3.4 Step 4: 1,3-H <sub>2</sub> YBDC crystallization	30
2.3.5 Synthesis of [Et <sub>3</sub> NH] <sub>2</sub> [1,3-YBDC]	30
2.4 Synthesis of [Cu(1,3-YBDC)]·xH <sub>2</sub> O	31
2.4.1 Solvothermal synthesis of [Cu(1,3-YBDC)]·xH <sub>2</sub> O in 2-propanol, 24 h	31
2.4.4 Synthesis of [Cu(1,3-YBDC)]·xH <sub>2</sub> O in ethanol with [NEt <sub>3</sub> ] <sub>2</sub> [1,3-YBDC]	32
2.4.6 Microwave-assisted synthesis of [Cu(1,3-YBDC)]·xH <sub>2</sub> O in 2-propanol	32
2.5 Reactivity of [Cu(1,3-YBDC)]·xH <sub>2</sub> O towards HAuCl <sub>4</sub>	32
2.5.1 MeOH, r.t., 5/10/50/ wt% w <sub>Au</sub> /w <sub>MOF</sub> in air	32
2.5.2 MeOH, 65 °C, 12.2 wt% w <sub>Au</sub> /w <sub>MOF</sub> under N <sub>2</sub>	32
2.5.3 MeOH, 65 °C, 10 wt% w <sub>Au</sub> /w <sub>MOF</sub>	32
2.5.4 Butanol, 118 °C, 10 wt% w <sub>Au</sub> /w <sub>MOF</sub>	33
2.6.1 All in one pot synthesis 1 (AOPS1)	33
2.6.2 All in one pot synthesis 2 (AOPS2)	33
2.7 Electrochemical cell setup	33
2.8 Electrodes modification	34
2.8.1 GC/Cu-MOF	34
2.8.2 GC/Cu-MOF/Au	34
CHAPTER 3	35
3 Linker and [Cu(1,3-YBDC)]·xH <sub>2</sub> O synthesis and characterization	35
3.1 Linker Synthesis and characterization	35
3.3 [Cu(1,3-YBDC)]·xH <sub>2</sub> O synthesis and characterization	42
3.2.1 Optimal reaction conditions screening	42
3.2.2 Vibrational spectroscopy and thermal characterization	45
3.2.3 Crystallochemical analysis	49
3.2.4 SEM-EDX characterization	52
3.2.5 XPS characterization	53
3.2.6 Surface area and porosity	54
CHAPTER 4	56
4.1 Reactivity of [Cu(1,3-YBDC)]·xH <sub>2</sub> O toward Au(III)	56
4.2 All in one pot synthesis	61
CHAPTER 5	65

<b>5 Electrochemical characterization and applications of [Cu(1,3-YBDC)]·xH<sub>2</sub>O</b>	65
<b>5.1 GC/Cu-MOF SEM-EDX</b>	66
<b>5.2 GC/Cu-MOF electrochemical characterization</b>	66
<b>5.3 Nitrite oxidation</b>	71
<b>5.3.1 Nitrite oxidation on a glassy carbon electrode</b>	71
<b>5.3.2 Nitrite oxidation on GC/Cu-MOF and GC/Cu-MOF/Au</b>	73
<b>5.4 EIS characterization</b>	77
<b>5.5 Reproducibility studies</b>	80
<b>5.5.1 Reproducibility on GC/Cu-MOF electrode preparation</b>	80
<b>5.5.2 Reproducibility on GC/Cu-MOF/Au electrode preparation</b>	81
<b>CHAPTER 6</b>	83
<b>6 Conclusions and Future Work</b>	83
<b>BIBLIOGRAPHY</b>	86

# CHAPTER 1

## 1. INTRODUCTION

### 1.1 Context of the work

The research group in which I worked during my internship has shown that a propargylcarbamate [ $-N(H)C(O)OCH_2C\equiv CH$ ] group anchored on different oxide supports ( $SiO_2$ ,  $Al_2O_3$ ,  $TiO_2$ ,  $Fe_3O_4$ ) is capable of straightforwardly reducing  $Au(III)$  to  $Au(0)$ , yielding supported gold nanoparticles (AuNPs) without the addition of any external reducing and/or stabilizing agent (Figure 1.1).<sup>1,2</sup>

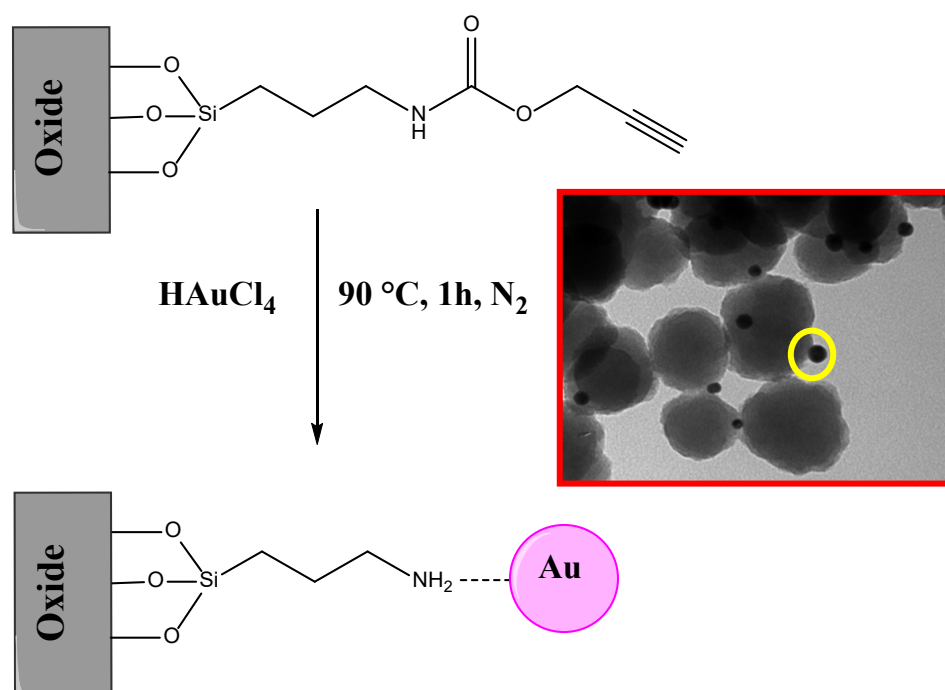


**Figure 1.1:** Alkyne-modified oxide supports and TEM image of AuNPs supported on functionalized Nanosilica.<sup>1</sup>

The first paper<sup>3</sup> reporting the use of this molecule was about functionalization of nanosilica spherical particles (Figure 1.1) and spontaneous reduction of  $Au(III)$  by the alkyl-carbamate group without the use of any other reducing and stabilizing agent. The size of AuNPs synthesized by the functionalized silica is reported to be 11 nm, way lower than the size of AuNPs synthesized using PEI-functionalized silica nanoparticles (40-100 nm).<sup>2</sup> In order to show the higher catalytic activity of AuNPs synthesized using the new molecule supported on silica, the nanomaterial was used as a heterogeneous catalyst for 4-nitrophenol reduction<sup>3</sup> and alkyne hydroamination.<sup>1</sup>

Based on these results the research group envisaged that the versatility demonstrated by the propargylcarbamate residue could be further exploited by anchoring it to different solid supports other than oxides, for example within alkynyl-derivatized MOFs. Indeed, the isolation of a metal-organic framework starting from a suitably functionalized organic linker (Figure 1.2) would ensure an even, dense, and possibly highly symmetric distribution of the reactive alkyne moiety in the material. Additionally, the material porosity and the presence of the metal nodes could affect the reactivity of the alkyne and induce different effects on the ensuing gold nanoparticles, than when the alkyne is attached onto the oxidic surfaces cited above.

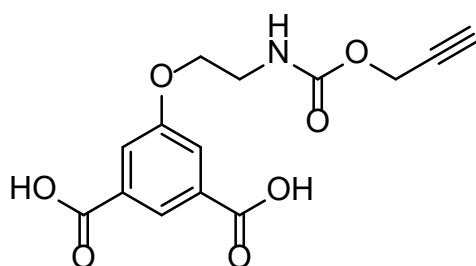


**Figure 1.2:** 1,3-H<sub>2</sub>YBDC.

## 1.2 Objectives

The aim of this work is to show how the linker 1,3-H<sub>2</sub>YBDC and the MOF named [Cu(1,3-YBDC)]·xH<sub>2</sub>O were synthesized, focusing on chemical and electro-chemical characterization of the material. The characterization of this compound was performed using several complementary techniques such as infrared (ATR-FTIR) and Raman spectroscopy, X-ray powder diffraction spectroscopy (PXRD), scanning electron microscopy (SEM), X-ray photoelectron spectroscopy (XPS), atomic absorption spectroscopy (AAS), as well as thermal and surface area measurements.

Successively, the Cu-MOF was treated with HAuCl<sub>4</sub> in order to study the ability of the propargylcarbamate functionality to capture and reduce the Au(III) ion. The overall amount of gold retained by the Cu-MOF/Au was determined through AAS while the amount of gold and its oxidation state on the surface of the MOF was studied by XPS.

A glassy carbon electrode was modified with the Cu-MOF with the purpose to evaluate the nitrite sensing capabilities of the modified electrode. The electro-chemical characterization of the newly synthesized MOF was performed using cyclic voltammetry

(CV) and electrochemical impedance spectroscopy (EIS) while its performance toward nitrite oxidation was evaluated through cyclic voltammetry (CV) and chronoamperometry.

## 1.3 Introduction to Metal Organic Frameworks (MOFs)

### 1.3.1 Definition

Metal Organic Frameworks are a class of porous, crystalline materials characterized by organic ligands that act as linkers between metal centers (nodes), forming 3D structures. Metal centers can be metal ions or metallic clusters.

### 1.3.2 Brief history

The field of MOFs is a relatively young field evolved from coordination chemistry and solid-state/zeolite chemistry.<sup>4</sup> Even if coordination polymers were reviewed for the first time in 1964, the interest in MOFs became popular only in 1990 through the work of Hoskins and Robson (Figure 1.3).<sup>5</sup>

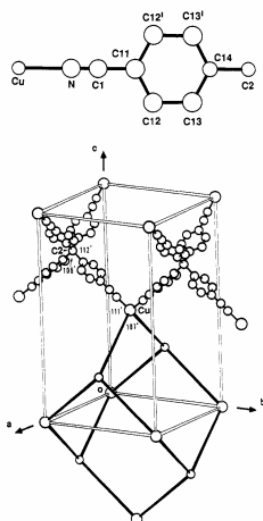


**Figure 1.3:** Structure of  $\text{Cu}^{\text{I}}[4,4',4'',4''',\text{-tetracyanotetraphenylmethane}]_n^{n+}$  framework.<sup>5</sup>

In the paper, the authors suggest that a new class of solid materials, presenting an infinite and ordered framework structure, could form spontaneously from metal centers and rod-like connecting units. They had taken into account the fact that such polymerizing systems could lead to disordered amorphous materials of indefinite composition, but they also stated that the formation of highly ordered self-assembly crystalline structures was probable enough to make some trial synthesis worthwhile. Yaghi et al. popularized the term “MOF” in 1995,<sup>4</sup> and later these materials found applications in gas-sorption, catalysis, electro-catalysis, drug delivery systems and many other fields; confirming the “far-reaching implications” hypothesized by Hoskins and Robson.

### 1.3.3 The linker-metal bond and framework structure

The crystallinity of the structure of MOFs is due to the reversibility of the coordination bonds between organic linkers and metal ions/clusters. This reversibility allows the MOF to achieve a highly ordered structure over time. Increasing the strength of the metal-linker bond decreases the reversibility of the bond leading to an increase in crystallization difficulty (Figure 1.4).<sup>6</sup>

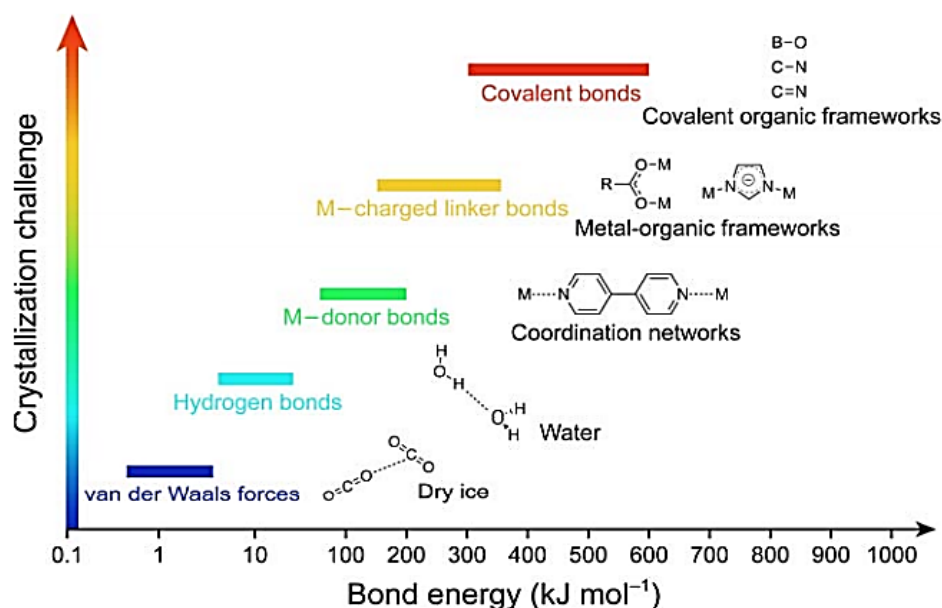
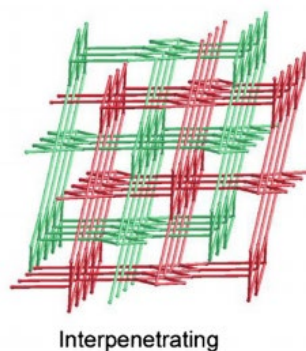


Figure 1.4: Comparison of the strength of different types of interaction.<sup>6</sup>

The most common linkers found in the literature are aromatic amines, ditopic and tritopic carboxylate linkers. The strength of the metal-ligand bond increases with the charge density of the metal cation and the complexing power of the ligand.<sup>7</sup> The use of cations in a high oxidation state and poly-dentate ligand leads to the formation of highly stable MOFs. Anionic linkers offer different advantages over neutral donor linkers: (i) charge neutralization of the metal center, allowing for the formation of neutral frameworks and avoiding the need for counter-ions to be incorporated inside the structure; (ii) stronger bonds between metal centers and linkers, increasing mechanical and chemical stability.<sup>6</sup> Chelating linkers provide more structural rigidity and directionality.

The linkage between metal centers and organic linkers can lead to the formation of a framework with open spaces. These open spaces can form pores, or they can be filled with another framework with identical composition and topology. This phenomenon is called interpenetration (Figure 1.5). The interpenetrating frameworks are mechanically entangled rather than chemically linked.<sup>8</sup> Interpenetration is very common when using long flexible

linkers. While interpenetration increases the density and mechanical properties of the material, it also negatively affects porosity and surface area. For this reason, interpenetration is, for the vast majority of applications, something to be avoided.<sup>9</sup> On the basis of the same reaction starting materials, high temperature, high concentration of reactants and long reaction time promote interpenetration.<sup>9</sup>



**Figure 1.5:** Two interpenetrating frameworks.<sup>9</sup>

The greatest advantage of MOFs compared to other solid crystalline materials is the tunability of their structure and properties. Different ligands, different metal centers and even different preparation methods can produce MOFs with different structures, pore sizes and pore morphology. For example, as reported by Gokhan Barin et al., the field transitioned from using simple symmetrical linkers to extended linkers in order to achieve higher surface area and pore volumes increasing the gas storage capability of the material.<sup>10</sup> They also show how co-crystallizing different linkers can introduce new functional groups inside the MOF, hence altering the pore environment as a result of linker fragmentation (Figure 1.6).

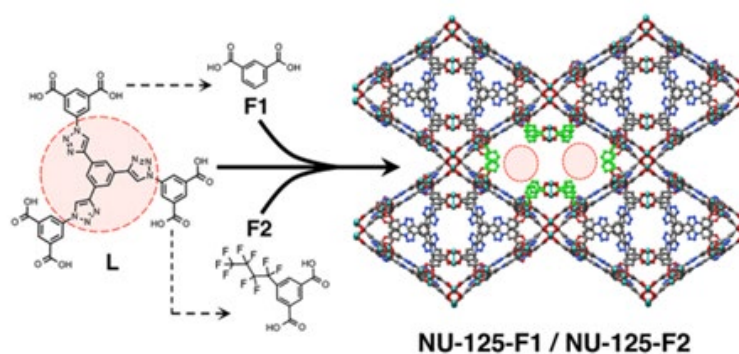


**Figure 1.6** Mixed linker MOF NU-125-F1/NU-125-F2.<sup>10</sup>

## 1.4 Stability of MOFs

### 1.4.1 Chemical stability

Chemical stability is often a huge limitation for MOFs applications. Of the thousands of different structures reported to date, only a limited number of them shows promising properties outside their mother liquor.<sup>11</sup> For example, Cu<sup>2+</sup> benzene-1,3,5-tricarboxylate, also called HKUST-1 degrades over time in water at room temperature. It is reported that the hydrolysis of the metal-carboxylate bond is driven by the ability of water molecules to access and cluster around the metal-carboxylate sites. The higher is the number of linkers connected to the metallic nodes, the higher is the stability of a carboxylate-based MOF in water. This is because the sites become more saturated and less accessible to water and other guest molecules. For carboxylate-based MOFs, the hydrolysis of the metal-linker bond is led by carboxylate protonation.<sup>12</sup>

Another parameter that affects the chemical stability of MOFs is the linker-metal bond strength. The probability of hydrolysis of the metal-ligand bond is inversely correlated with the strength of the bond between the metallic node and the organic linker (Figure 1.7).<sup>7</sup> To some extent, this concept can be extended to the scission of the metal-ligand bond by other guest molecules (like phosphates, NH<sub>3</sub>, NO<sub>x</sub>, SO<sub>x</sub>, H<sub>2</sub>S, etc.) that can compete with the organic linker for a metal coordination site.

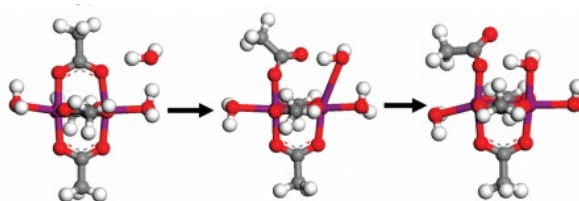


**Figure 1.7:** Simulation of Cu-ligand hydrolysis for HKUST-1.

Colour scheme: red, O; grey, C; white, H; purple, Cu.<sup>7</sup>

A common way to study chemical degradation of a MOF is to perform a powder X-ray diffraction (PXRD) before and after exposure to a given chemical environment paired with an inert gas adsorption isotherm. A loss of porosity will clearly reflect any partial degradation of the crystalline framework.<sup>11</sup>

When discussing about chemical stability of MOFs in water, pH is another important parameter. For carboxylate-based MOFs, low values of pH can lead to the protonation of the carboxylate linker. For copper-based MOFs, high pH values can lead to copper hydroxides and oxides formation.

### **1.4.2 Thermal stability**

The thermal stability of a MOF can be defined as its ability to avoid irreversible changes in its structure due to high temperature exposure. Because post-synthesis thermal treatments are common, the evaluation of the thermal stability of the material has an important role in the design of MOFs. Upon heating, the material can be subject to amorphization, melting, dehydration, linker dehydrogenation or graphitization.<sup>11</sup> The most common methods used to evaluate thermal stability are thermo-gravimetric analysis (TGA) and PXRD performed at different temperatures.

In general, it is reported that MOFs with metal centers in high oxidation states and aromatic organic linkers have higher thermal stability. Carboxylate linkers are subject to decarboxylation and oxidation upon heating, while the less popular sulfate or phosphonate linkers lead to more thermally stable MOFs.<sup>11</sup>

### **1.4.3 Mechanical stability**

The most common mechanical stability issue in MOFs is the amorphization caused by capillary force-driven destruction during guest molecules removal (activation), which leads inevitably to pores collapse and decreased surface area.

The most efficient way to eliminate guest molecules from MOFs without losing porosity is through supercritical processing. Incomplete or failed activation is typically evidenced by discrepancies between the surface areas that are obtained experimentally and surface areas obtained through computational studies based on the structure determined through X-ray spectroscopy.<sup>13</sup> Channels collapse caused by solvent removal or channels blockage caused by the partial retention of the solvent are addressed as the two main reasons of the discrepancies between experimental data and the computational simulations regarding superficial area.

Traditional activation methods consist in heating MOFs under vacuum, while supercritical processing consists in exchanging guest molecules with supercritical CO<sub>2</sub> leading to zero solvent surface tension and thus zero capillary force.<sup>11</sup>

Besides being less prone to interpenetration, MOFs made with aromatic linkers show higher mechanical properties than MOFs made with long and flexible linkers, leading to higher mechanical stability.<sup>11</sup>

## 1.5 Methods of synthesis

### 1.5.1 Solvothermal synthesis

Solvothermal synthesis (Figure 1.8) is the most common way to synthesize MOFs. It is defined as reactions carried inside a closed vessel under autogenous pressure at the boiling point of the solvent. The most important parameters are the concentrations of the reagents and the choice of solvent, that determines the temperature at which the reaction is carried out.<sup>4</sup>

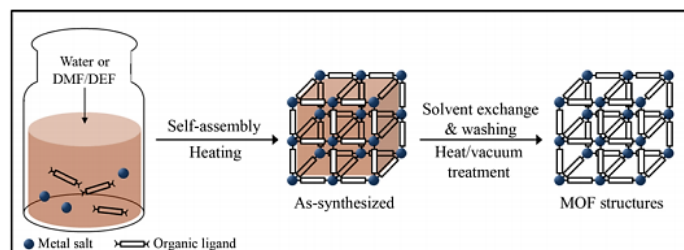


Figure 1.8: Schematic solvothermal synthesis of MOFs.<sup>14</sup>

### 1.5.2 Microwave-assisted synthesis

In this technique (Figure 1.9), the reaction mixture is transferred into a Teflon vessel and heated by microwave radiations.<sup>14</sup> The solvent must have a non-zero dipole moment in order to interact with microwave radiation.

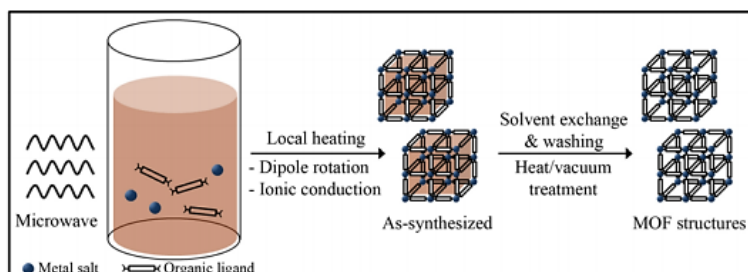


Figure 1.9: Scheme of microwave-assisted MOF synthesis.<sup>14</sup>

The main advantages of this technique are the lower reaction time compared to solvothermal synthesis and the narrow particle size distribution.<sup>14</sup>

### 1.5.3 Solvent-free mechanochemical synthesis

Chemical reactions can be induced by mechanical force as well as many other physical phenomena. The main advantages of mechanochemical synthesis of MOFs are the avoidance of solvent usage and the possibility of conducting the reaction at room temperature.<sup>14</sup>

Grinding time is an important factor that affects the structure of the MOF and its crystallinity. Long grinding times can lead to defects formation, dislocations in crystal

lattices, amorphization and crystalline phase transition.<sup>15</sup> The low predictability of the structure of the products is the greatest disadvantage of this technique.

#### 1.5.4 Interfacial synthesis

The solvothermal method (Figure 1.10) requires a solvent able to solubilize a salt containing the metal ion and the organic linker. Because of the very different nature of these components, it is not always easy to find the right solvent. Rob Ameloot et al.<sup>16</sup> show that the difference in solubility of the organic and inorganic precursors is not always a drawback as it can be used to synthesize thin MOF layers via interfacial synthesis.

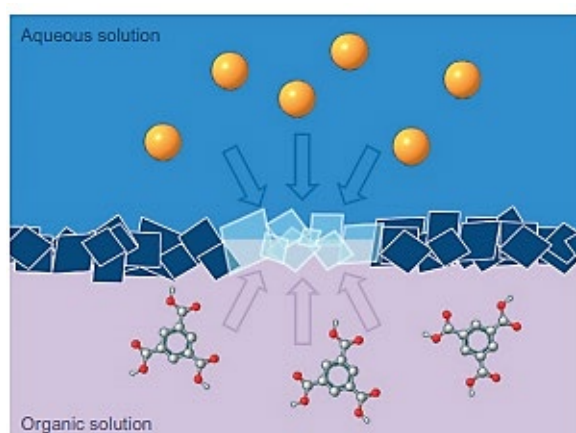


**Figure 1.10:** Interfacial synthesis of MOFs.<sup>16</sup>

Typically, the salt containing the metal cation is solubilized in water while the organic linker is solubilized in an organic solvent immiscible with water. The ligand exchange reaction that leads to the formation of the MOF occurs at the interface between the two phases. This technique is commonly used to fabricate MOF membranes or to obtain single crystals. The growth of the MOF at the interface is dependent on the diffusion rate of the MOF's precursors in the respective solvent, and the diffusion of the precursors at the membrane defects is faster than through the already formed layer.<sup>17</sup> The mechanical strength and flexibility of MOF membranes are generally poor and, at this moment, they do not meet the requirements of stability and durability to be employed in battery fabrication.<sup>17</sup>

#### 1.5.5 Sonochemical synthesis

The sonochemical method (Figure 1.11) is another fast method of MOF preparation. It consists in inserting the reaction mixture inside an ultrasonic bath. The application of ultrasound speeds up the nucleation, shortening the crystallization time and leading to the formation of MOF micro-particles.

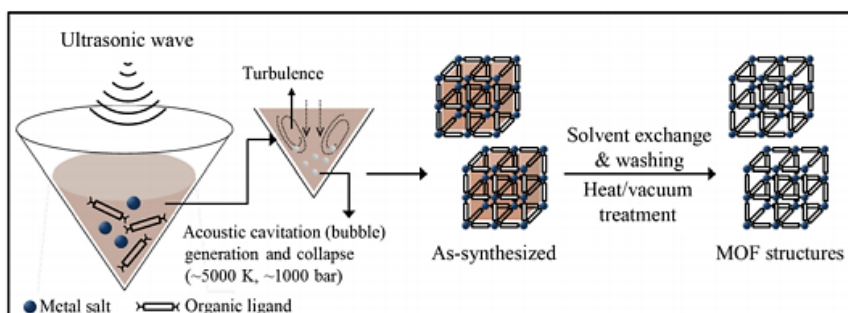


**Figure 1.11:** Schematic of Sonochemical synthesis.<sup>14</sup>

Sonochemical synthesis of MOFs is potentially attractive because of its capability to supply controlled amounts of energy to the reaction mixture through microscopic pressure and temperature fluctuations. Local temperature can raise up to 5000 K and local pressures can raise up to 1000 bar. The very fast heating and cooling rates lead to fine crystallites production.<sup>14,18</sup> It is reported that the porosity and CO<sub>2</sub> uptake of the material is not affected by sonochemical synthesis.<sup>18</sup>

### 1.6 Activation of MOFs

MOFs synthesis under solvothermal conditions leads to the retention of guest molecules, which can lower the surface area and porosity of the material. For this reason, before utilizing the MOF for any application, an activation step is required after the synthesis in order to free porosities from guest molecules (Figure 1.12).

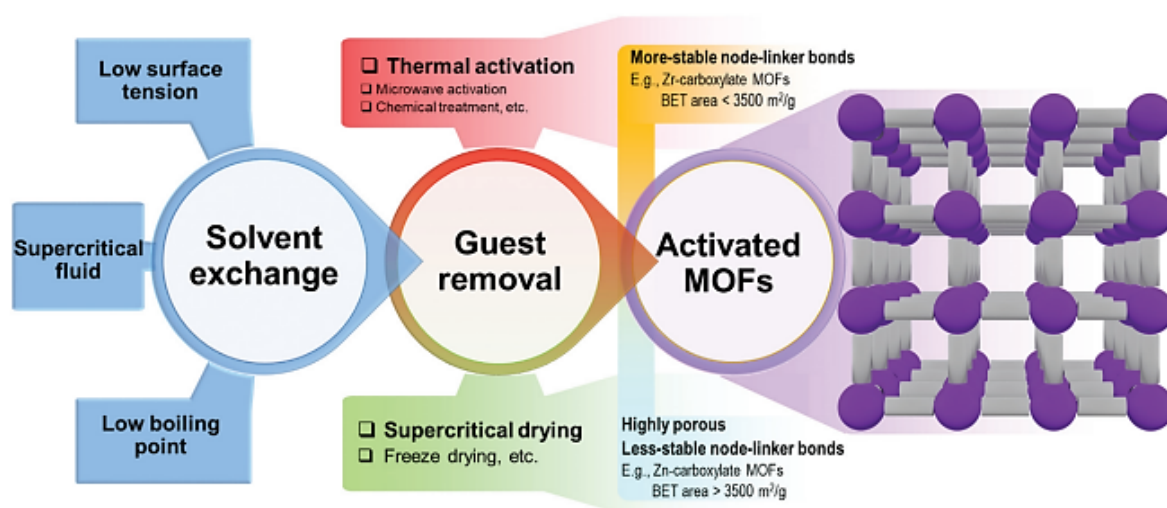


**Figure 1.12:** Overview of the workflow and strategies of MOF activation.<sup>19</sup>

### 1.6.1 Thermal activation

Thermal activation consists in heating the MOF sample under vacuum in order to evaporate the guest molecules. The main disadvantage of this technique is amorphization and pore collapse due to the capillary forces generated by the procedure inside MOF's pores, as described in Section 1.4.3.

To reduce capillary forces and prevent pores to collapse, a solvent-exchange step is usually performed before the thermal activation. This step consists in exposing the MOF to a low boiling solvent that will be exchanged with guest molecules within the MOF.<sup>19</sup> High boiling solvent molecules such as DMF, DMSO and H<sub>2</sub>O are very common as guests inside the MOF's structure as they are typically employed as solvents for the synthesis. The most common solvents with low surface tension and boiling point used for solvent exchange are pentane, fluorocarburi, n-hexane and ethyl acetate.<sup>19</sup>

### 1.6.2 Supercritical CO<sub>2</sub> drying

Supercritical CO<sub>2</sub> is a safe, non-flammable, and inexpensive resource that is used for supercritical extractions and aerogels synthesis. Supercritical activation can be seen as a solvent exchange made with liquid CO<sub>2</sub> instead of low surface tension solvents.

The main advantage of liquid CO<sub>2</sub> as a solvent is that it can be evaporated in its supercritical state. This process prevents pores collapse due to the very low surface tension of liquid CO<sub>2</sub> (Figure 1.13).<sup>19</sup>

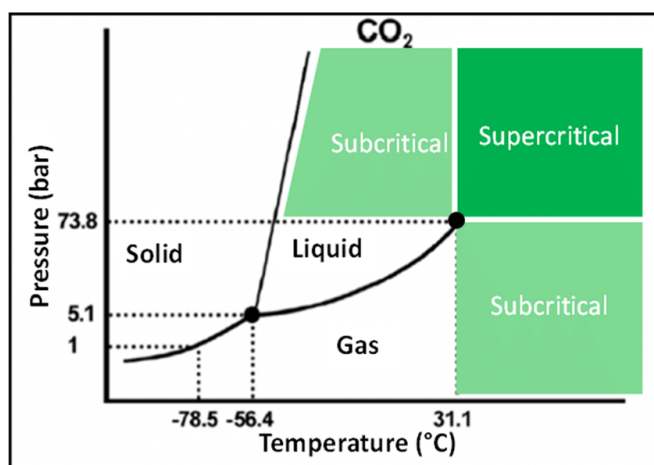


Figure 1.13: state diagram of CO<sub>2</sub>.

In this process, the MOF is exposed to liquid CO<sub>2</sub> below its critical temperature (31 °C) and above its critical pressure (73 bar). The evaporation of CO<sub>2</sub> is performed by heating it above its critical temperature. Usually several cycles of CO<sub>2</sub> exchange are performed and a cycle last

few hours. In the end, the sample is put under vacuum at 50 °C to remove potentially physisorbed CO<sub>2</sub>.<sup>19</sup>

### 1.6.3 Freeze drying

In freeze drying, a solvent exchange is performed using a high-freezing-point solvent, by cooling down the sample in order to freeze it. By putting the sample under vacuum, the frozen solvent is sublimed, effectively avoiding superficial tensions that would occur during liquid-gas transition.<sup>19</sup> A comparison of N<sub>2</sub> isotherms obtained for different activation technique is shown in Figure 1.14.

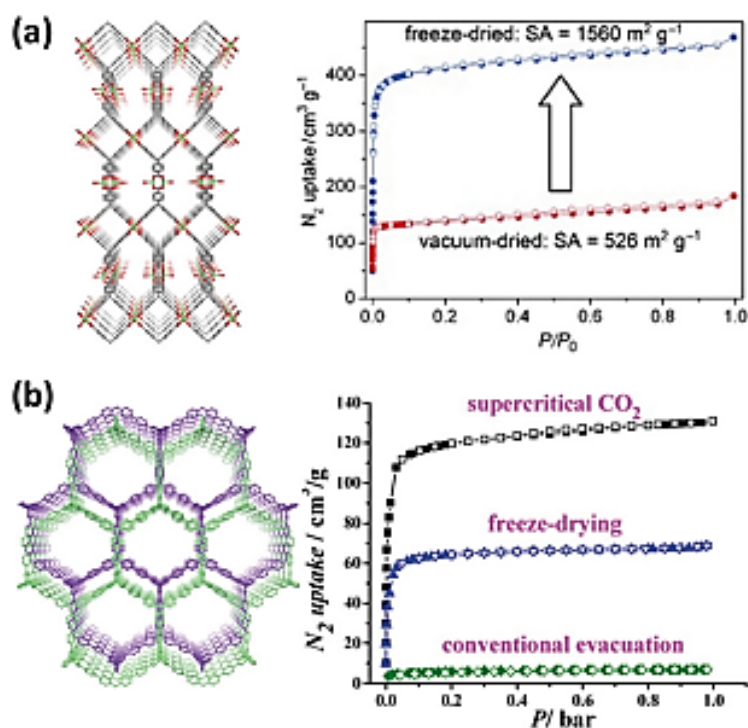


**Figure 1.14:** N<sub>2</sub> absorption isotherms of two Cu-based MOFs activated by different methods.<sup>19</sup>

The most common solvents employed in this activation technique are benzene, with a freezing temperature of 5.5 °C at ambient pressure, and cyclohexane, with a freezing point of 6.5 °C at ambient pressure. Some cases of structural collapse are reported when using benzene because of  $\pi$ - $\pi$  interactions between guest benzene molecules.<sup>19</sup>

## 1.7 Au nanoparticles

### 1.7.1 AuNPs catalytic activity

Due to its electronic configuration  $[\text{Xe}]4f^{14}5d^{10}s^1$ , gold is known to be a very stable metal. Reactants are too weakly adsorbed on bulk gold surface to make it useful for catalysis applications.

The same cannot be said about gold nanoparticles, as the presence of highly uncoordinated atoms on their defective surface is the cause of their high activity.<sup>20</sup> The lower the coordination number of a metal site, the higher is its bonding energy with a reactant. The greater is the number of low-coordination sites on a catalyst particle's surface, the higher is its catalytic activity. Since the number of low coordinated metal sites is a strong function of particle size, the lower the particle size, the higher its catalytic activity (Figure 1.15).<sup>21</sup>

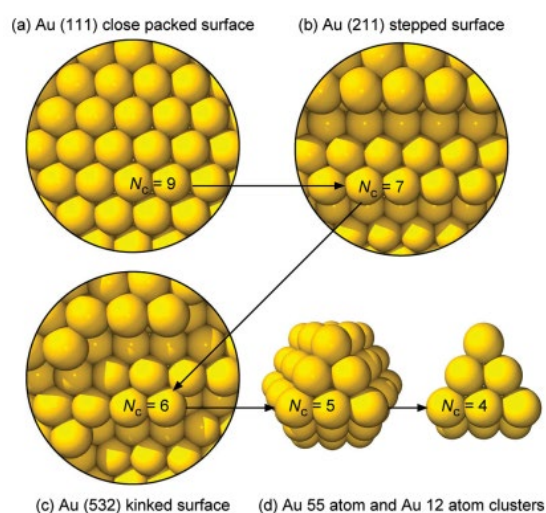


**Figure 1.15:** Structural schematic and lowest coordination number  $N_c$  for the (a) Au (111) close-packed surface, (b) Au (211) stepped surface, (c) Au (532) kinked surface, and (d) Au 55 atom cuboctahedral cluster and Au 12 atom cluster corner model.<sup>21</sup>

### 1.7.2 Colour of solutions containing AuNPs

While the colour of bulk gold is yellow, the colour of AuNPs solutions depends on the average size and shape of the particles (Figure 1.16). This particular property of nanoparticles is caused by a phenomenon called surface plasmon resonance.

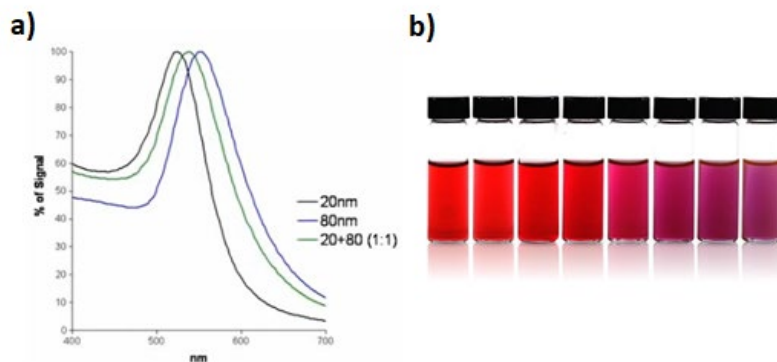


**Figure 1.16:** a) absorbance of different solutions containing AuNPs; b) colour of different solutions containing AuNPs with different size: from lower size to higher.

### 1.7.3 AuNPs stability

Because of the low coordination number of Au atoms on the nanoparticle surface, AuNPs tend to agglomerate in order to increase their stability (Figure 1.17). This phenomenon is also called sintering. The smaller is a particle, the lower its stability. For this reason, small AuNPs are more difficult to obtain and to stabilize, even if they show a higher catalytic activity.

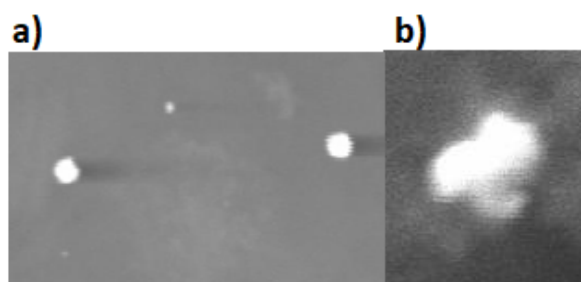


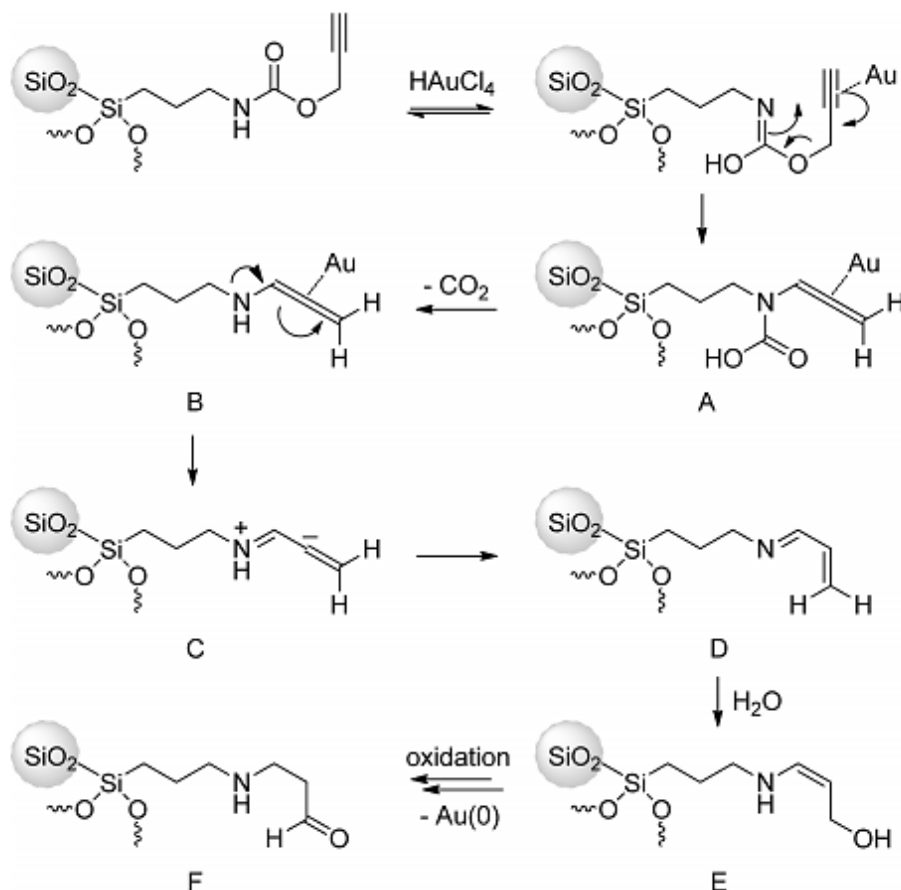
**Figure 1.17:** SEM images of AuNPs on a glassy carbon electrode: a) AuNPs of different sizes, b) AuNPs agglomerate.

Truly naked gold nanoparticles are probably impossible to make, except maybe in the gas phase.<sup>22</sup> The most common ways to stabilize AuNPs, and prevent their aggregation, are to support them on metal oxides or utilizing stabilizer agents, usually polymers, like polyethyleneimine (PEI).

### 1.7.4 AuNPs synthesis and stabilization

AuNPs are commonly synthesized from Au(III) solutions, typically  $\text{HAuCl}_4$ , in the presence of a strong reductant like  $\text{NaBH}_4$  and a stabilizer agent. Because of the high stability of Au(0), it is not uncommon to observe Au(III) reduction by alcohols (especially primary alcohols) or amines in solvothermal conditions.

Although stabilizers have the advantage of stabilizing AuNPs and controlling their size, they bind to low coordination metal sites, reducing their catalytic activity.<sup>23</sup> This is the main drawback of colloidal synthesis of AuNPs. As mentioned in Section 1.1, the group in which I worked during my internship developed a molecule able to reduce and stabilize Au(III) to form AuNPs. The proposed reduction mechanism is shown in Scheme 1.1.



**Scheme 1.1:** Proposed mechanism for the SiO<sub>2</sub>@Yne-mediated reduction of HAuCl<sub>4</sub>.<sup>1</sup>

The affinity of Au(III) for alkyne groups is exploited to coordinate Au(III). The activated alkyne group is exposed to the nucleophilic attack by the carbamic nitrogen in an 1,3-migration reaction. The following decarboxylation and rearrangement reactions lead to the unsaturated imine D. That imine, as well as its hydrolysis products (e.g. E) can act as a reducing agent for Au(III) or Au(I), leading to the formation of stabilized AuNPs.<sup>3</sup>

## 1.8 MOF-based electrochemical sensors

### 1.8.1 Introduction

Metal Organic Frameworks are of great interest for building electrochemical sensing platforms. Due to the high porosity and surface area, MOF films can concentrate analytes near the surface of the electrode amplifying the signal response and improving the detection sensitivity.<sup>24</sup> The particular size and shape of the available channels allows electrodes coated with MOFs to increase their selectivity towards certain analytes in complex matrices due to size exclusion effects. Because MOFs suffer from low conductivity, they are usually modified with highly conductive nanomaterials, like metallic nanoparticles and carbon nanomaterials, in order to increase even further the sensibility of the sensors in which they are employed.<sup>24</sup>

Electrodes are typically coated with MOFs using the drop-casting technique.<sup>25</sup> However, the main problem of this coating method is the progressive exfoliation of the MOF layer from the electrode. This could reduce the reproducibility of the sensor. To prevent this from happening, techniques involving the in-situ growth of MOF layers on the electrode surface were developed in recent years (Figure 1.18).<sup>24</sup>

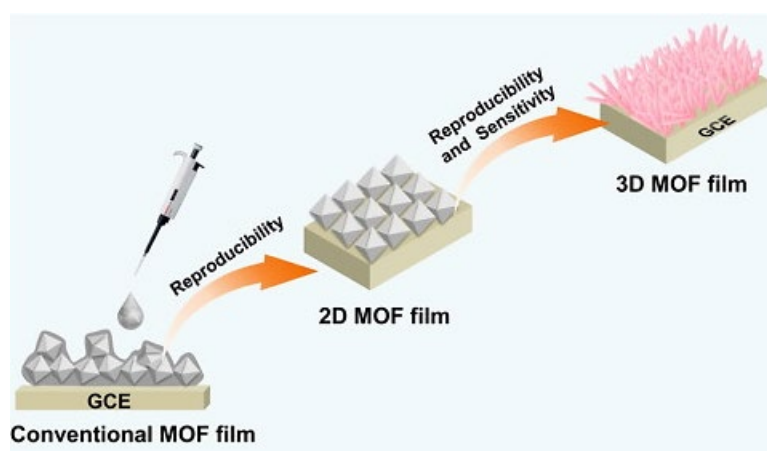


**Figure 1.18:** Strategies to improve the reproducibility of MOF-based electrochemical sensors.<sup>24</sup>

For example, Zhou et al.<sup>26</sup> drop-coated a glassy carbon electrode with carboxylated-graphene and subsequently placed the electrode in the reaction mixture containing the precursors of a Cu-MOF. Using this technique, the MOF layer grows on the electrode surface remaining chemically linked to the carboxylate functionalities of the carboxylated-graphene through their coordination with the metal centres of the forming MOF.

Shahrokhian et al.<sup>27</sup> uniformly coated a glassy carbon electrode with a Cu-MOF based layer. In order to do that, they electrodeposited copper on the electrode surface, then placed

the electrode in an alkaline solution to form copper hydroxides nanotubes from the electrodeposited copper. After putting the electrode in a solution containing the linker, they successfully grew a thin Cu-MOF film on the electrode surface (Figure 1.19).

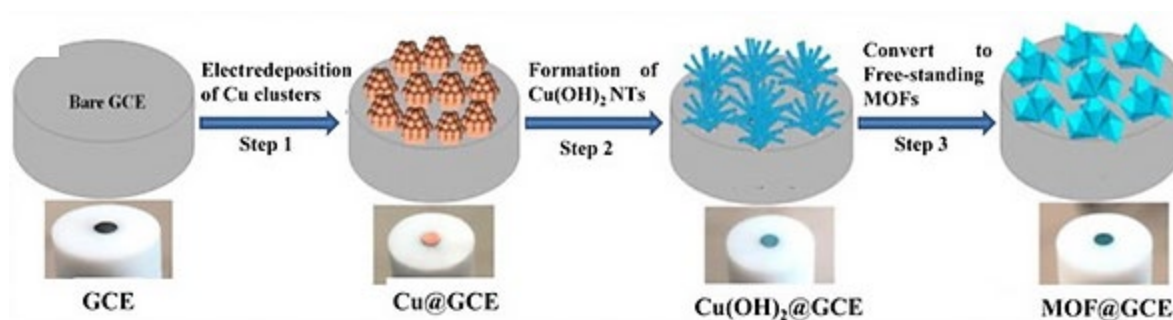
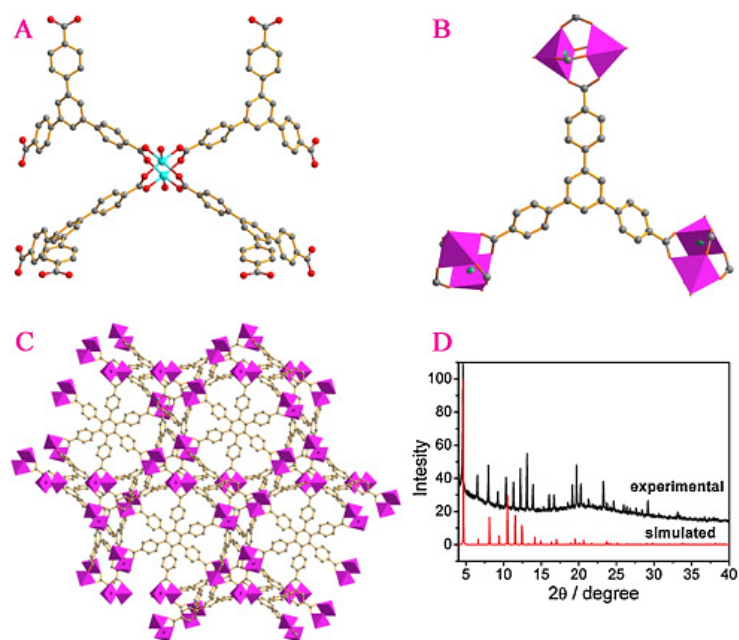


Figure 1.19: Preparation of free standing MOF film on a glassy carbon electrode.<sup>27</sup>

### 1.8.2 MOF-based nitrite sensors

Nitrite comes from nitrogenous organic compounds of animal waste, organic waste, fertilizers, and drinking water.<sup>25</sup> Nitrate and nitrites are also routinely added to meat products as a preservative against food poisoning organisms such as *Clostridium botulinum*.<sup>28</sup> Nitrite is an inorganic pollutant that, upon the interaction with proteins, is able to form carcinogenic *N*-nitrosamines. The dangerousness of these compounds for human health made necessary the development of sensors that can detect the presence of nitrite and quantify its concentration. Nitrite sensors are widely used in food safety supervision.<sup>25</sup>

Glassy carbon electrodes modified with MOFs are widely used as nitrite sensors for their ability to concentrate nitrite in their pores. For example, Yuan et al.<sup>29</sup> modified a carbon paste electrode (CPE) by drop-casting it with stable 3D Cu-based MOF (Figure 1.20) synthesized by a simple solvothermal synthesis.



**Figure 1.20:** Simulated structure of the Cu-MOF used by Yuan et al. for the development of a nitrite sensor.<sup>29</sup>

By testing the performance of the modified electrode through cyclic voltammetry, they found that the deposition of their MOF on a CPE electrode increased its nitrite sensing capability in terms of both oxidation potential and peak current. Through the electrodeposition of AuNPs on the modified electrode they increased even more the performance of the electrode (Figure 1.21).

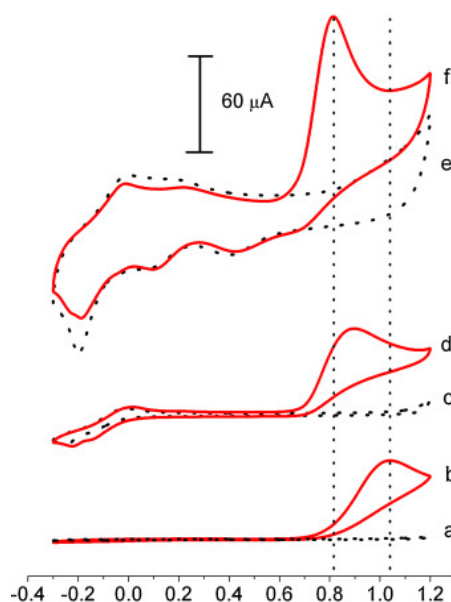


**Figure 1.21:** CVs in PBS 0.1M pH7.2: (a) bare CPE; (b) bare CPE in presence of nitrite 5 mM; (c) CPE/Cu-MOF; (d) CPE/Cu-MOF in presence of nitrite 5 mM; (e) CPE/MOF/Au; (f) CPE/Cu-MOF/Au in presence of nitrite 5 mM.<sup>29</sup>

# CHAPTER 2

## 2 EXPERIMENTAL

### 2.1 Materials

All reagents and solvents were purchased from commercial vendors and used as received; ultrapure water purified with the Milli-Q plus system (Millipore Co, resistivity over 18 M $\Omega$  cm) was used in all cases. The reactions were monitored by thin-layer chromatography (TLC) on highly purified Silica on TLC-PET foils (with fluorescent indicator 254 nm, Fluka). The chemicals 2-bromoethylamine hydrobromide, propargyl chloroformate, dimethyl 5-hydroxyisophthalate, tetrahydrofuran (THF), ethyl acetate, petroleum ether, diethyl ether, butanone, ethanol (EtOH), dichloromethane, deuterated chloroform (CDCl<sub>3</sub>), sulphuric acid (H<sub>2</sub>SO<sub>4</sub>, 98%), hydrochloric acid (HCl, 37 wt%), nitric acid (HNO<sub>3</sub>, 65 wt%), NaHCO<sub>3</sub>, magnesium sulphate, and sodium hydroxide (NaOH, 50 wt%) were purchased from Sigma-Aldrich (analytical reagent grade). H<sub>2</sub>AuCl<sub>4</sub> was synthesized by dissolving a gold wire (BASF, 99.9999%, 1.4 mm diameter) in hot aqua regia.<sup>30</sup>

### 2.2 Instrumentation

ESI-MS analyses were performed by direct injection of methanol solutions using a WATERS ZQ 4000 mass spectrometer; working temperature: 80 ÷ 100 °C; working concentrations: ca. 10<sup>-8</sup> g/L; Cone Voltage: 10 ÷ 30 V; working flow: 10  $\mu$ L/min. The NMR spectra were recorded at 298 K using a Varian MercuryPlus VX 400 (<sup>1</sup>H, 399.9; <sup>13</sup>C, 100.6 MHz); spectra were referenced internally to residual solvent resonances and were recorded at 298 K for characterization purposes; full <sup>1</sup>H and <sup>13</sup>C NMR assignments were done using standard Varian pulse sequences. Spectra have been edited with the software MestReNova Version: 14.1.0-24037, 2019 MestRelab Research S.L. Abbreviations: s = singlet, d = doublet, t = triplet, m = multiplet, bs = broad singlet. ATR-FTIR analyses were performed with a Perkin Elmer Spectrum Two spectrophotometer, equipped with a Universal ATR accessory, in the range 4000-600 cm<sup>-1</sup> with a resolution of 0.5 cm<sup>-1</sup>. The products were directly analysed performing 40 scans. Abbreviations:  $\nu$  = stretching,  $\delta$  = bending. Thermogravimetric analyses were carried out using a Perkin Elmer TGA-7. The samples (ca. 10 mg) were heated in a platinum crucible at a rate of 10 °C min<sup>-1</sup> from 40 °C to 900 °C. Elemental C, H, N analyses were obtained at REDOX s.r.l. (Monza, Italy).

The overall amount of copper present on the different samples was determined by means of flame atomic absorption spectroscopy (AAS, Thermo Scientific iCE 3300

AA01124707) in air-acetylene flame ( $\lambda = 324.8$  nm; spectral bandwidth = 0.5 nm). The analyses were conducted by comparison with five calibration standards (2.0, 4.0, 6.0, 8.0, 10.0 ppm) prepared by dilution to 25 mL of different amounts of a 100 ppm standard solution prepared by diluting 1 mL of *FIXANAL* (03372-1EA Fluka, Copper atomic spectroscopy standard concentrate 10.00 g/L) in 0.5 M HNO<sub>3</sub> (Normatom®, 67-69 %, d = 1.41 g/cm<sup>3</sup>, MW 63.01, VWR Chemicals). The samples were prepared by first heating the solid (5.3 mg) with concentrated nitric acid until complete dissolution and subsequently diluted with HNO<sub>3</sub> 0.5 M up to a volume of 100 mL. The obtained calibration curve is shown in Figure 2.1.

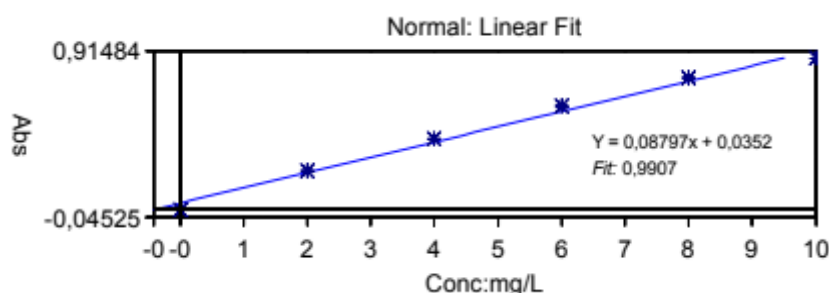


**Figure 2.1:** Cu calibration curve.

The density of the aqueous solution containing the MOF was approximated to 1 g/mL, so that 5.3 mg of MOF were dissolved in 100 g of it. Hence, the concentration of the MOF in the solution was:

$$[MOF] = \frac{0.0053 \text{ g}}{100.0053 \text{ g}} = 5.3 \times 10^{-5} = 53 \text{ ppm}$$

The absorbance of the analysed sample was 0.890. Using the calibration curve in Figure 2.1, the copper concentration was estimated to be 9.714 ppm. For this reason, the copper content inside the MOF was:

$$Cu\% = \frac{9.714 \text{ ppm}}{53 \text{ ppm}} \times 100 = 18.3 \%$$

Being 63.546 g/mol the molecular weight of copper, 305.15 g/mol the molecular weight of 1,3-YBDC and considering the MOF di-hydrate:

$$\frac{MW_{Cu}}{MW_{MOF}} \% = \frac{63.546 \text{ g/mol}}{404.736 \text{ g/mol}} \times 100 = 15.70 \%$$

Since the percentage w/w of copper in the MOF, assuming Cu:1,3-YBDC = 1:1 stoichiometry, is close to the fraction by weight of copper determined by AAS, the stoichiometry is confirmed.

The overall amount of gold present on the different samples was determined by means of flame atomic absorption spectroscopy (AAS, Thermo Scientific iCE 3300 AA01124707) in air-acetylene flame ( $\lambda = 242.8$  nm; spectral bandwidth = 0.5 nm). The analyses were conducted by comparison with six calibration standards (4.4, 6.6, 8.8, 11.0, 13.2, 15.4 ppm) prepared by dilution to 25 mL of different amounts of a 110 ppm standard solution prepared by dissolving 11 mg of a gold wire (BASF, 99.9999%, 1.4 mm diameter) in a minimum amount of aqua regia and then diluted with HCl 0.5 M up to a volume of 100 mL. The samples were prepared by first heating the solid with aqua regia ( $\text{HNO}_3\text{:HCl} = 1\text{:}3$ ) until complete dissolution and subsequently diluted with HCl 0.5 M up to a volume of 100 mL. The obtained calibration curves are shown in Figures 2.2 and 2.3.

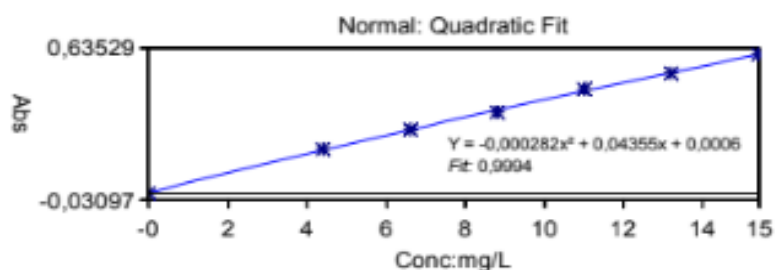


**Figure 2.2:** Au calibration curve 1.

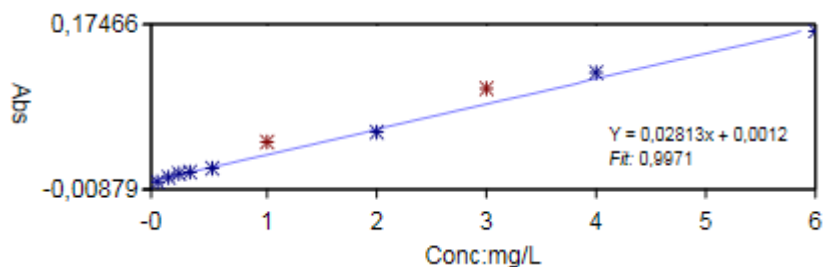


**Figure 2.3:** Au calibration curve 2.

Raman spectra were recorded using a HORIBA Jobin Yvon T64000 spectrometer equipped with three monochromators in double subtractive configuration. The spectrometer was coupled to an Olympus BX40 confocal microscope equipped with 100X, 50X, 20X and 10X objectives, for a lateral resolution lower than 1  $\mu\text{m}$  with the 100X objective. An  $\text{Ar}^+$  laser emitting at 514.5 nm was used in which its output power was limited in order to avoid sample damaging (70-100 mW) and with long times and accumulations (about 50-60 min for spectrum).

Field emission-scanning electron microscopy (FE-SEM) analysis was carried out by means of a Zeiss SUPRA 40VP instrument equipped with an INCAx-act PentaFET Precision

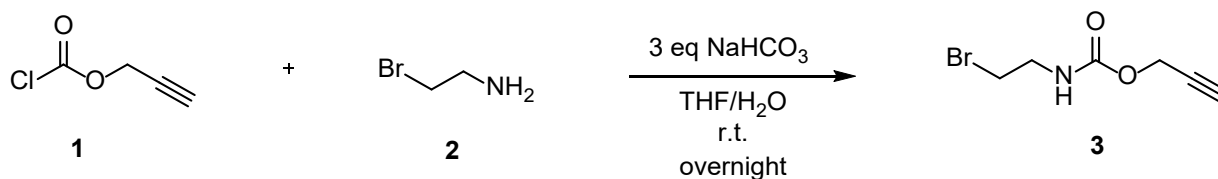
spectrometer (Oxford Instruments) for energy dispersive X-ray spectroscopy (EDXS) characterization. The used primary beam acceleration voltages were comprised between 5 kV (for imaging) and 20 kV (for EDXS analyses). The mean nanoaggregate sizes were evaluated through repeated measurements using the ImageJ<sup>®</sup> software (accessed May 2020). SEM images were obtained at the Department of Chemical Science of Padova University.

X-ray photoelectron (XPS) characterization was performed at the Department of Chemical Science of Padova University using a Perkin-Elmer  $\Phi$  5600-ci instrument, at an operating pressure  $< 10^{-8}$  mbar, using a standard AlK $\alpha$  excitation source ( $h\nu = 1486.6$  eV) and an analysis area with a diameter of 800  $\mu\text{m}$ . Survey scans were acquired in the 0–1300 eV range (187.8 eV pass energy,  $0.8 \text{ eV} \times \text{step}^{-1}$ ,  $0.02 \text{ sec} \times \text{step}^{-1}$ ). Higher resolution scans for the single photopeaks were recorded using the following settings: 58.7 eV pass energy,  $0.1 \text{ eV} \times \text{step}^{-1}$ ,  $0.05 \text{ sec} \times \text{step}^{-1}$ ). Binding energy values (BEs; uncertainty =  $\pm 0.2$  eV) were corrected for charging by assigning to the adventitious C1s peak associated with adventitious hydrocarbons a value of 284.8 eV. After a Shirley-type background subtraction, curve fitting was carried out by the XPS peak software. Atomic percentages (at. %) were evaluated from integrated peak areas using sensitivity factors supplied by Perkin-Elmer.

The adsorption isotherm was measured by using a static volumetric apparatus (ASAP 2020, Micromeritics, USA). The absolute total surface area (SA) of the solid powder ( $>1.5 \text{ m}^2$ ) was above the lowest measurable value ( $0.5 \text{ m}^2$ ). The errors on SA were calculated by standard deviation on 5 consecutive measurements. The sample was degassed at  $1 \times 10^{-3}$  mbar at 323 K for 2 h prior the measurement and after this operation ca. 5% mass loss was observed, in agreement with TGA.

## 2.3 Linker synthesis

### 2.3.1 Step 1: Synthesis of prop-2-yn-1-yl *N*-(2-bromoethyl)carbamate (3)



Scheme 2.1: Synthesis of 3.

To a solution of 2-bromoethylamine hydrobromide (2, 17.8 g, 86.9 mmol) in THF/H<sub>2</sub>O (214 mL/171 mL), cooled to 0 °C, NaHCO<sub>3</sub> (21.9 g, 261 mmol, 3 eq) was added, followed by propargyl chloroformate (1, 10.0 mL, 102.5 mmol, 1.18 eq) added dropwise. The solution was stirred at r.t. overnight. THF was evaporated and the aqueous layer was extracted with ethyl acetate (4 x 20 mL). The organic layer was washed with HCl 1.0 M (2 x 10.0 mL) and brine (2 x 10.0 mL), then dried with MgSO<sub>4</sub>, filtered and concentrated in vacuum to obtain a colourless oil (3, 15.5 g, 75.2 mmol, yield 86.5%). The crude material was used without any further purification. Rf1 = 0.54, Rf2 = 0.12, Rf3 = 0.48 (1:2 petroleum ether/Et<sub>2</sub>O).

ESI-MS(+) (MeOH, m/z): 228 (100) [C<sub>6</sub>H<sub>8</sub>NO<sub>2</sub>Br + Na]<sup>+</sup>.

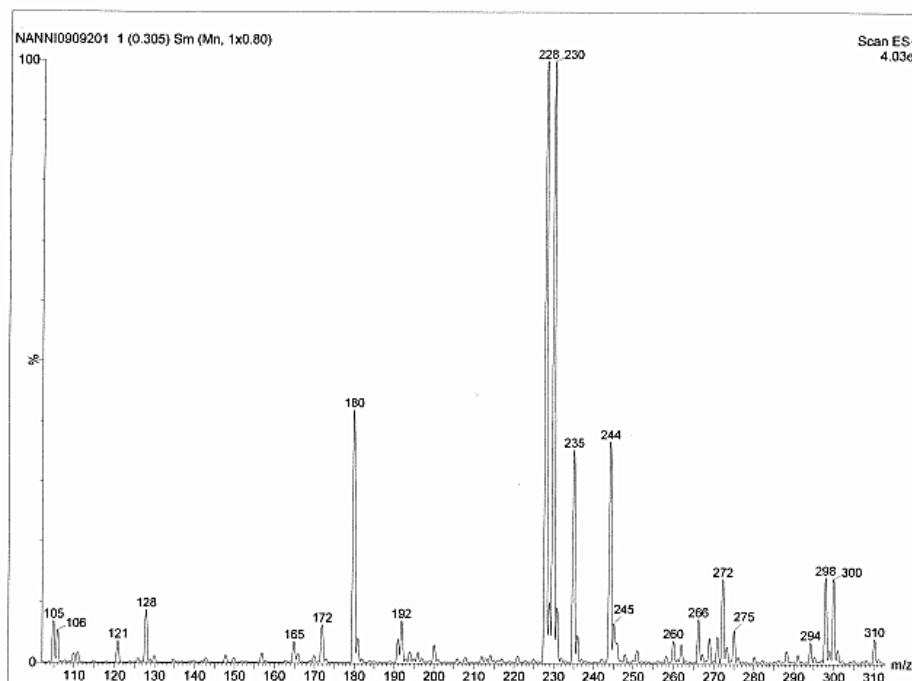
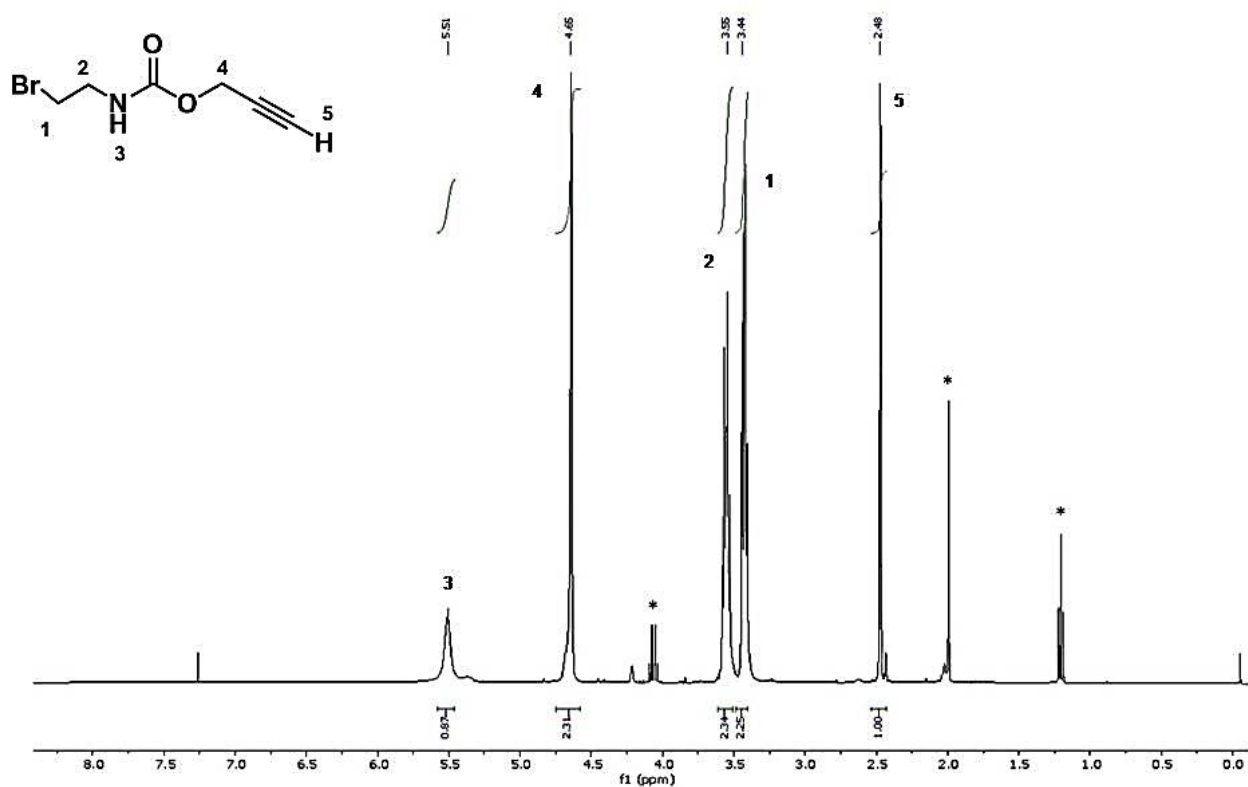


Figure 2.4. ESI-MS(+) spectrum of 3.

**<sup>1</sup>H-NMR (400 MHz, CDCl<sub>3</sub>):** δ 5.51 (bs, 1H, NH<sup>3</sup>), 4.65 (d, <sup>4</sup>J<sub>H,H</sub> = 2.4 Hz, 2H, -OCH<sub>2</sub><sup>4</sup>-), 3.55 (m, 2H, -CH<sub>2</sub><sup>2</sup>N(H)-), 3.44 (t, <sup>3</sup>J<sub>H,H</sub> = 6.2 Hz, 2H, BrCH<sub>2</sub><sup>1</sup>-), 2.48 (t, <sup>4</sup>J<sub>H,H</sub> = 2.4 Hz, 1H, -C≡CH<sup>5</sup>).



**Figure 2.5:** <sup>1</sup>H-NMR spectrum of **3**. Signal labelled with asterisk is relative to the solvent ethyl acetate.

**<sup>13</sup>C-NMR (CDCl<sub>3</sub>, 100.6 MHz):** δ 155.25 (-NHC<sup>3</sup>(O)O-), 77.97 (-C<sup>5</sup>≡CH), 74.82 (-C≡C<sup>6</sup>H), 52.72 (-OC<sup>4</sup>H<sub>2</sub>C≡CH), 42.79 (-C<sup>2</sup>H<sub>2</sub>NH-), 32.22 (BrC<sup>1</sup>H<sub>2</sub>-) ppm.

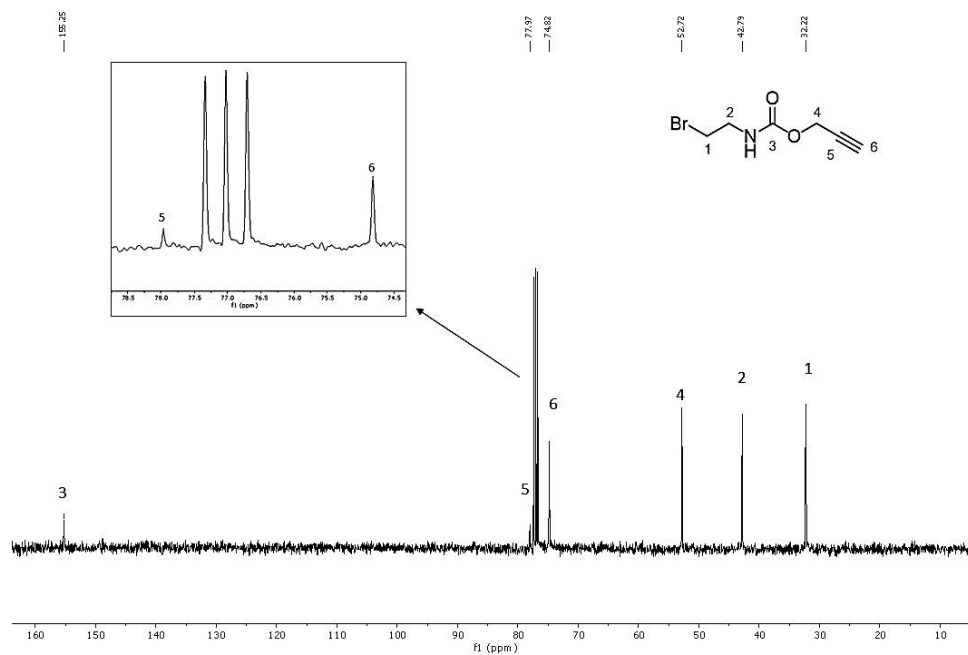


**Figure 2.6:** <sup>13</sup>C-NMR spectrum of **3**.

**ATR-FTIR spectra of neat 3 (cm<sup>-1</sup>):** 3331 (ν NH, m), 3293 (ν ≡C-H, m), 2949 (ν C-H aliphatic, w), 2131 (ν -C≡C-, w), 1703 (ν -C(O)NH- carbamate, s), 1520 (δ NH, s), 1245 (ν C-O, s).

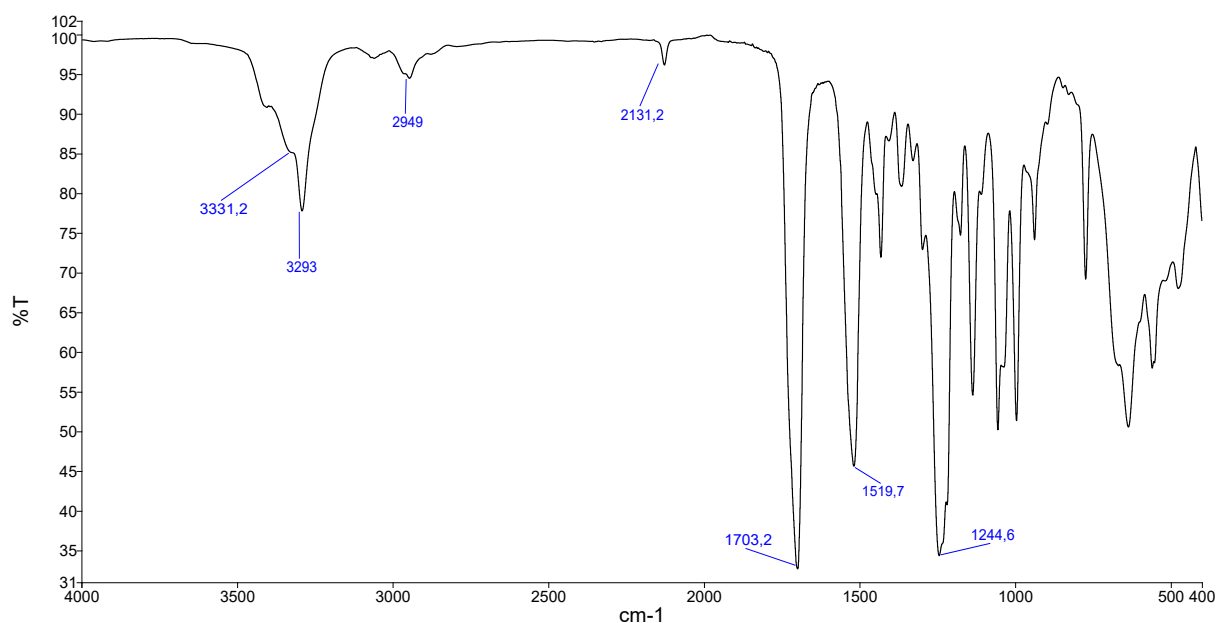
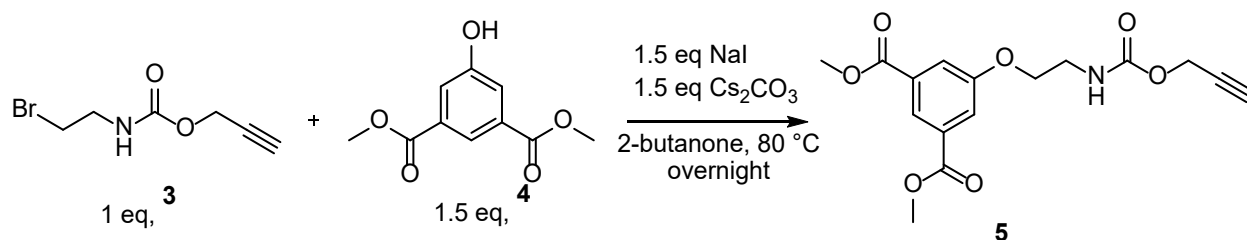


Figure 2.7: IR-ATR spectrum of 3.

### 2.3.2 Step 2: Synthesis of dimethyl 5-(2-((prop-2-yn-1-yloxy)carbonyl)amino)ethoxy isophthalate (1,3-Me<sub>2</sub>YBDC) (5)



Scheme 2.2: Synthesis of 5.

A solution of prop-2-ynyl *N*-(2-bromoethyl)carbamate (3, 3.00 g, 14.6 mmol) in butanone (50 mL) was treated with dimethyl 5-hydroxyisophthalate (4, 4.60 g, 21.9 mmol), NaI (3.28 g, 21.9 mmol), and Cs<sub>2</sub>CO<sub>3</sub> (7.14 g, 21.9 mmol), and the resulting suspension was vigorously stirred at 80 °C overnight. The cooled reaction mixture was first concentrated under vacuum, then diluted with CH<sub>2</sub>Cl<sub>2</sub> (50 mL) and subsequently washed with H<sub>2</sub>O and then with NaOH 10% v/v. After drying the organic phase with MgSO<sub>4</sub>, the solvent was removed to afford 5 as a white solid (4.08 g, 12.19 mmol, yield 83.5%). R<sub>f</sub>3 = 0.48, R<sub>f</sub>4 = 0.30, R<sub>f</sub>5 = 0.20 (1:2 petroleum ether/Et<sub>2</sub>O). M.p. = 99-102 °C. Soluble at r.t. in CHCl<sub>3</sub>, CH<sub>2</sub>Cl<sub>2</sub>, THF, Et<sub>2</sub>O, soluble in boiling methanol, ethanol, and isopropanol.

ESI-MS(+) (MeOH, m/z): 358 (100) [C<sub>16</sub>H<sub>17</sub>NO<sub>7</sub> + Na]<sup>+</sup>.

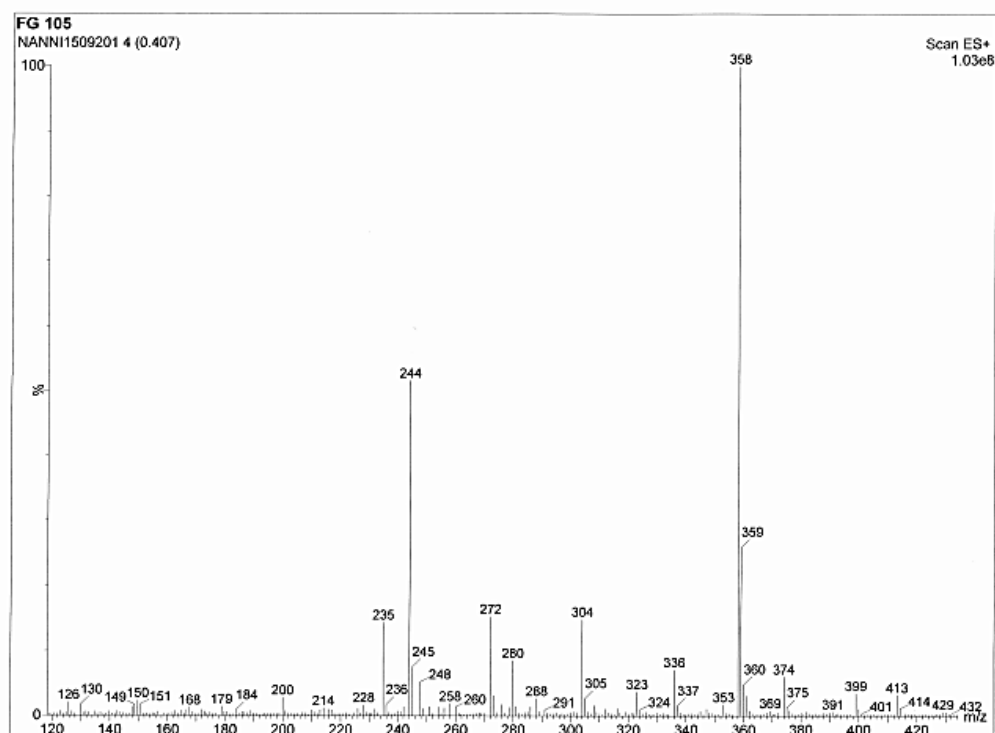


Figure 2.8: ESI-MS(+) spectrum of 5.

<sup>1</sup>H-NMR (CDCl<sub>3</sub>, 399.9 MHz)  $\delta$ : 8.30 (t, <sup>4</sup>J<sub>H,H</sub> = 1.9 Hz, 1H, Ar-H<sup>2</sup>), 7.73 (d, <sup>4</sup>J<sub>H,H</sub> = 1.9 Hz, 2H, Ar-H<sup>3</sup>), 5.24 (bs, 1H, NH<sup>6</sup>), 4.70 (d, <sup>4</sup>J<sub>H,H</sub> = 2.4 Hz, 2H, -OCH<sub>2</sub><sup>7</sup>C $\equiv$ CH), 4.13 (t, <sup>3</sup>J<sub>H,H</sub> = 6.8 Hz, 2H, -OCH<sub>2</sub><sup>4</sup>-), 3.94 (s, 6H, OCH<sub>3</sub><sup>1</sup>), 3.63 (m, 2H, -CH<sub>2</sub><sup>5</sup>NH), 2.47 (t, <sup>4</sup>J<sub>H,H</sub> = 2.4 Hz, 1H, -C $\equiv$ CH<sup>8</sup>).

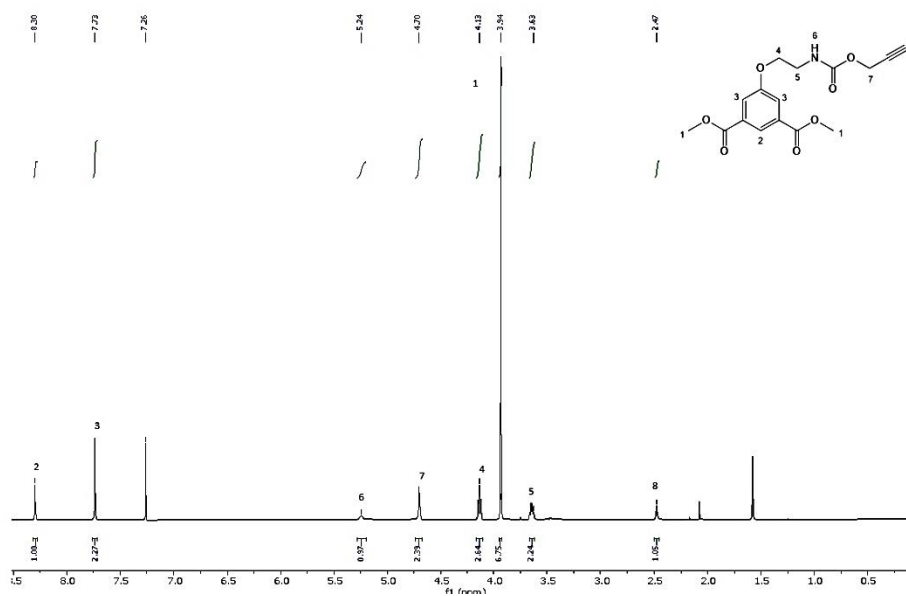
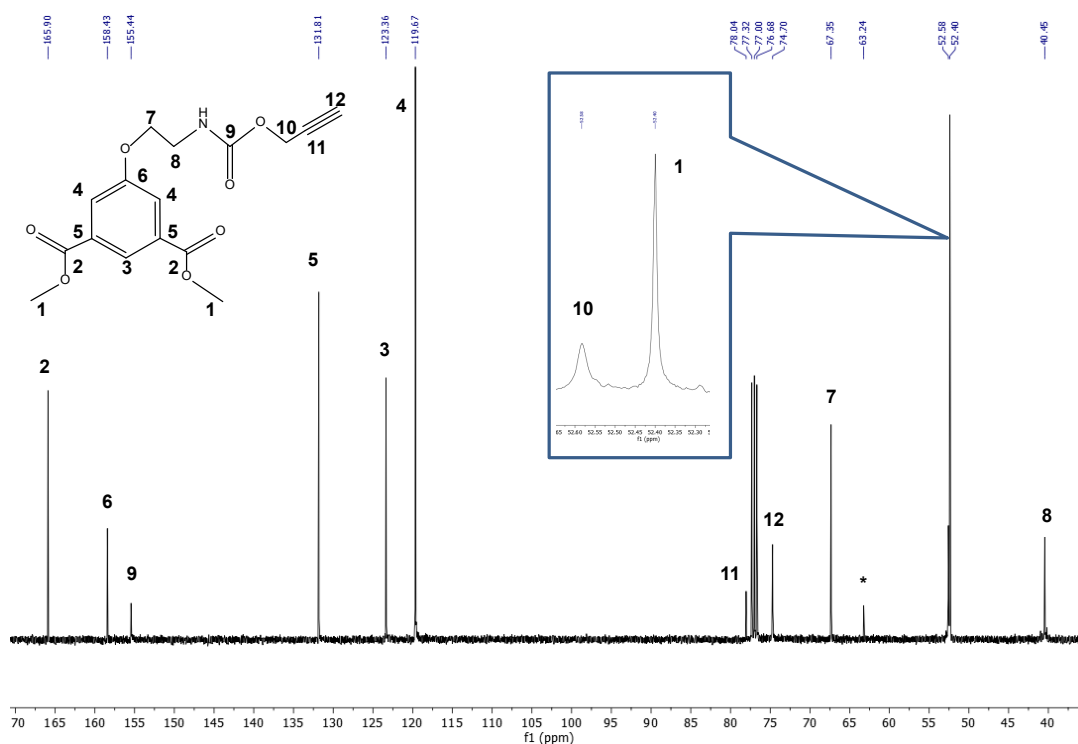


Figure 2.9: <sup>1</sup>H-NMR spectrum of 5.

**$^{13}\text{C}$ -NMR ( $\text{CDCl}_3$ , 100.6 MHz)  $\delta$ :** 165.90 (Ar-C<sup>2</sup>(O)OMe), 158.43 (ArC<sup>6</sup>O-), 155.44 (-N(H)C<sup>9</sup>(O)O-), 131.81 (C<sub>q</sub>, Ar), 123.36 (CH, Ar), 119.67 (CH, Ar), 78.04 (-C<sup>11</sup>≡CH), 74.70 (-C≡C<sup>12</sup>H), 67.35 (-OC<sup>7</sup>H<sub>2</sub>-), 52.58 (-OC<sup>10</sup>H<sub>2</sub>-C≡CH), 52.40 (-OC<sup>1</sup>H<sub>3</sub>), 40.45 (-C<sup>8</sup>H<sub>2</sub>N(H)-) ppm.



**Figure 2.10:**  $^{13}\text{C}$ -NMR spectrum of 5. Signal labelled with an asterisk is relative to a solvent impurity.

**ATR-FTIR spectrum of neat 5 ( $\text{cm}^{-1}$ ):** 3373  $\text{cm}^{-1}$  ( $\nu$  NH, s), 3258 ( $\nu$  ≡C-H, s), 3078 – 2840 ( $\nu$  C-H aliphatic and aromatic, m), 2132 ( $\nu$  -C≡C-, w), 1738 ( $\nu$  -C(O)O- carboxylate, s), 1714 ( $\nu$  -C(O)NH- carbamate, vs), 1544 ( $\delta$  NH, s), 1243 ( $\nu$  C-O, vs).

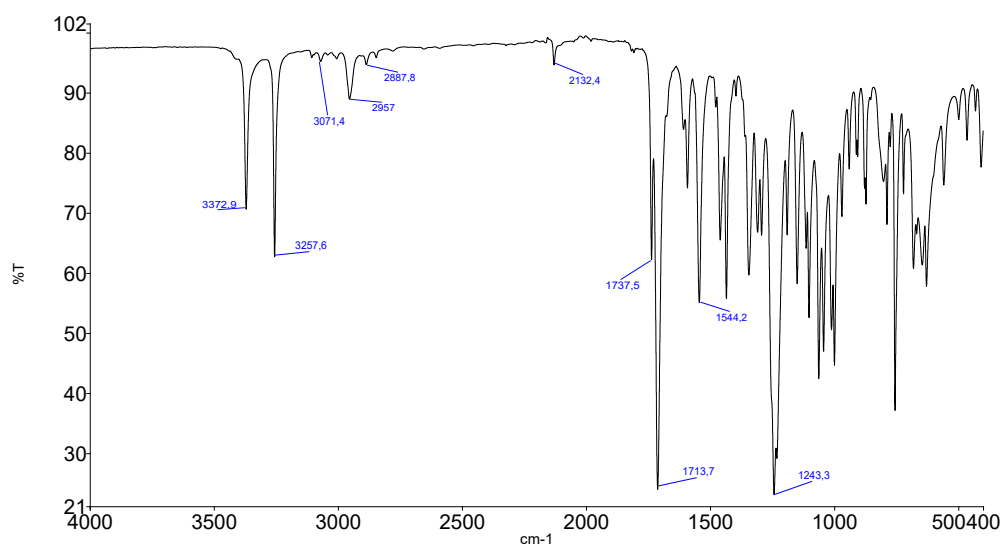
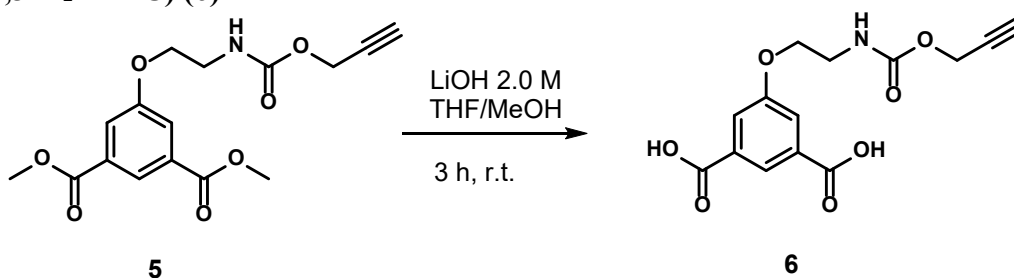


**Figure 2.11:** IR-ATR spectrum of 5.

### 2.3.3 Step 3: Synthesis of 5-(2-(((prop-2-yn-1-yloxy)carbonyl)amino)ethoxy)isophthalic acid (1,3-H<sub>2</sub>YBDC) (**6**)



**Scheme 2.3:** Synthesis of **6**.

Dimethyl 5-(2-(((prop-2-yn-1-yloxy)carbonyl)amino)ethoxy)isophthalate (**5**, 2.42 g, 7.20 mmol) was dissolved in a 1:1 v/v mixture of THF/methanol (60 mL) and treated with 18 mL of 2.0 M aqueous solution of LiOH. After stirring for 3 h, the solvents were evaporated and the residue was treated with 1.0 M aqueous HCl (20 mL) and extracted with ethylacetate. The organic phase was dried with MgSO<sub>4</sub> and evaporated to obtain the pure desired dicarboxylic acid derivative **6** (2.15 g, 7.00 mmol, yield 97%). M.p.= 186-191 °C (215-217 °C after recrystallization). Soluble at r.t. in ethylacetate, DMSO, and acetone; soluble in boiling methanol, ethanol, and isopropanol.

**ESI-MS(+)** (MeOH, *m/z*): 330 (100) [C<sub>14</sub>H<sub>13</sub>NO<sub>7</sub> + Na]<sup>+</sup>, 308(10) [C<sub>14</sub>H<sub>13</sub>NO<sub>7</sub> + H]<sup>+</sup>.

**<sup>1</sup>H-NMR** (acetone-*d*<sub>6</sub>, 399.9 MHz): δ 8.29 (t, <sup>4</sup>J<sub>H,H</sub> = 1.5 Hz, 1H, Ar-H<sup>1</sup>), 7.79 (d, <sup>4</sup>J<sub>H,H</sub> = 1.5 Hz, 2H, Ar-H<sup>2</sup>), 4.67 (d, <sup>4</sup>J<sub>H,H</sub> = 2.4 Hz, 2H, -OCH<sub>2</sub><sup>5</sup>C≡CH), 4.25 (t, <sup>3</sup>J<sub>H,H</sub> = 6.8 Hz, 2H, -OCH<sub>2</sub><sup>3</sup>-), 3.60 (t, <sup>3</sup>J<sub>H,H</sub> = 6.8 Hz, 2H, -CH<sub>2</sub><sup>4</sup>N(H)-), 2.95 (t, <sup>4</sup>J<sub>H,H</sub> = 2.4 Hz, 1H, -C≡CH<sup>6</sup>) ppm.

**<sup>13</sup>C-NMR** (acetone-*d*<sub>6</sub>, 100.6 MHz) δ: 166.73 (ArC<sup>1</sup>(O)OH), 159.99 (Ar-C<sup>5</sup>O-), 157.00 (-N(H)C<sup>8</sup>(O)O), 133.22 (C<sub>q</sub>, Ar), 123.79 (CH, Ar), 120.55 (CH, Ar), 79.73 (-C<sup>10</sup>≡CH), 75.78 (-C≡C<sup>11</sup>H), 68.19 (-OC<sup>6</sup>H<sub>2</sub>-), 52.48 (-OC<sup>9</sup>H<sub>2</sub>-C≡CH), 41.08 (-C<sup>7</sup>H<sub>2</sub>N(H)-) ppm.

**ATR-FTIR spectrum of neat **6** (cm<sup>-1</sup>):** 3336 cm<sup>-1</sup> (ν NH, s), 3304 (ν ≡C-H, s), 3200 – 2800 (ν -OH, broad), 3086-2961 (ν C-H aliphatic and aromatic, m), 2139 (ν -C≡C-, w), 1737 (ν -C(O)O- carboxylate, s), 1687 (ν -C(O)NH- carbamate, vs), 1550 (δ NH, s), 1259 (ν C-O, vs).

### 2.3.4 Step 4: 1,3-H<sub>2</sub>YBDC crystallization

1,3-H<sub>2</sub>YBDC (6, 1.91 g, 5.69 mmol) was dissolved in EtOH (10 mL) at 80 °C. After 1,3-H<sub>2</sub>YBDC solubilisation, water (5 mL) was added to the mixture. During cooling in an ice bath, a white precipitate was observed. The solid was separated by filtration and washed with EtOH. The product was placed under vacuum at r.t overnight, while the mother liquor was placed in a freezer at -11 °C overnight to precipitate more linker. The white solid obtained from the mother liquor was filtered following the same procedure as before. The process was repeated three times, monitoring the melting point of the crystallized 1,3-H<sub>2</sub>YBDC.

### 2.3.5 Synthesis of [Et<sub>3</sub>NH]<sub>2</sub>[1,3-YBDC]

Triethylamine (0.205 mL, 1.48 mmol) was added to 1,3-H<sub>2</sub>YBDC (0.151 g, 0.491 mmol) in ethanol (10 mL) under stirring. After 1 h evaporation of the solvent under reduced pressure gave the triethyl ammonium salt as a pale yellow, viscous oil in quantitative yields. It is partially soluble at r.t. in ethylacetate and acetone, soluble in ethanol and chloroform.

**<sup>1</sup>H-NMR (acetone-*d*<sub>6</sub>, 399.9 MHz):** δ 8.34 (t, <sup>4</sup>J<sub>H,H</sub> = 1.4 Hz, 1H, Ar-H<sup>1</sup>), 7.68 (d, <sup>4</sup>J<sub>H,H</sub> = 1.4 Hz, 2H, Ar-H<sup>2</sup>), 7.00 (brs from NH), 4.67 (d, <sup>4</sup>J<sub>H,H</sub> = 2.5 Hz, 2H, -OCH<sub>2</sub><sup>5</sup>C≡CH), 4.14 (q, <sup>3</sup>J<sub>H,H</sub> = 6.8 Hz, 2H, -OCH<sub>2</sub><sup>3</sup>-), 3.60 (m, , 2H, -CH<sub>2</sub><sup>4</sup>NH-), 3.09 (q, <sup>3</sup>J<sub>H,H</sub> = 7.3 Hz, 10 H, NCH<sub>2</sub>CH<sub>3</sub>), 3.03 (t, <sup>4</sup>J<sub>H,H</sub> = 2.4 Hz, 1H, -C≡CH<sup>6</sup>), 1.25 (t, <sup>3</sup>J<sub>H,H</sub> = 7.3 Hz, 14H, NCH<sub>2</sub>CH<sub>3</sub>) ppm.

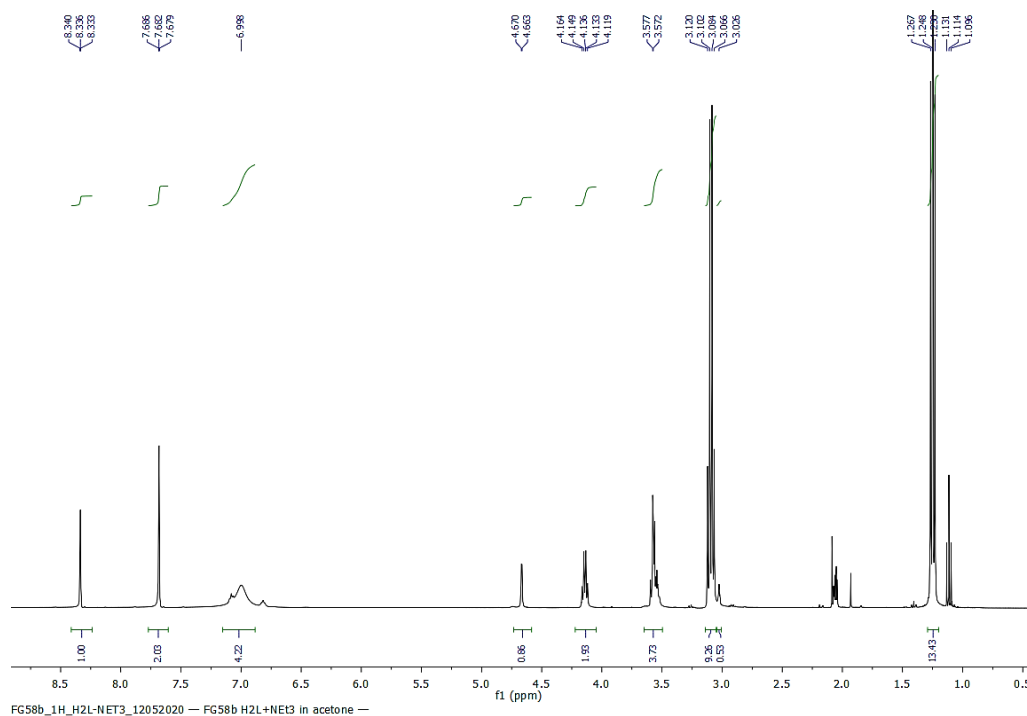
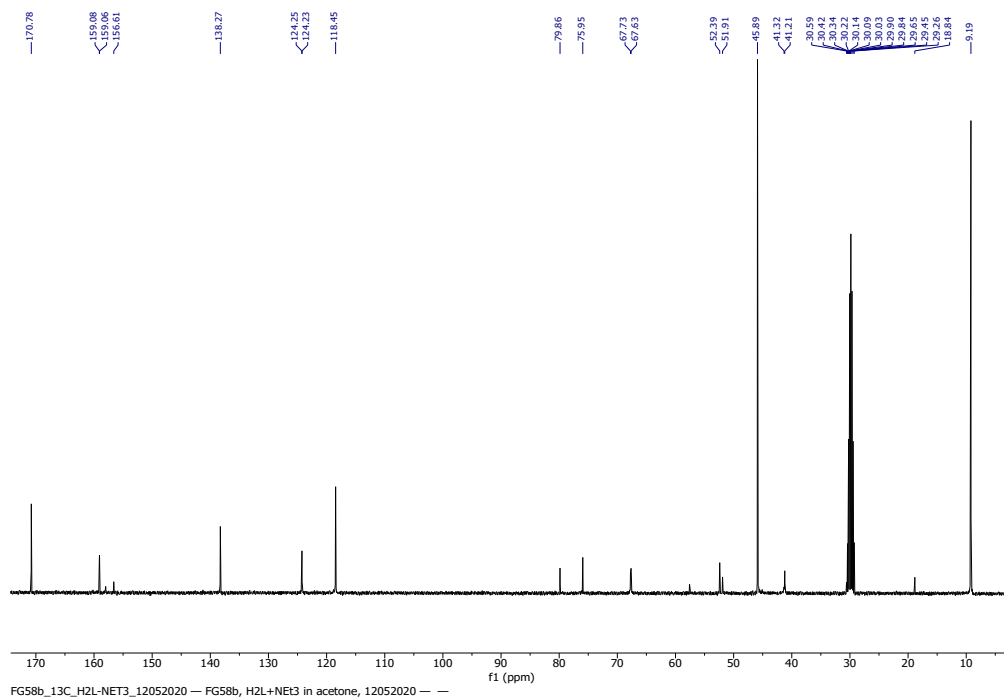


Figure 2.12: <sup>1</sup>H-NMR of [Et<sub>3</sub>NH]<sub>2</sub>[1,3-YBDC].

**$^{13}\text{C}$ -NMR (acetone- $d_6$ , 100.6 MHz)  $\delta$ :** 170.78 (ArC<sup>1</sup>(O)OH), 159.08 (Ar-C<sup>5</sup>O-), 157.6 (-N(H)C<sup>8</sup>(O)O), 138.27 (C<sub>q</sub>, Ar), 124.25 (CH, Ar), 118.45 (CH, Ar), 79.85 (-C<sup>10</sup>≡CH), 75.95 (-C≡C<sup>11</sup>H), 67.63 (-OC<sup>6</sup>H<sub>2</sub>-), 52.39 (-OC<sup>9</sup>H<sub>2</sub>-C≡CH), 45.89 (-NCH<sub>2</sub>CH<sub>3</sub>), 41.32 (-C<sup>7</sup>H<sub>2</sub>N(H)-), 9.19 (-NCH<sub>2</sub>CH<sub>3</sub>) ppm.



**Figure 2.13:**  $^{13}\text{C}$ -NMR of [Et<sub>3</sub>NH]<sub>2</sub>[1,3-YBDC].

## 2.4 Synthesis of [Cu(1,3-YBDC)]·xH<sub>2</sub>O

The synthesis of the Cu-MOF has been carried out under a variety of experimental conditions discussed in detail in Chapter 3.

### 2.4.1 Solvothermal synthesis of [Cu(1,3-YBDC)]·xH<sub>2</sub>O in 2-propanol, 24 h

A suspension of 1,3-H<sub>2</sub>YBDC (0.120 g, 0.390 mmol) and Cu(NO<sub>3</sub>)<sub>2</sub>·2.5H<sub>2</sub>O (0.163 g, 0.701 mmol) in 2-propanol (150 mL) was refluxed under stirring (300 rpm) for 24 h and then cooled to room temperature. The precipitate was collected by Buchner filtration and washed with 2-propanol (2 x 10 mL). The turquoise microcrystalline powder was then dried in an oven at 70 °C for 24 h, successively kept under vacuum (0.02 bar) for 24 h and stored under nitrogen to give 0.142 g of [Cu(1,3-YBDC)]·xH<sub>2</sub>O (yield 90% based on the organic acid and considering the Cu-MOF dihydrate). The reaction can be easily scaled up to produce gram quantities. The elemental analysis of the synthesized sample (C, 42.48; H, 3.59; N, 3.60, Cu, 15.91) is in good agreement with the calculated composition of [Cu(1,3-YBDC)]·2H<sub>2</sub>O (C<sub>14</sub>H<sub>15</sub>NO<sub>9</sub>Cu: C, 41.54; H, 3.73; N, 3.46; Cu, 15.70 %).

#### **2.4.4 Synthesis of [Cu(1,3-YBDC)]·xH<sub>2</sub>O in ethanol with [NEt<sub>3</sub>]<sub>2</sub>[1,3-YBDC]**

A suspension of Cu(NO<sub>3</sub>)<sub>2</sub>·2.5H<sub>2</sub>O (0.110 g, 0.473 mmol) and [NEt<sub>3</sub>]<sub>2</sub>[1,3-YBDC] (0.473 mmol) in ethanol (10 mL) was kept at room temperature under stirring (300 rpm) for 1 h and then cooled to room temperature. The precipitate was collected by Buchner filtration, washed with ethanol (2 x 10 mL), and placed in the oven at 70 °C for 24 h.

#### **2.4.6 Microwave-assisted synthesis of [Cu(1,3-YBDC)]·xH<sub>2</sub>O in 2-propanol**

1,3-H<sub>2</sub>YBDC (0.122 g, 0.397 mmol) and Cu(NO<sub>3</sub>)<sub>2</sub>·2.5H<sub>2</sub>O (0.166 g, 0.715 mmol) were dissolved in 2-propanol (15 mL). The reaction mixture was placed in a Teflon vessel that was inserted in a microwave furnace. The heating was performed through pulsed microwave radiation with a frequency between 0 and 600 Hz that kept the temperature at 105 °C for 1h. The precipitate was collected by Buchner filtration and washed with 2-propanol (2 x 10 mL). The powder obtained was then dried in the oven at 70 °C for 48 h.

#### **2.5 Reactivity of [Cu(1,3-YBDC)]·xH<sub>2</sub>O towards HAuCl<sub>4</sub>**

The Cu-MOF was treated with HAuCl<sub>4</sub> under different reaction conditions described below.

##### **2.5.1 MeOH, r.t., 5/10/50/ wt% w<sub>Au</sub>/w<sub>MOF</sub> in air**

To a suspension of [Cu(1,3-YBDC)]·xH<sub>2</sub>O (0.300 g) in MeOH, different amounts of HAuCl<sub>4</sub>·3H<sub>2</sub>O (0.030/0.060/0.300 g) dissolved in the same solvent were added. The reaction mixture was stirred at r.t. for 72 h in air. The obtained solid was isolated by Buchner filtration and washed with EtOH (2 x 10 mL). Then, the product was dried at 70 °C for 24 h.

##### **2.5.2 MeOH, 65 °C, 12.2 wt% w<sub>Au</sub>/w<sub>MOF</sub> under N<sub>2</sub>**

To a suspension of [Cu(1,3-YBDC)]·xH<sub>2</sub>O (0.300 g) in MeOH, HAuCl<sub>4</sub>·3H<sub>2</sub>O (0.073 g, 0.186 mmol) was added. The reaction mixture was stirred at 65 °C for 24 h under N<sub>2</sub>. The obtained solid was isolated by Buchner filtration and washed with EtOH (2 x 10 mL). Then, the product was dried at 70 °C for 24 h.

##### **2.5.3 MeOH, 65 °C, 10 wt% w<sub>Au</sub>/w<sub>MOF</sub>**

To a suspension of [Cu(1,3-YBDC)]·xH<sub>2</sub>O (0.250 g) in MeOH (120 mL), HAuCl<sub>4</sub>·3H<sub>2</sub>O (0.050 g, 0.127 mmol) was added. The reaction mixture was stirred for 1 h at r.t. and the solid successively was separated from the supernatant by centrifugation at 5400 rpm for 15 min. After three cycles of washings with MeOH (3x20 mL) and centrifugations the product was divided in two parts: one half was placed in MeOH (30 mL) at 65 °C for 1 h under stirring. The second half was placed in MeOH (30 mL) at 65 °C for 24 h under stirring. After that, the solid was again separated by centrifugation and washed with MeOH.

#### **2.5.4 Butanol, 118 °C, 10 wt% w<sub>Au</sub>/w<sub>MOF</sub>**

To a suspension of [Cu(1,3-YBDC)]·xH<sub>2</sub>O (0.250 g) in MeOH (120 mL), H<sub>2</sub>AuCl<sub>4</sub>·3H<sub>2</sub>O (0.050 g, 0.127 mmol) was added. The reaction mixture was stirred for 1 h at r.t. and the solid successively was separated from the supernatant by centrifugation at 5400 rpm for 15 min. After three cycles of washings with MeOH (3x20 mL) and centrifugations the product was divided in two parts: one half was placed in butanol (30 mL) at 118 °C for 24 h under stirring. The second half was placed in butanol (30 mL) at 118 °C for 1 h under stirring. After that, the solid was again separated by centrifugation and washed with MeOH.

### **2.6 All in one pot synthesis**

#### **2.6.1 All in one pot synthesis 1 (AOPS1)**

1,3-H<sub>2</sub>YBDC (0.300 g, 0.97 mmol), Cu(NO<sub>3</sub>)<sub>2</sub>·2.5H<sub>2</sub>O (0.403g, 1.74 mmol), and H<sub>2</sub>AuCl<sub>4</sub>·3H<sub>2</sub>O (0.060g, 0.152 mmol) were dissolved in 2-propanol (150 mL). The reaction mixture was stirred at 83 °C for 24 h. The solid obtained was separated from the supernatant by centrifugation (5400 rpm) for 10 min, washed with 2-propanol and centrifuged again. The material obtained was thermally activated as described in Section 2.4.1.

#### **2.6.2 All in one pot synthesis 2 (AOPS2)**

1,3-H<sub>2</sub>YBDC (0.300g, 0.97 mmol) and H<sub>2</sub>AuCl<sub>4</sub>·3H<sub>2</sub>O (0.060g, 0.152 mM) were dissolved in 2-propanol (150 mL). The reaction mixture was stirred at 83 °C for 2 h, then Cu(NO<sub>3</sub>)<sub>2</sub>·2.5H<sub>2</sub>O (0.403g, 1.74 mmol) was added to the reaction mixture. The reaction was carried out under the same conditions for another 18 h. The solid obtained was separated from its mother liquor through centrifugation (5400 rpm) for 10 min, washed with 2-propanol and centrifuged again. The material obtained was thermally activated as described in Section 2.4.1.

### **2.7 Electrochemical cell setup**

The electrochemical cell is composed by three electrodes: a glassy carbon (GC) working electrode (modified or not-modified), a platinum wire counter electrode, and a saturated calomel electrode (SCE) as the reference electrode. The electrolyte solutions were purged with N<sub>2</sub> for 10 min to eliminate the dissolved O<sub>2</sub>.

SEM images of the modified electrodes were acquired using screen-printed electrodes (SPE) C110, purchased from Metrohm, composed by an Ag/AgCl reference electrode, a platinum counter electrode and a glassy carbon working electrode.

The electrolyte solutions employed in the electrochemical experiments were tris(hydroxymethyl)aminomethane (TRIS) buffer 0.1 M (pH 7.2), phosphate buffer (PBS) 0.1 M (pH 7.2) and NaCl 0.1 M. TRIS buffer 1.0 M (pH 7.2) was purchased from SIGMA ALDRICH and diluted with distilled water, while PBS buffer was made solubilizing  $\text{NaH}_2\text{PO}_4 \cdot \text{H}_2\text{O}$  (7,159 g) and  $\text{Na}_2\text{HPO}_4$  (6.839 g), both purchased from Merck Chemicals, in distilled water (1 L) adjusting the pH with a NaOH solution.

## **2.8 Electrodes modification**

### **2.8.1 GC/Cu-MOF**

$[\text{Cu}(1,3\text{-YBDC})] \cdot x\text{H}_2\text{O}$  (10 mg) was dispersed in 8 mL of EtOH and sonicated for 10 min; 10  $\mu\text{L}$  of the suspension were deposited over the GC surface. Then, the electrode was dried at 70  $^\circ\text{C}$  for 10 minutes.

### **2.8.2 GC/Cu-MOF/Au**

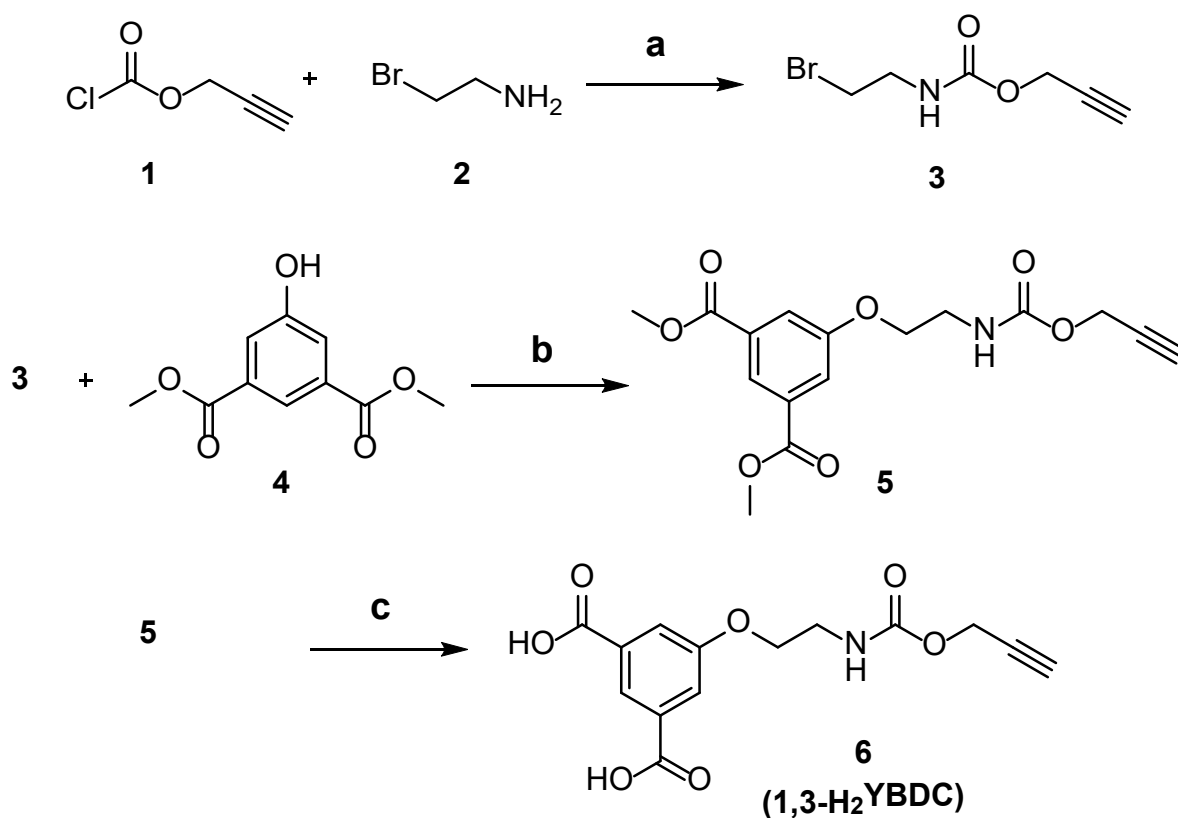
The GC/Cu-MOF electrode was placed inside an EtOH solution containing  $\text{HAuCl}_4$  5 mM for 10 min. The electrode was washed with ethanol to eliminate the excess of  $\text{HAuCl}_4$  from the GC or GC/Cu-MOF surface. Successively, the electrode was placed inside a PBS 0.1 M (pH 7.2) electrolytic solution. After drying the electrode at 70  $^\circ\text{C}$  for 10 min, the electro-deposition was carried at 0.05 V for 600 s to selectively reduce Au(III) to Au(0).

## CHAPTER 3

### 3 Linker and [Cu(1,3-YBDC)]·xH<sub>2</sub>O synthesis and characterization

#### 3.1 Linker Synthesis and characterization

The novel organic dicarboxylic linker 1,3-H<sub>2</sub>YBDC, bearing a propargylcarbamate group, was prepared following the synthetic route depicted in Scheme 3.1. The synthesis involves initial condensation of the commercially available chloroformate **1** with bromoamine **2**, yielding carbamate **3**. Crude **3** was then reacted with phenol **4** in the presence of NaI and cesium carbonate to afford arylether **5**, which was subsequently converted into the corresponding dicarboxylic acid **6** by LiOH-promoted hydrolysis, with overall, reproducible yields normally well above 95%.



**Scheme 3.1.** Synthesis of **6** (1,3-H<sub>2</sub>YBDC). Reagents and conditions: (a) NaHCO<sub>3</sub> (3 eq), THF/H<sub>2</sub>O, r.t., overnight; (b) NaI (1.5 eq.), Cs<sub>2</sub>CO<sub>3</sub> (1.5 eq.), 2-butanone, 80 °C, overnight; (c) LiOH (2.0 M), THF/MeOH, r.t., 3h.

Figure 3.1 shows the ESI-MS(+) spectra of 1,3-H<sub>2</sub>YBDC; the peak at 330 *m/z* is attributed to the pseudomolecular ion [C<sub>14</sub>H<sub>13</sub>NO<sub>7</sub> + Na]<sup>+</sup>.

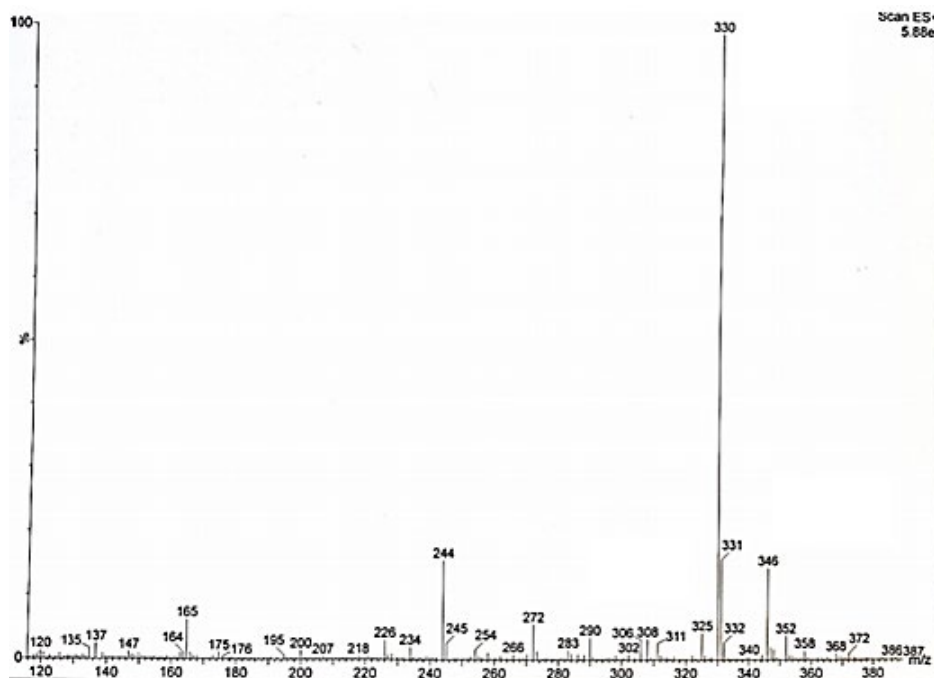


**Figure 3.1:** ESI-MS(+) spectrum of 1,3-H<sub>2</sub>YBDC.

Figure 3.2 shows the <sup>1</sup>H-NMR spectra of 1,3-H<sub>2</sub>YBDC. In the aromatic region, the Ar-H<sup>1</sup> signal at 8.29 ppm is a triplet and shows a <sup>4</sup>J<sub>H-H</sub> (1.5 Hz) coupling with the two symmetric Ar-H<sup>2</sup>, its integral was set to be unitary. The Ar-H<sup>2</sup> signal at 7.79 ppm is a doublet with a <sup>4</sup>J<sub>H-H</sub> with Ar-H<sup>1</sup> and an integral slightly more than double that of Ar-H<sup>1</sup>. In the aliphatic region of the spectra, the -OCH<sub>2</sub><sup>5</sup>C≡CH signal at 4.67 ppm is a doublet that integrates two protons, showing a <sup>4</sup>J<sub>H-H</sub> (2.4 Hz) coupling with the allylic proton -C≡CH<sup>6</sup>. The signals of -OCH<sub>2</sub><sup>3</sup>- and -CH<sub>2</sub><sup>4</sup>N(H)- are located at 4.25 ppm and 3.60 ppm respectively, being -OCH<sub>2</sub><sup>3</sup>- more deshielded due to its proximity to the more electronegative oxygen. They are both triplets, integrating two protons and displaying a <sup>3</sup>J<sub>H-H</sub> (6.8 Hz) coupling between each other. The signal at 2.95 ppm is attributed to -C≡CH<sup>6</sup>, it is a triplet because of its <sup>4</sup>J<sub>H-H</sub> with the two -OCH<sub>2</sub><sup>5</sup>C≡CH protons. Figure 3.3 shows the <sup>13</sup>C-NMR spectra of 1,3-H<sub>2</sub>YBDC.

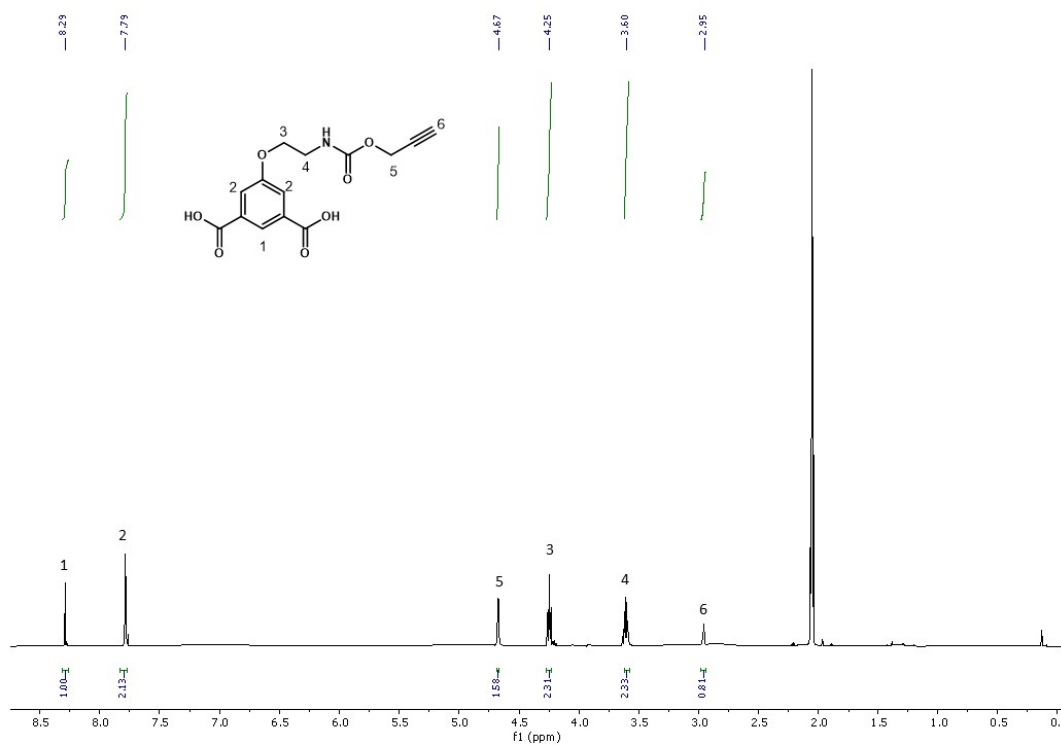


Figure 3.2: <sup>1</sup>H-NMR spectrum of 1,3-H<sub>2</sub>YBDC.

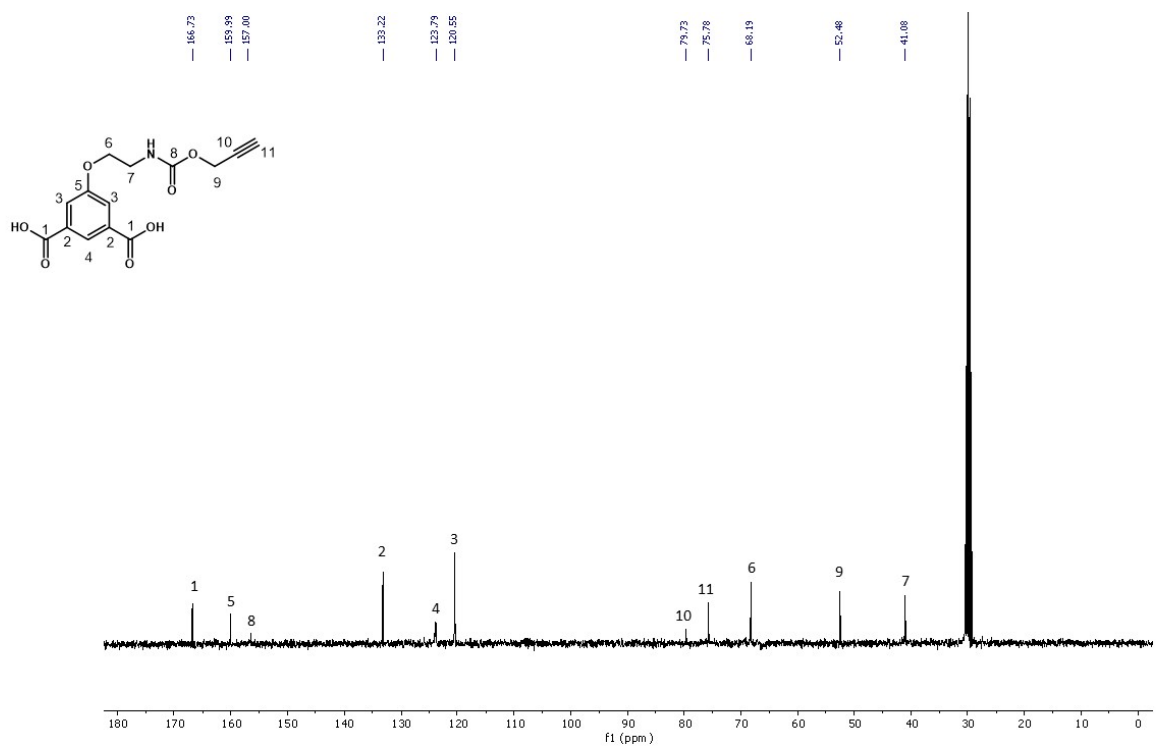
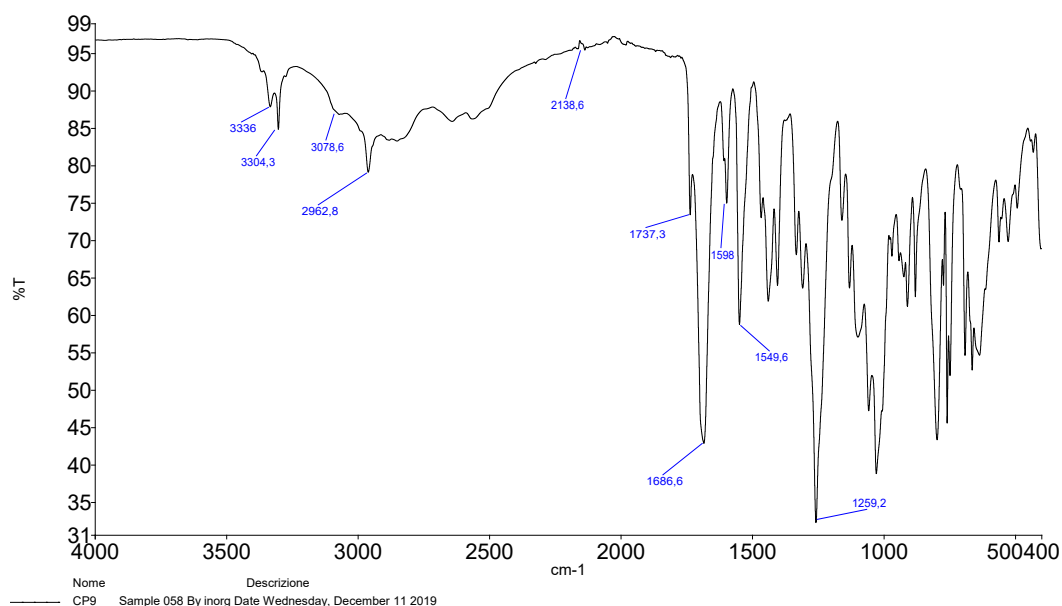


Figure 3.3: <sup>13</sup>C-NMR spectrum of 1,3-H<sub>2</sub>YBDC.

The IR-ATR spectra of 1,3-H<sub>2</sub>YBDC is showed in Figure 3.4. The peak at 3336 cm<sup>-1</sup> is attributed to the N-H bond stretching and the peak at 3304 cm<sup>-1</sup> is due to the ≡C-H stretching, both present in the propargylcarbamate residue of 1,3-YBDC. The broad band in the 2800-3200 cm<sup>-1</sup> region is attributed to the carboxylic acid H-O stretching while the stretching of both aliphatic and aromatic C-H bonds are responsible for the broad band at 3086-2961 cm<sup>-1</sup>. The peak at 1737 cm<sup>-1</sup> and 1687 cm<sup>-1</sup> are attributed to the stretching of carboxilate (-C(O)O-) and carbamate (-C(O)NH-) groups respectively. The bending of the carbammic N-H bond and the stretching of the C-O bond are attributed to the peaks at 1550 cm<sup>-1</sup> and 1259 cm<sup>-1</sup>, respectively. Due to the low change in dipole moment caused by the stretching of the alkylic C≡C bond, its peak is barely visible at 2139 cm<sup>-1</sup>.



**Figure 3.4:** IR-ATR spectrum of 1,3-H<sub>2</sub>YBDC.

The TGA analysis of the as prepared 1,3-H<sub>2</sub>YBDC (Figure 3.5) showed a high residue (5%) at 800 °C, indicating the presence of inorganic impurities in the sample deriving from the inorganic salts used in large excesses during the last step of the synthesis.

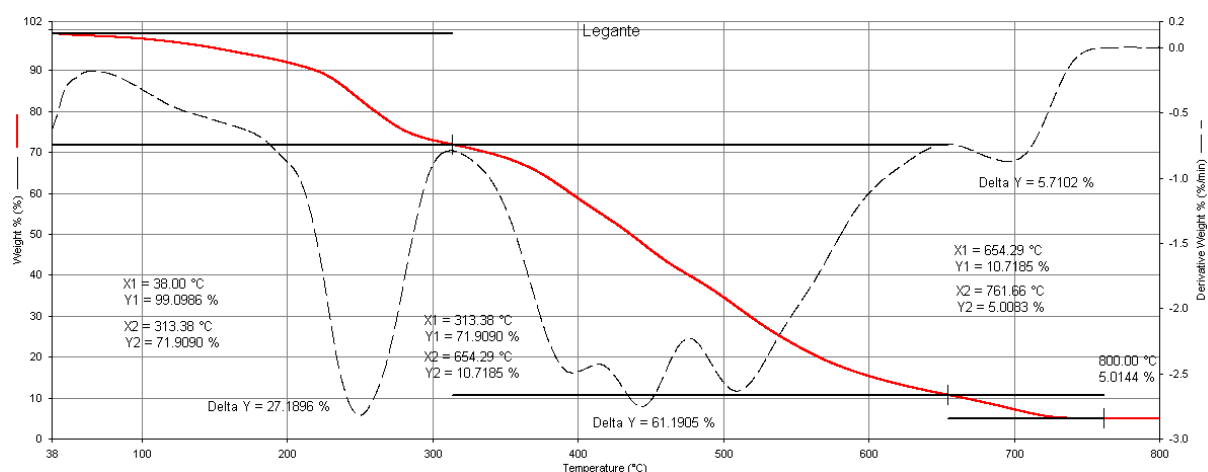


**Figure 3.5** TGA curve (continuous red line) and first derivative (dashed line) of the weight loss of 1,3-H<sub>2</sub>YBDC.

**Table 3.1:** TGA table of 1,3-H<sub>2</sub>YBDC.

1° loss (%)	2° loss (%)	3° loss (%)	Residue (800°C, %)
21.2	61.2	5.7	5.0

The presence of LiCl and/or LiOH in the linker could lead to the formation of copper hydroxides and/or copper chlorides impurities within the MOF able to occupy the MOF's pores and in turn lowering its surface area and pore volume. To prevent this from happening, the purification of the linker through crystallization became mandatory. The procedure is described in Section 2.3.4. As shown in Table 3.2, after the first crystallization, the melting point of the linker increased from 186-191 °C to 216-217 °C.

**Table 3.2:** Yields and melting points of the crystallized products.

	Yield (%)	Melting point (°C)
First crystallization	29.6	216-217
Second crystallization	8.7	216-217
Third crystallization	11.8	215-217
Fourth crystallization	4.2	187-190

The increased purity was confirmed by the lower % of residue observed in the TGA analysis of the product after the first crystallization.

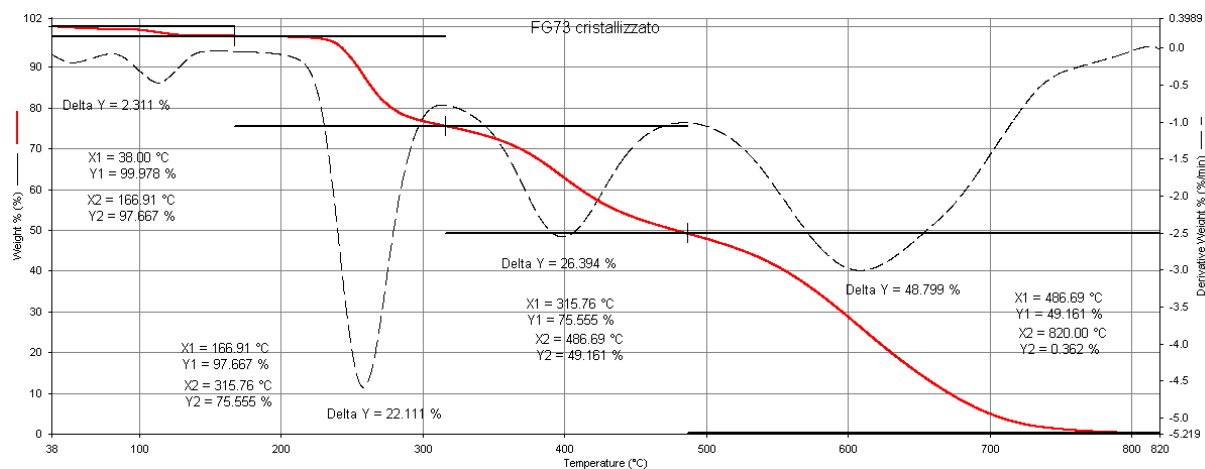


**Figure 3.6:** TGA curve (continuous red line) and first derivative (dashed line) of the weight loss of 1,3-H<sub>2</sub>YBDC from the first crystallization.

**Table 3.3:** TGA losses of 1,3-H<sub>2</sub>YBDC from the first crystallization.

1° loss (%)	2° loss (%)	3° loss (%)	4° loss (%)	Residue (800°C, %)
2.3	22.1	26.4	48.8	0.4

Because of the presence of impurities, 1,3-H<sub>2</sub>YBDC from the fourth crystallization onward showed a lower melting point and a pink colour. For this reason, it was discarded. The similarity between the <sup>1</sup>H-NMR of the as synthesized 1,3-H<sub>2</sub>YBDC (Figure 3.2) and that of the recrystallized one (Figure 3.7), suggests that the recrystallization process does not chemically modify the structure of the molecule. The crystallized 1,3-H<sub>2</sub>YBDC was used as the linker for the synthesis of the MOF.

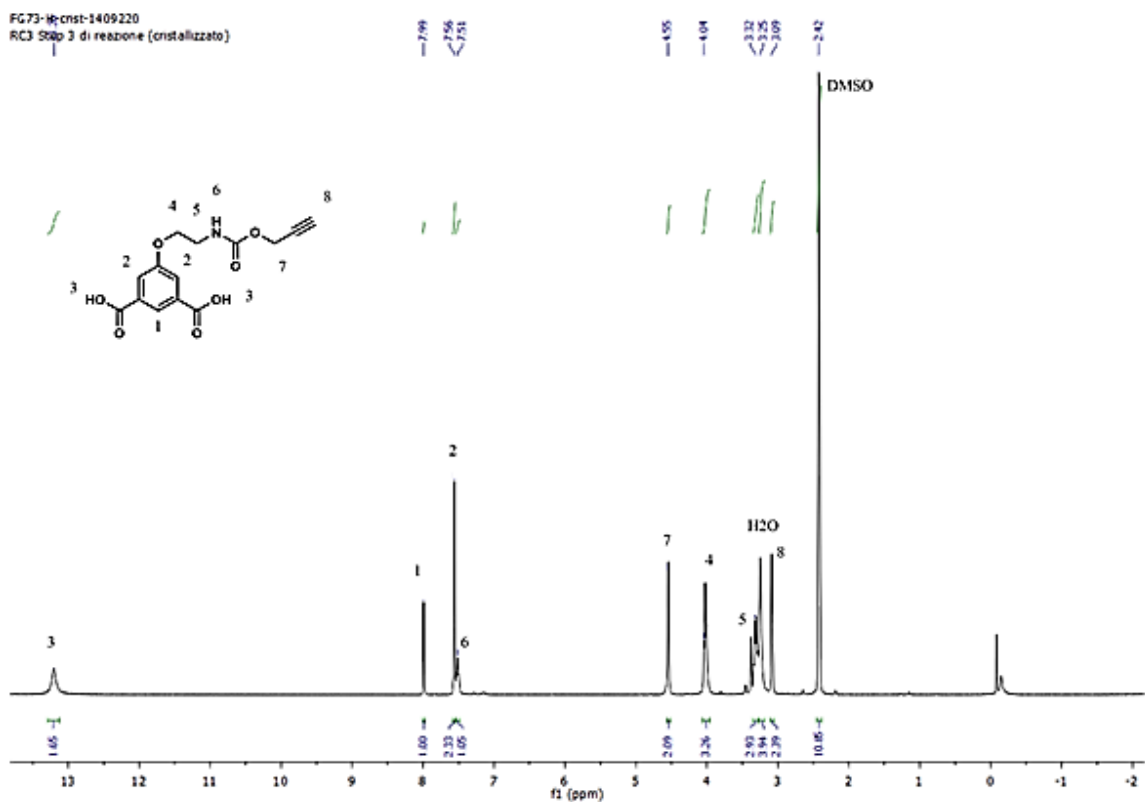
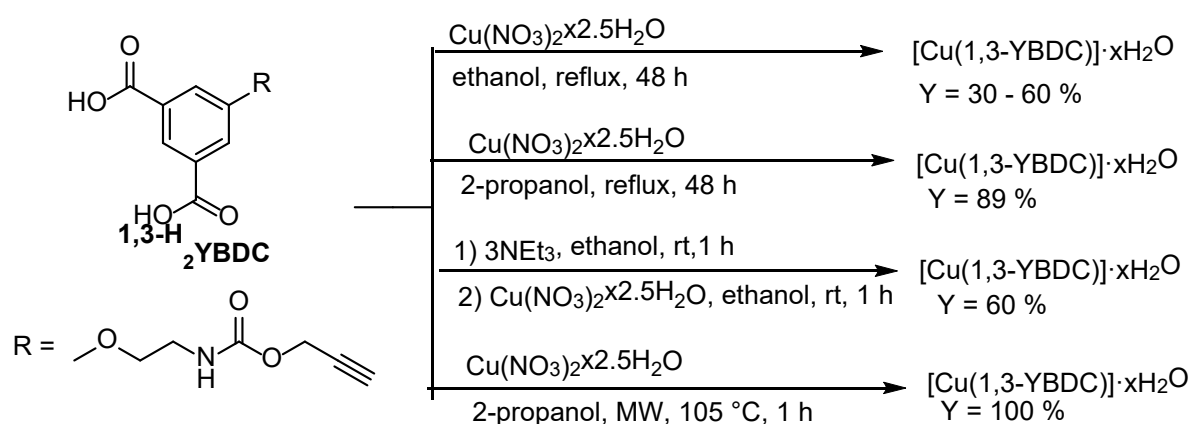


Figure 3.7:  $^1\text{H-NMR}$  of 1,3- $\text{H}_2\text{YBDC}$  from the first crystallization.

### 3.3 [Cu(1,3-YBDC)]·xH<sub>2</sub>O synthesis and characterization

#### 3.2.1 Optimal reaction conditions screening

As shown in Scheme 3.2, the dicarboxylic linker 1,3-H<sub>2</sub>YBDC was reacted with Cu(NO<sub>3</sub>)<sub>2</sub>·2.5H<sub>2</sub>O under different reaction conditions. It was found that in refluxing ethanol for 48 h, regardless of the Cu:L molar ratios employed (from 1:1 to 5:1), the yields were erratically ranging between 30 and 60% (based on 1,3-H<sub>2</sub>YBDC). As reported by Morris et al.<sup>31</sup> this behaviour is due to the concomitant copper-promoted esterification reaction of the diacid with ethanol and indeed the presence of the diester was confirmed by analysing the reaction supernatant and washings by NMR spectroscopy.



**Scheme 3.2:** Synthesis of [Cu(1,3-YBDC)]·xH<sub>2</sub>O under different conditions.



**Figure 3.8:** [Cu(1,3-YBDC)]·xH<sub>2</sub>O inside its mother liquor on the left and MOF after work-up on the right.

When 2-propanol is used instead of ethanol, such side reaction is minimized, and the yields were repeatable and always about 90 % or more. Alternatively, the diacid 1,3-H<sub>2</sub>YBDC was first reacted with triethylamine in ethanol to give the corresponding triethylammonium salt [NEt<sub>3</sub>H]<sub>2</sub>[1,3-YBDC] that was isolated as a pale, yellow oil that immediately reacts with copper nitrate at room temperature. Regardless of the conditions employed, the final product was always a turquoise polycrystalline powder having formula [Cu(1,3-YBDC)]·xH<sub>2</sub>O

Attempts to get X-ray quality single crystals either by carrying out the reaction under hydrothermal conditions using a mixture of water/benzene or layering a solution of  $\text{Cu}(\text{NO}_3)_2$  in ethanol onto a solution of  $[\text{NEt}_3\text{H}]_2[1,3\text{-YBDC}]$  in  $\text{CHCl}_3$ , failed. Through a microwave-assisted synthesis of  $[\text{Cu}(1,3\text{-YBDC})]\cdot x\text{H}_2\text{O}$  in 2-propanol, a turquoise solid was obtained with a very high yield in just one hour.

The screening of the reaction conditions was performed through XRD characterization of the products (Figures 3.9 and 3.10).

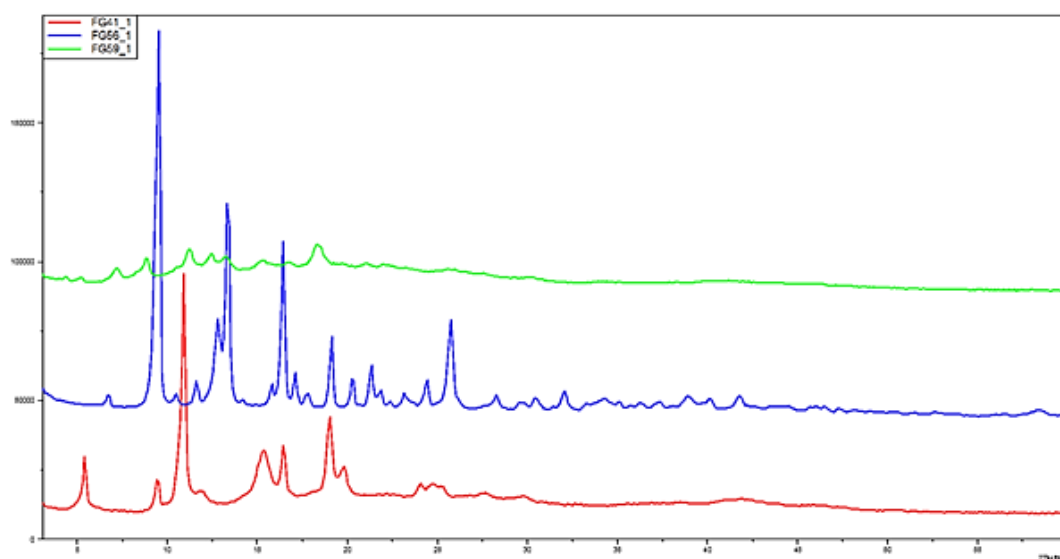


**Figure 3.9:** XRD patterns of MOF powders from different synthesis: synthesis in ethanol 48 h (red line), synthesis in 2-propanol 48 h (blue line), synthesis in ethanol with trimethylamine (green line).

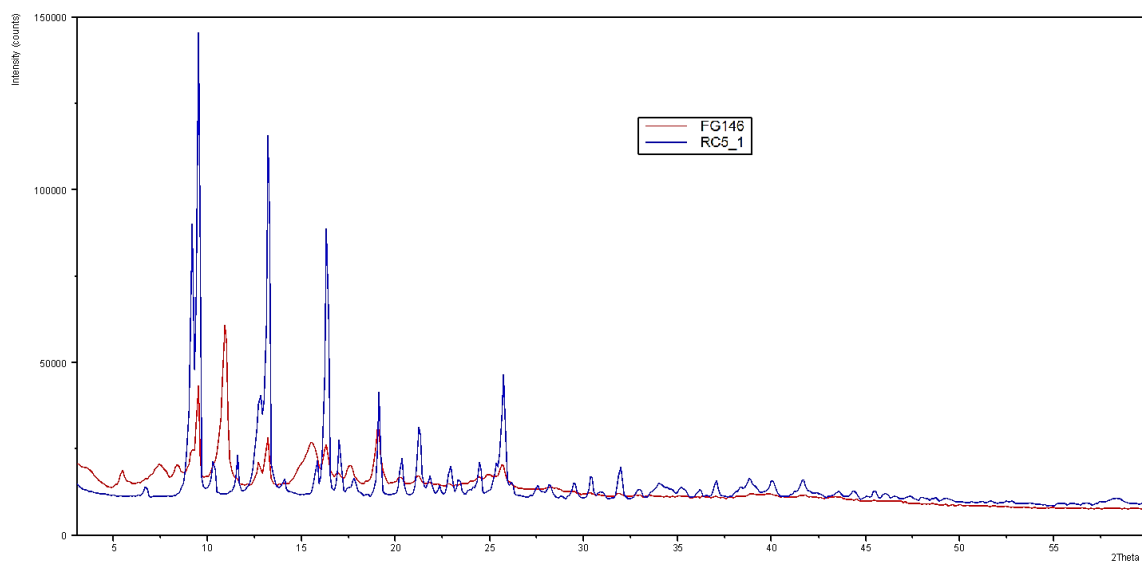


**Figure 3.10:** XRD patterns of MOF powders from different synthesis: synthesis in 2-propanol 24 h (blue line), microwave assisted synthesis (red line).

The only product that satisfied the crystallinity requirement is the one from the solvothermal synthesis in 2-propanol (Figures 3.9 and 3.10 blue line). The use of ethanol as the solvent for the synthesis (Figure 3.9 red line) led to a low degree of crystallinity. The use of triethylamine as a templating agent (Figure 3.9 green line) in ethanol caused an even lower degree of crystallinity, as shown by the broadness of the peaks in the XRD spectra. The XRD spectra of the product of the microwave-assisted synthesis also shows broad peaks. Although its XRD spectra (Figure 3.10 red line) and that of the solvothermal synthesis in 2-propanol product have some peaks in common, the XRD of the microwave-assisted synthesis product shows other peaks indicating the presence of another phase, which is preponderant. By looking at the broadness of the peak at about  $15^\circ 2\theta$ , the crystallinity of this new phase also seems to be very low. For all these reasons, 2-propanol was chosen as the solvent for the solvothermal synthesis of  $[\text{Cu}(1,3\text{-YBDC})]\cdot x\text{H}_2\text{O}$ .

The screening for the solvent was followed by the screening for the optimal reaction time. The solvothermal synthesis in 2-propanol was carried for 24, 48, 72, and 120 hours. The XRD spectra of the products of these reactions are shown in Figure 3.11.

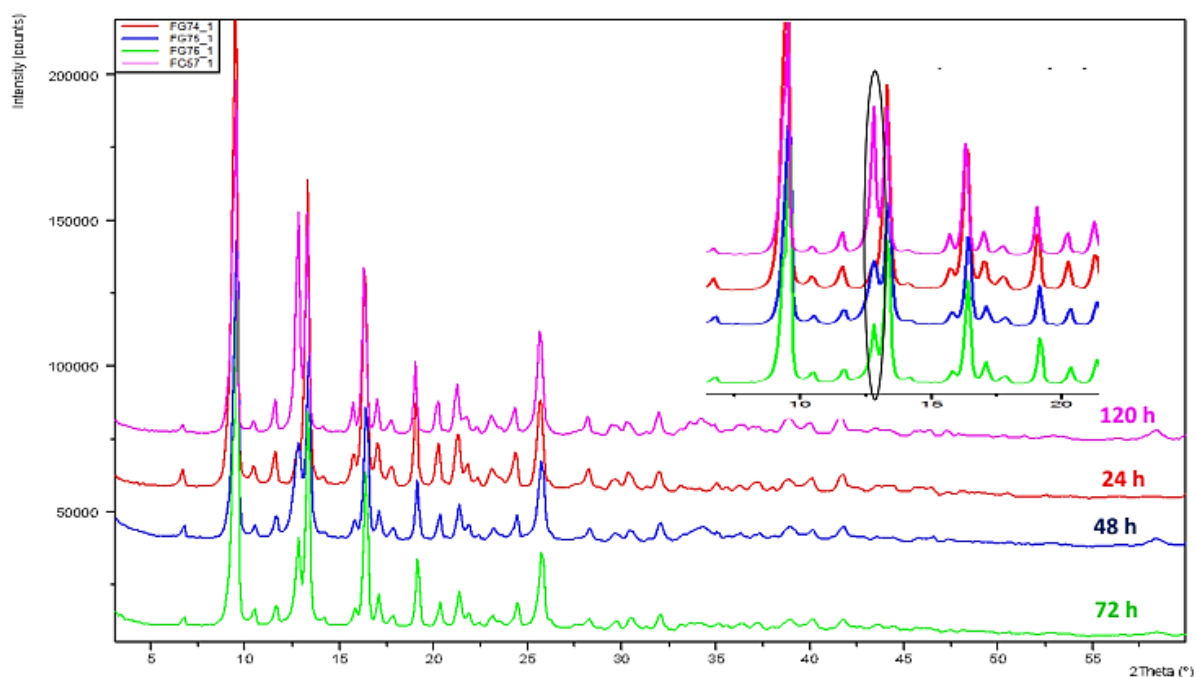


**Figure 3.11:** XRD patterns of MOF powders from solvothermal synthesis carried in 2-propanol at different reaction times: 24 h (red), 48 h (blue), 72 h (green), 120 h (purple).

Increasing the reaction time over 24 hours led to the formation of a new crystalline phase, as evidenced by the peak at about  $12.5^\circ 2\theta$  present in the XRD of the products from the reactions carried for 48h, 72 h, and 120 h. For this reason, 24 hours was chosen as the optimal reaction time for the synthesis of the MOF and all the characterization was carried out on this sample.

### 3.2.2 Vibrational spectroscopy and thermal characterization

Figure 3.12 shows the IR spectra of the linker (black) and the MOF (red). The very broad band in the  $2800\text{-}3200\text{ cm}^{-1}$  region, attributed to the carboxylic acid H-O bond stretching and observable in the linker's IR spectra (black), is not present in the MOF's IR spectra (red). This means that the deprotonation of the linker must occur in order for the MOF to form.

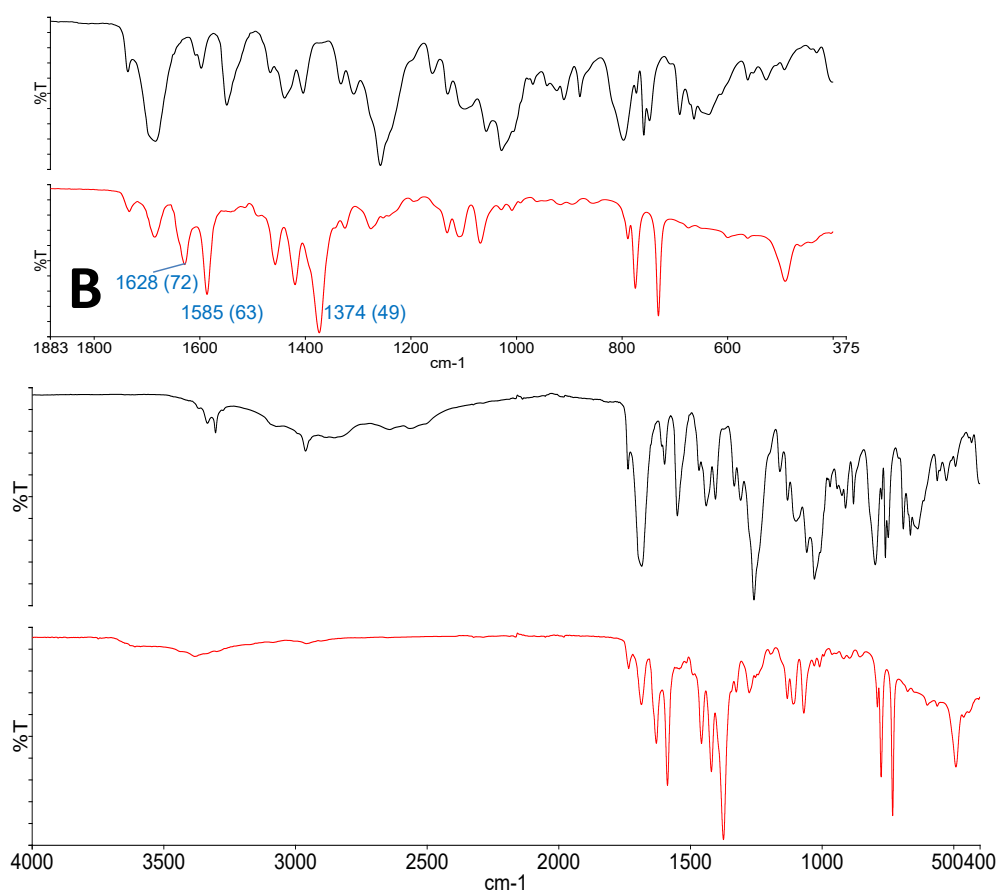


**Figure 3.12:** (A) ATR-FTIR spectra of 1,3-H<sub>2</sub>YBDC (black curve) and [Cu(1,3-YBDC)]·xH<sub>2</sub>O (red curve); (B) magnification of the 1800-400 cm<sup>-1</sup> range (in parentheses the % Transmittance values of the labelled peaks).

The peak at  $731\text{ cm}^{-1}$  is attributed to the Cu-O bond.<sup>32</sup> This suggests the coordination of copper with the carboxylate groups of the linker. Because the IR-ATR was always the first analysis performed on the MOF right after its activation, the presence of the  $731\text{ cm}^{-1}$  peak in the spectra was used to verify if the MOF synthesis was successful and if the material was worthy of further characterizations. The broad peak at  $3000\text{-}3500\text{ cm}^{-1}$  in the

[Cu(1,3-YBDC)]·xH<sub>2</sub>O IR spectra indicates the presence of water inside the MOF structure.<sup>32</sup> This peak is not present in the linker's IR spectra. The presence of water in the MOF could be explained by one or both:

- the adsorption of water from air between the MOF thermal activation and the IR analysis (supported by later shown TGA characterization);
- the presence of weakly bonded water molecules from Cu(NO<sub>3</sub>)<sub>2</sub>·2.5H<sub>2</sub>O that are not removed during thermal activation.

The signals at 1605 and 1004 cm<sup>-1</sup> are associated with the vibrations of the C=C bonds of the benzene ring. In addition, the IR spectrum shows two intense bands at 1585 and 1374 cm<sup>-1</sup> particularly diagnostic for the asymmetric and symmetric stretching mode of the carboxylate group (RCO<sub>2</sub><sup>-</sup>).<sup>33</sup> The peaks at 3336 cm<sup>-1</sup> and 3304 cm<sup>-1</sup> are associated with the vibrations of the ≡C-H and N-H bonds, respectively. These peaks are both presents in the 1,3-YBDX and the [Cu(1,3-YBDC)]·xH<sub>2</sub>O IR spectra, although in the second one they are less recognizable due to the presence of water. The peak at 1628 cm<sup>-1</sup> is attributed to the ν(C=O) stretching of the carbamate group. Because of the coordination of this group to the apical position of copper (see paragraph 3.2.3 Crystallochemical Analysis), the peak is located at a frequency 59 cm<sup>-1</sup> lower than in the pristine 1,3-H<sub>2</sub>YBDC.<sup>34</sup>

Figure 3.13 shows a comparison between the Raman spectra of the linker, the MOF, and copper nitrate. Because of the little change of dipole moment induced by the symmetric stretching of the terminal alkyne group, its peak is not observable in the IR spectra. For this reason, the Raman spectra was used to monitor the alkyne functionality. The peak attributed to the stretching of this group is observable at 2135 cm<sup>-1</sup>. The presence of this peak in both the linker's and MOF's spectra suggests that, other than deprotonation, no further modification of the linker occurs during the synthesis.

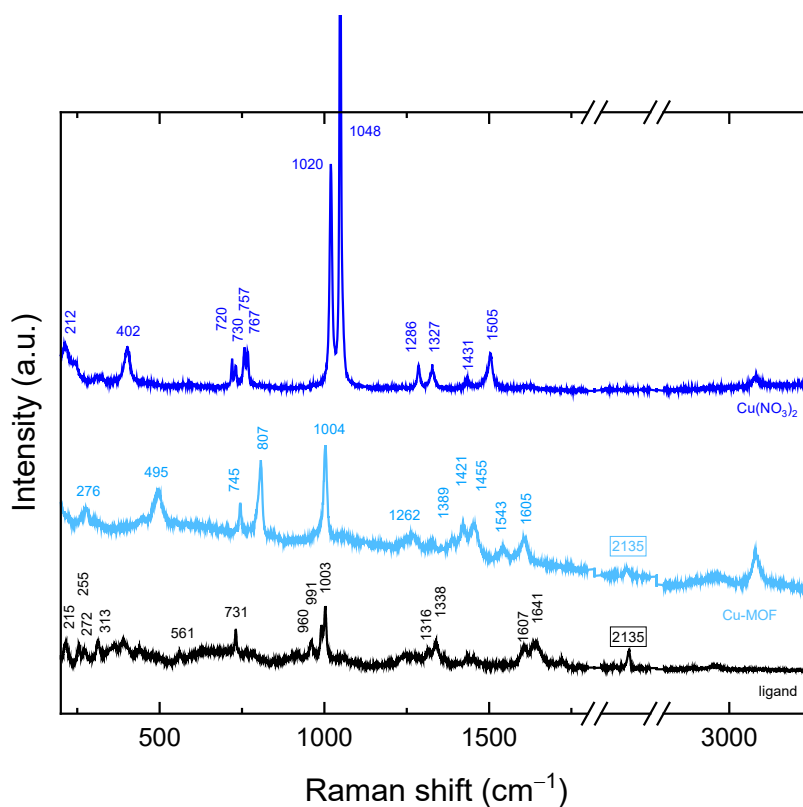


**Figure 3.13:** Raman spectra of 1,3-H<sub>2</sub>YBDC (black), Cu(NO<sub>3</sub>)<sub>2</sub>x2.5H<sub>2</sub>O (blue) and [Cu(1,3-YBDC)]·xH<sub>2</sub>O.

As mentioned in the introduction, the purpose of the propargylcarbamate group is to give the MOF the ability to synthesize AuNPs. In the proposed mechanism for AuNPs formation shown in scheme 1.1, the alkyne functionality is lost at the end of the process. For this reason, the Raman characterization was also useful to monitor AuNPs formation. In the low frequency range of the Raman spectra, the peaks at 495 and 276 cm<sup>-1</sup> are assigned to the vibrational stretching modes of equatorial and axial Cu-O bonds respectively.<sup>35</sup> The signals located at 1605 and 1004 cm<sup>-1</sup> are associated with the benzene ring  $\nu(\text{C}=\text{C})$  stretching modes. The peaks at 807 and 745 cm<sup>-1</sup> are caused by the out-of-plane  $\delta(\text{C}-\text{H})$  and  $\delta(\text{C}=\text{C})$  ring bending vibrations, respectively.

The elemental analysis of the synthesized sample is in good agreement with the theoretical chemical composition, showing a Cu/N molar ratio of ca. 1 (see the Experimental Part). The TGA characterization was used to investigate the thermal stability of the MOF (Figure 3.14).

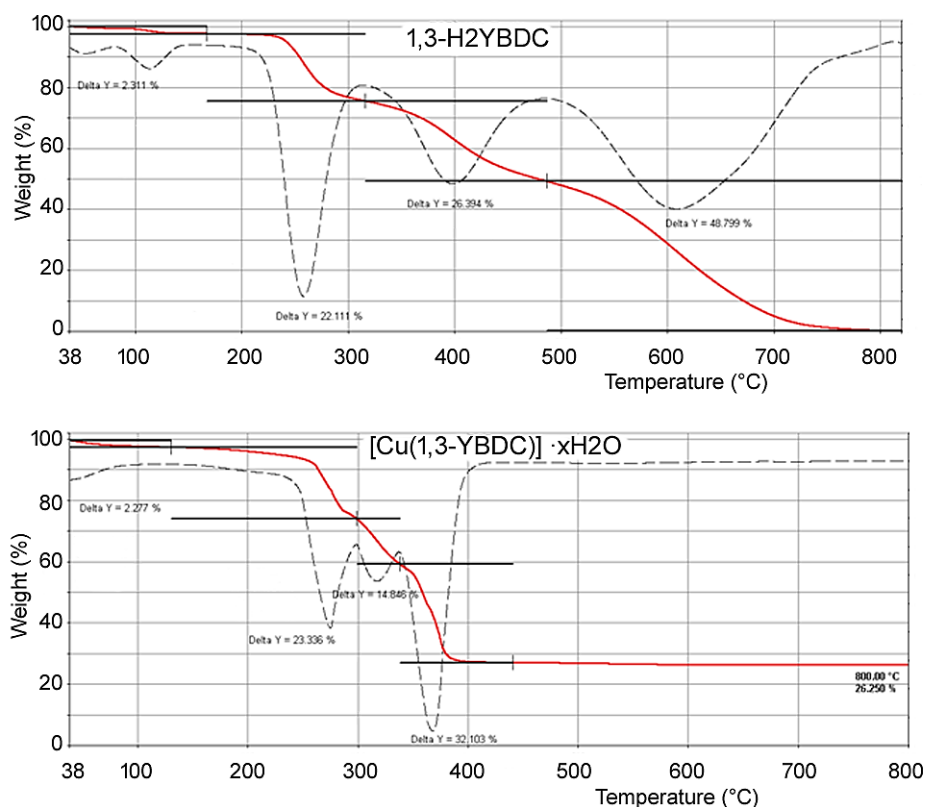


**Figure 3.14:** TGA curves (continuous red lines) and their first derivatives (dashed lines) for 1,3-H<sub>2</sub>YBDC (top) and [Cu(1,3-YBDC)]·xH<sub>2</sub>O (bottom).

**Table 3.4:** TGA losses.

	1° loss (%)	2° loss (%)	3° loss (%)	4° loss (%)	Residue (800 °C, %)
1,3-H <sub>2</sub> YBDC	2.3	22.1	26.4	48.8	0.4
[Cu(1,3-YBDC)]·xH <sub>2</sub> O	2.3	23.9	14.85	32.1	26.5

The first loss (2.3%), from 38 to 100 °C in both samples, could be caused by the evaporation of water absorbed from air by the samples before the TGA analysis.

The TGA plot for 1,3-H<sub>2</sub>YBDC (of C<sub>14</sub>H<sub>13</sub>NO<sub>7</sub> formula, mw 307.25 g mol<sup>-1</sup>) shows three main weight losses between 200 and 600 °C, due to organic material decomposition, and zero residual weight. The first two steps are interpreted by progressive loss of the propargyl fragments (obs. 48.5%, calc. for C<sub>6</sub>H<sub>8</sub>NO<sub>3</sub> 46.3%). Similarly, the copper-containing product (of C<sub>14</sub>H<sub>11</sub>CuNO<sub>7</sub> formula, mw 368.79 g mol<sup>-1</sup>) shows three decomposition steps in the 200-350 °C range (attributed, as above, to the loss of the C<sub>6</sub>H<sub>8</sub>NO<sub>3</sub> residue, obs. 38.2%, calc. 38.5%), terminating at a temperature ca. 150 °C lower than in the pristine organic ligand.

Such lower thermal stability of the organic skeleton within the MOF is tentatively attributed to assistance, during decomposition, of redox processes catalysed by Cu(II) ions. Furthermore, a residue of 26 wt% is present at 400 °C, with no significant variation up to 800 °C, which is presumably due to residual CuO. Assuming that all the copper in the MOF retain its oxidation state during the degradation process, only copper (II) oxide, with a stoichiometry of Cu:O = 1:1, will be present in the residue. Because in this oxide copper represents 79.54 % of the weight, it represents 21.07 % of the total weight of the sample used for the TGA analysis. From the AAS characterization the amount of copper inside the MOF is reported to be 18.3 %, so the excess residual could be from thermally stable carbonaceous materials.

### 3.2.3 Crystallochemical analysis

A sample of [Cu(1,3-YBDC)]·xH<sub>2</sub>O was sent to the Department of High Technology of the University of Insubria (Como) in order to perform a synchrotron X-ray diffraction analysis. Because no single crystal of the MOF was obtained, the crystal structure was simulated based on XRD data from MOF powder (Figure 3.15).

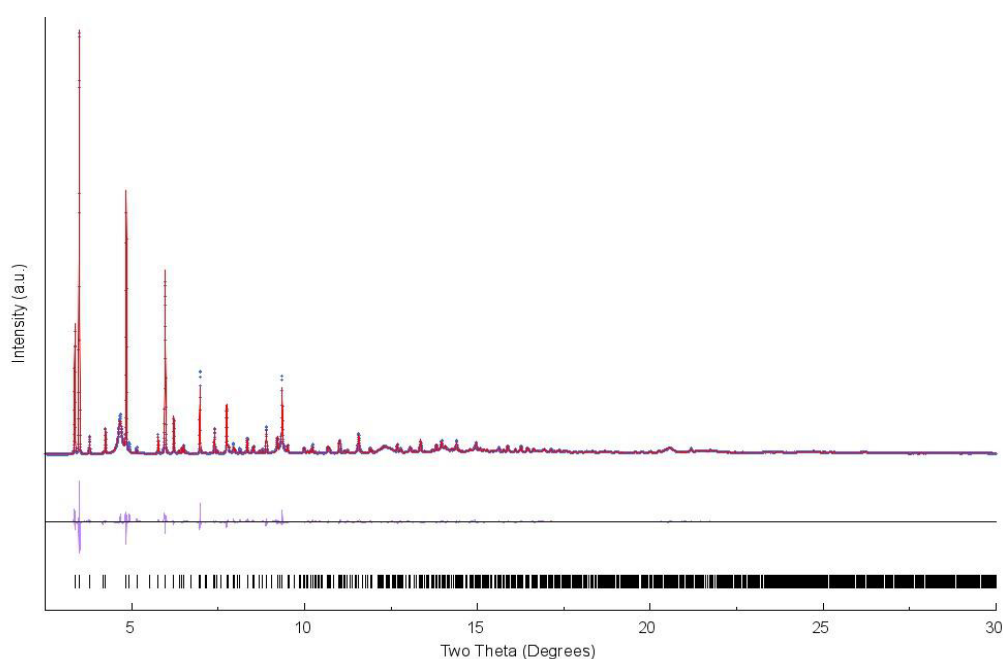


**Figure 3.15:** Rietveld refinement plot for [Cu(1,3-YBDC)]·xH<sub>2</sub>O; Blue trace = observed data; red trace = calculated pattern from the simulated structure. Difference plot in purple; peak markers at the bottom are for [Cu(1,3-YBDC)]·xH<sub>2</sub>O.

The structure obtained from the simulation suggests that the solid [Cu(1,3-YBDC)]·xH<sub>2</sub>O contains a network of isophthalate anions linked to Cu (II) centres belonging to the paddlewheel dimeric fragments. The apical atom in these fragments is the oxygen of the

carbonyl group belonging to the propargylcarbamate residue. This confirms the presence of a coordination between Cu (II) and the carbamate group of the linker. The distance between the two copper atoms in the paddlewheel fragments is calculated to be 2.633 Å. The average Cu-O equatorial bond distance is 2.00 Å. The conformation of the ligand is locked into two different conformations inside the MOF's crystalline phase. In both conformers, the alkyne moieties point directly into the crystal cavities.

Figures 3.16.E and 3.16.F show the complete structure of both conformers, not including the weakly bonded water molecules.

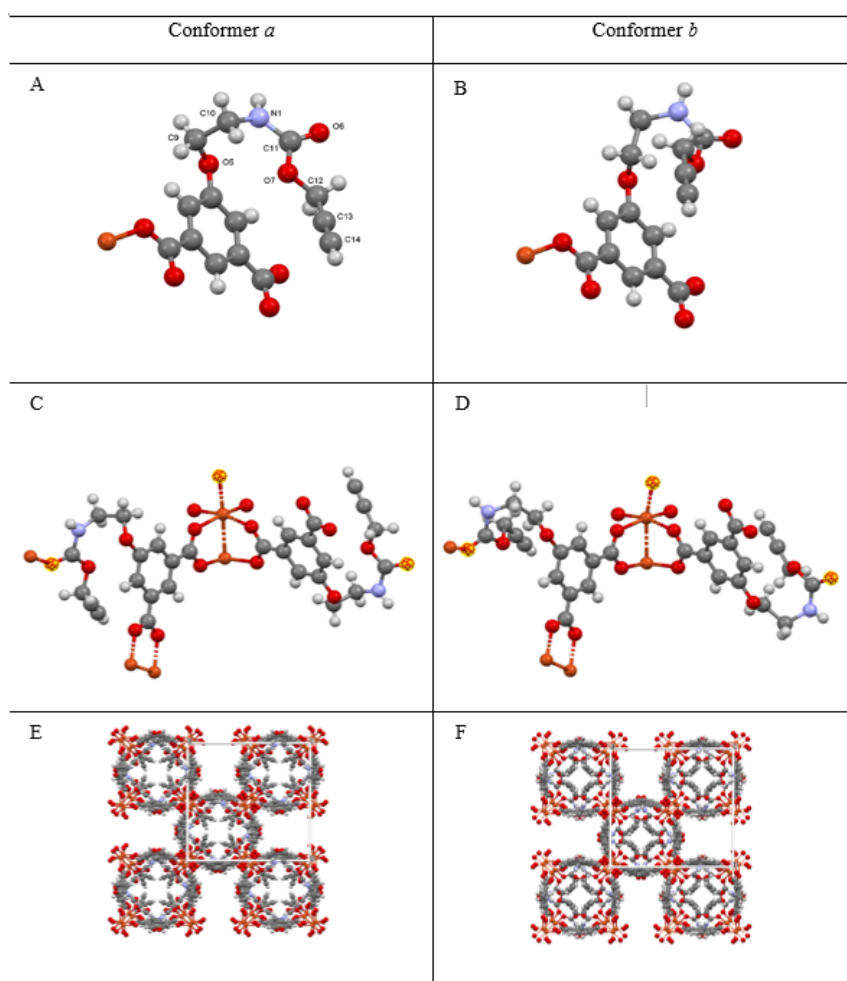


**Figure 3.16:** (A, B) the two different conformers *a* and *b*; (C, D) paddlewheel fragments arising from the two conformers; (E, F) crystal packing of the two conformers.

The void space inside the MOF structure is reported to be 20% of the volume and is partially occupied by water molecules, possibly disordered and of non-stoichiometric character.

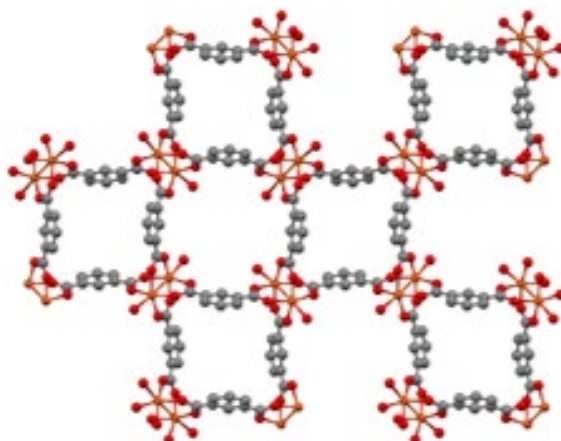


**Figure 3.17:** crystal packing with omitted hydrogens and propargylcarbamate residues.

The crystalline phase of the MOF is composed by corrugated 2D layers interlinked by the long propargylcarbamate residues through the apical coordination of the carbonyl oxygen with copper. The size of the MOF cavities was reported to be  $141 \text{ \AA}^3$ .

However, taking into account the approximate volume of the tetrachloroaurate anion [the Au(0) precursor,  $\approx 142 \text{ \AA}^3$ ] and the tabulated size of a single Au atom [ $\approx 43(2) \text{ \AA}^3$ ],<sup>36</sup> the MOF could be used for capturing and anchoring gold species, both inside the material (although to a small extent) and, primarily, on its external surface, due to its dense and even array of protruding propargylcarbamate residues. Taking into account the size of crystalline domain estimated by the XRD model (of the order of 100 nm for isotropic particles), nearly 2% of the ligands lie on the crystal surface, possibly acting as catalytic sites.

### 3.2.4 SEM-EDX characterization

The SEM image of the MOF (Figure 3.18) shows the occurrence of interconnected lamellar structures with an average lateral dimension of 2-3  $\mu\text{m}$  and a mean thickness of 200 nm.

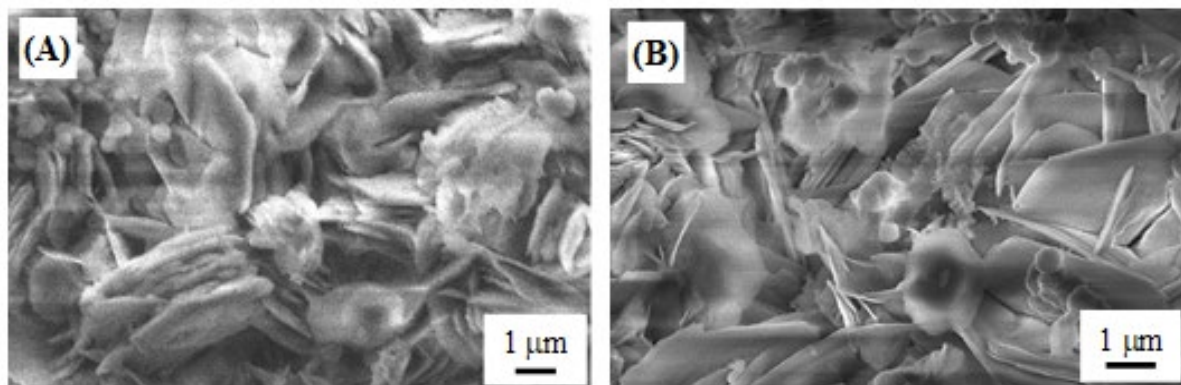


Figure 3.18: SEM images of  $[\text{Cu}(1,3\text{-YBDC})]\cdot x\text{H}_2\text{O}$ .

Figure 3.19 shows the presence of carbon, oxygen, copper and no other elements in the analysed region of the sample. Because of the low amount of azote in the sample, its signal is hidden behind the C and O peaks. Figure 3.20 shows the element distribution on the analysed surface.

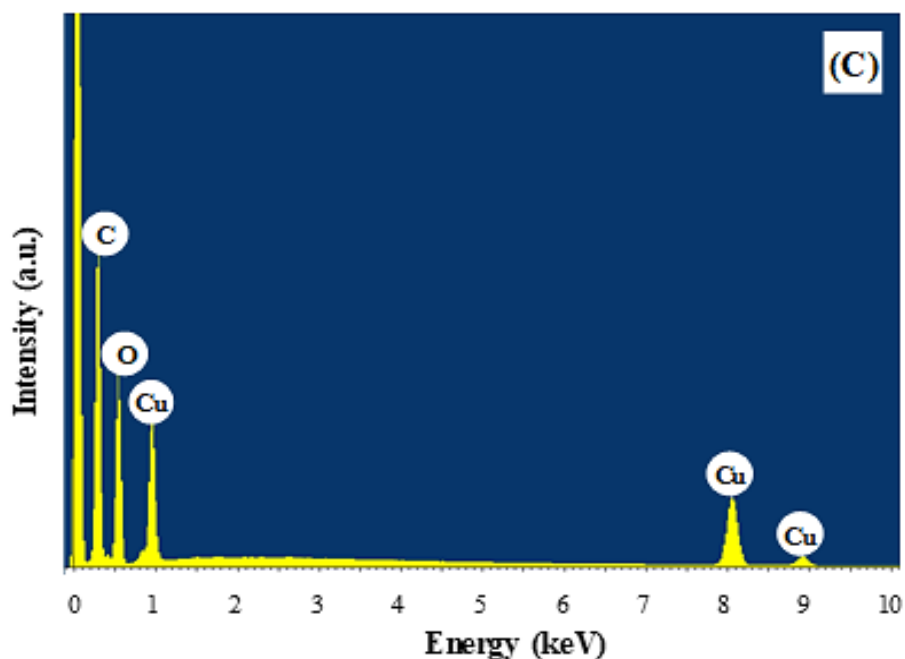
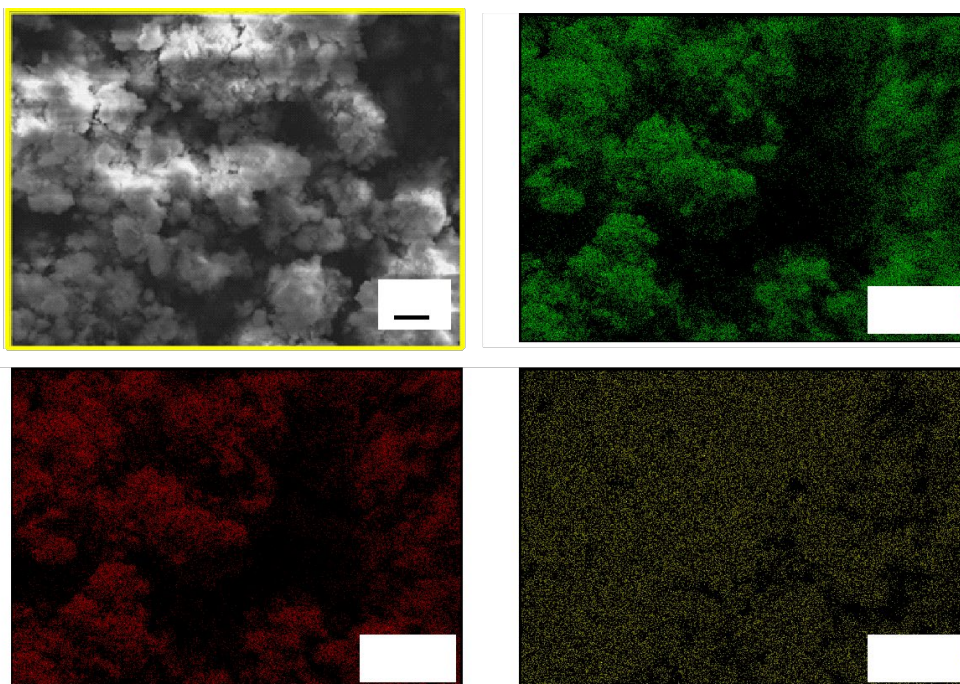


Figure 3.19: EDX spectra of  $[\text{Cu}(1,3\text{-YBDC})]\cdot x\text{H}_2\text{O}$ .



**Figure 3.20:** C, O and Cu EDXS elemental maps, recorded on the corresponding electron image contained in the yellow box, for  $[\text{Cu}(1,3\text{-YBDC})]\cdot x\text{H}_2\text{O}$  specimen.

### 3.2.5 XPS characterization

The XPS analysis, performed by the Department of Chemical Sciences of Padova University, was used to inspect the elements present on the MOF's surface, their oxidation states and their chemical environments (Figure 3.21).

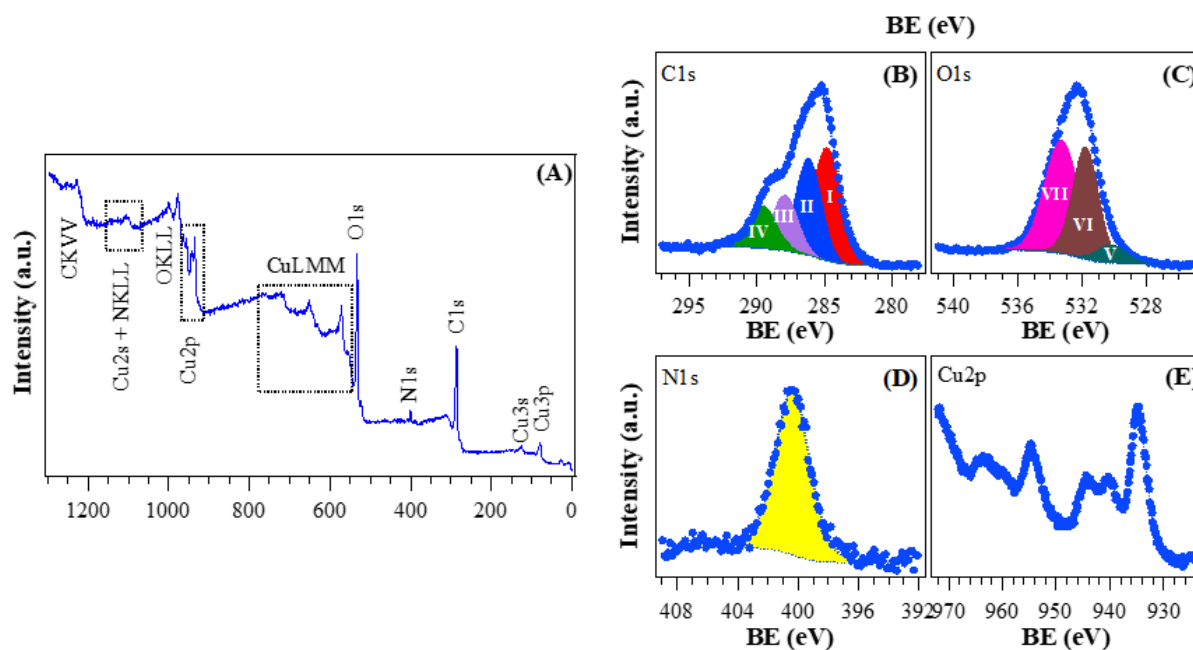


**Figure 3.21:** XPS analysis for the target  $[\text{Cu}(1,3\text{-YBDC})]\cdot x\text{H}_2\text{O}$  specimen: (A) wide-scan spectrum; (B) C1s, (C) O1s, (D) N1s, (E) Cu2p photoelectron peaks.

The quantitative analysis revealed the presence of C (58.7%), N (5.2%), O (31.3%), and Cu (4.8%) elements on the surface of the MOF (atomic percentages). The C 1s signal can be seen as the superposition of four peaks (Figure 3.21.B), each representing carbon in a different chemical environment (Table 3.5).<sup>37</sup>

**Table 3.5:** C 1s XPS peaks.

Peak	BE (eV)	Chemical environment	C signal contribution %
<b>C 1s (I)</b>	284.8	C-C	40
<b>C 1s (II)</b>	286.2	C-N/C-O	30
<b>C 1s (III)</b>	287.9	Ar-COOH	20
<b>C 1s (IV)</b>	289.6	-NCOO-	10

The O 1s signal can be seen as the superposition of three peaks (Figure 3.21.C), each representing oxygen in a different chemical environment (Table 3.6).<sup>38</sup>

**Table 3.6:** O 1s XPS peaks.

Peak	BE (eV)	Chemical environment	O 1s signal contribution %
<b>O 1s (V)</b>	530.2	Cu-O	8
<b>O 1s (VI)</b>	531.8	C-OH	40
<b>O 1s (VII)</b>	533.3	C=O/H <sub>2</sub> O	52

The N1s peaks (Figure 3.21.D) showed a single contribution centred at BE = 400.3 eV. The Cu peaks pattern (Figure 3.21.E), with Cu 2p<sub>3/2</sub> and Cu 2p<sub>1/2</sub> at 934.8 eV and 954.7 eV respectively, is a fingerprint of d<sup>9</sup> Cu (II) coming from the metal centers of the MOF and Cu(II) hydroxides.<sup>39</sup>

### 3.2.6 Surface area and porosity

A sample of [Cu(1,3-YBDC)]·xH<sub>2</sub>O was sent to the institute of Organic Synthesis and Photoreactivity (CNR-ISOF, Bologna) in order to study the surface area and pore volume by measuring the adsorption isotherm of nitrogen at 77 K (Figure 3.22). The sample was pre-treated at 343 K under vacuum (1x10<sup>-3</sup> mbar) for 2 h.

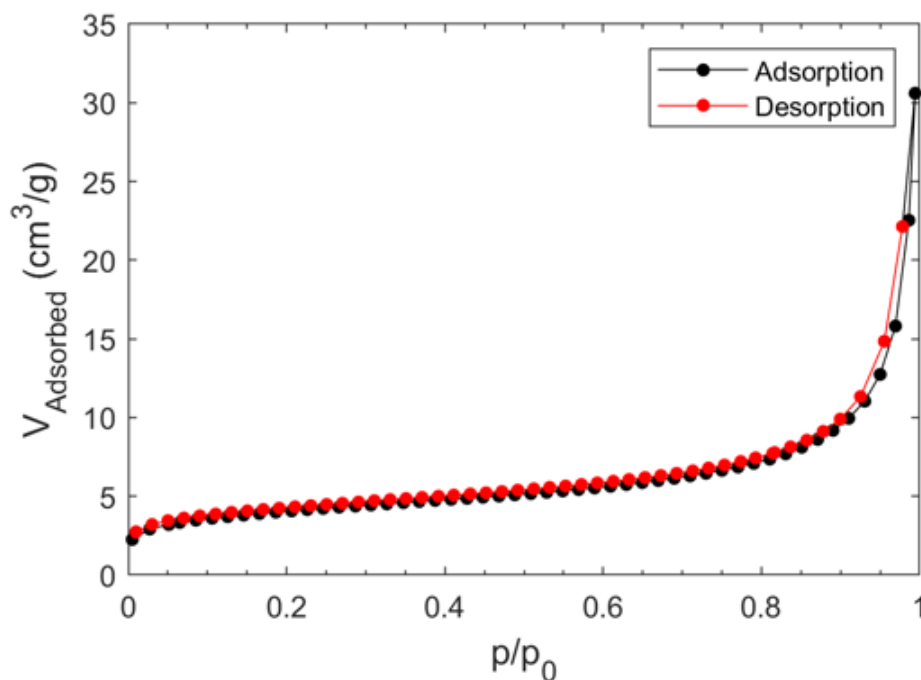


**Figure 3.22:** Adsorption and desorption isotherm of N<sub>2</sub> at 77 K on [Cu(1,3-YBDC)]·xH<sub>2</sub>O.

The data in the low N<sub>2</sub> partial pressure region was fitted with the BET model ( $R^2 = 0.99986$ ). The BET surface area was calculated to be  $14.5 \pm 0.8 \text{ m}^2/\text{g}$ , while the pore volume was  $46 \text{ mm}^3/\text{g}$ . The value obtained for the surface area was way lower than the one that is usually reported for tricarboxylate based MOFs. For example, the surface area of Cu-BTC MOFs is usually over  $1000 \text{ m}^2/\text{g}$ .<sup>14</sup> The main reasons for the low surface area and pore volume are:

- the presence of an extra coordination of Cu with the carbamate group of the linker that is reported to drop the surface area to  $100 \text{ m}^2$  and below;<sup>40</sup>
- the presence of trapped water molecules within the structure of the MOF, even after thermal activation and pre-treating, as suggested by the crystallochemical analysis;
- the presence of nanosized copper hydroxides and hydroxonitrates that can lower the channels accessibility.



The atomic composition of the surface of the samples is reported in the table below.

**Table 4.1:** superficial atomic compositions.

Sample	Atomic % values					% Au w/w
	C	N	O	Cu	Au	
MOF/Au5_1	63.2	3.6	28.8	3.6	0.21	2.68
MOF/Au10_1	63.2	3.8	29.0	3.0	0.33	4.24
MOF/Au50_1	59.5	4.5	31.6	3.4	0.29	3.67
MOF/Au12.2_1	64.4	4.4	27.7	2.8	0.22	2.88

The atomic percentage of gold increases from MOF/Au5\_1 to MOF/Au10\_1, whereas it remains near the same upon going to sample MOF/Au50\_1, possessing a higher nominal gold loading. This means that an increase of the amount of gold beyond 10% w/w does not increase the amount of gold retained by the MOF. The contribution of each oxidation state to the Au 4f signal for the sample MOF/Au5\_1 is reported in the table below:

**Table 4.2:** contribution % to the Au 4f signal in the sample MOF/Au5\_1.

Au(0)	Au (I)	Au (III)
22%	47%	31%

The 4f peaks of gold are subject to a split of 3.7 eV due to a phenomenon called spin-orbit splitting.<sup>41,42</sup> The Au 4f signal in the XPS spectra of MOF/Au5\_1 can be seen as the superposition of three peaks (Figure 4.1), each representing gold in a different oxidation state (table 4.3).

**Table 4.3:** Au 4f peaks in the sample MOF/Au5\_1.

Peak	BE (eV) (4f <sub>7/2</sub> , 4f <sub>5/2</sub> )	Oxidation state
Au 4f (VIII)	84.5, 88.3	0
Au 4f (IX)	85.4, 89.2	I
Au 4f (X)	86.4, 90.2	III

The Au 4f<sub>7/2</sub> photoelectron peak for a pure metallic Au(0) species is located at a value between 83.9 and 84.4 eV. Chang et al.<sup>43</sup> observed that the Au(0) 4f<sub>7/2</sub> peak shifts towards lower binding energies with the increase of particles size, attributing this phenomenon to

changes in the electronic structure of the particle. The slightly higher B.E. (84.6 eV) of the Au(0)  $4f_{7/2}$  in our sample could suggest the formation of small AuNPs on the MOF external surface. The presence of Au(III) and Au(I) showed that the MOF was able to retain these species, even after the sample was washed two times, but it also showed that the reduction was not complete.

Since the synthesis was performed in the presence of a primary alcohol, Au(III) could have been reduced by the solvent. In order to confirm that the propargylcarbamate group was responsible of the Au(0) formation, a Raman characterization was carried out (Figure 4.2). From the proposed reaction mechanism shown in scheme 1.1 the alkyne group should be lost and its Raman peak at  $2135\text{ cm}^{-1}$  should decrease in intensity.

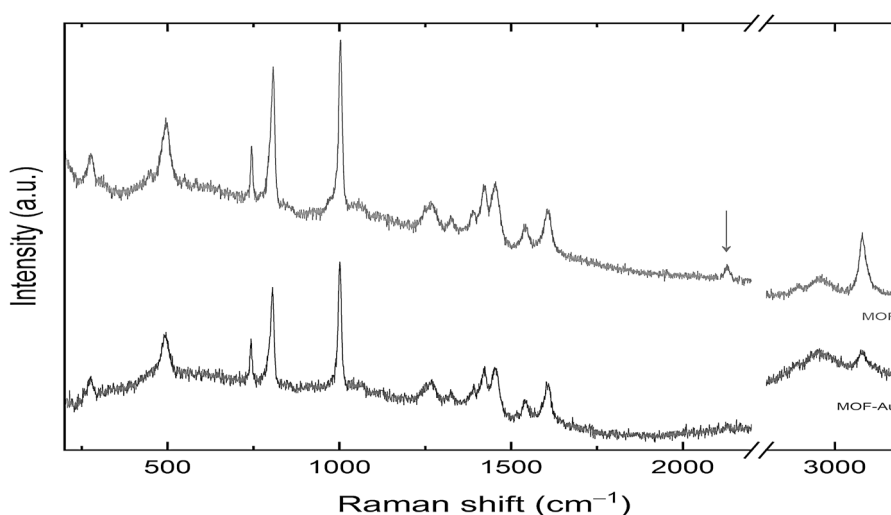


**Figure 4.2:** Raman spectra of the MOF (top); Raman spectra of the MOF after the  $\text{HAuCl}_4$  treatment (bottom).

As shown in Figure 4.2, the decrease of the alkyne peak intensity confirmed the Au(III) reduction by the linker of the MOF through the propargylcarbamate group. The samples MOF/Au5\_1, MOF/Au10\_1 and MOF/Au50\_1 were also analysed through AAS to determinate the total amount of gold in them (Table 4.4).

**Table 4.4:** Gold content in samples MOF/Au5\_1, MOF/Au10\_1 and MOF/Au50\_1.

Sample Name	sample quantity (mg)	Abs	Au concentration (ppm)	%Au w/w
MOF/Au5_1	9.4	0.121	3.04	3.22
MOF/Au10_1	10.2	0.193	4.90	4.80
MOF/Au50_1	3.0	0.150	3.79	12.60

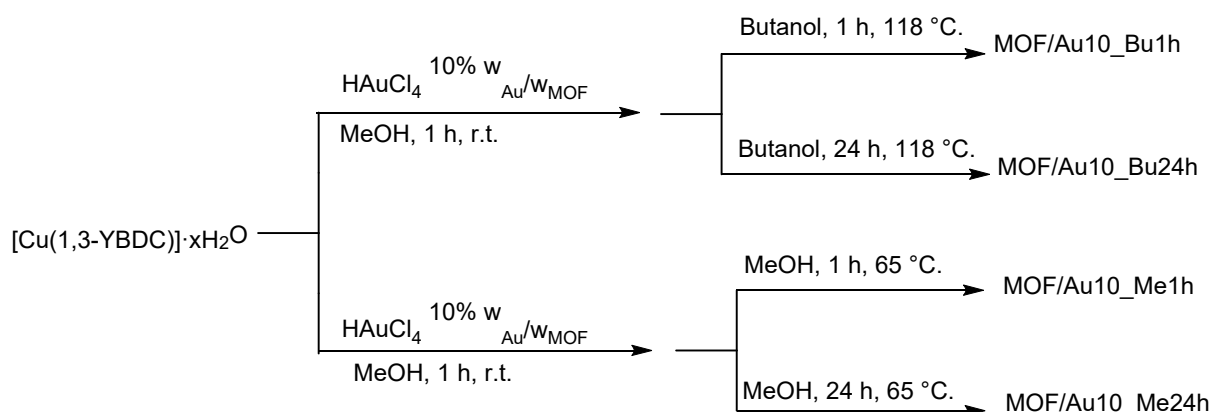
For samples MOF/Au5\_1 and MOF/Au10\_1, the percentage by weight of gold on the surface of the materials determined by XPS is approximately equal to the percentage by weight on the whole sample determined by AAS. This means that, in these two samples, gold seems to be evenly distributed between the external surface and the porosity of the material. For MOF/Au50\_1, the gold content determined by AAS is way higher than the one determined by XPS. Due to the low pore volume of the MOF and its low superficial area, it is unlikely for gold to be more present in the porosity rather than on the external surface. It is more likely that the sample was contaminated by massive gold that formed due to the reduction of  $\text{HAuCl}_4$  by the solvent (MeOH). This hypothesis is justified by the high loading of gold used in the synthesis of MOF/Au50\_1. This contamination could be also present in MOF/Au5\_1 and MOF/Au10\_1 as the evenly distribution of gold in the material is in contrast with the low surface area and low pore volume of the material.

The centrifugation of a Cu-MOF treated with  $\text{HAuCl}_4$  showed the presence of a heterogeneous mixture of phases (Figure 4.3) not evident if the sample is filtered on a Buckner funnel.



**Figure 4.3:** Solid phases separation by centrifugation: bulk gold (0) at the top and the MOF at the bottom.

This observation made clear that a new reaction protocol was necessary and therefore the procedure was changed as follows: first the MOF was stirred in a solution containing  $\text{HAuCl}_4$  at room temperature for 1 h in methanol under  $\text{N}_2$ , then all the  $\text{HAuCl}_4$  not adsorbed by the MOF was separated by centrifugation and the MOF thoroughly washed with methanol. Unlike what observed with the previous protocol, the centrifuged material appeared homogeneous. Afterwards, the resulting material was placed in a solvent under reflux to promote the reduction of the adsorbed Au(III). In this way only the Au(III) truly adsorbed inside the MOF is reduced (Scheme 4.2).



**Scheme 4.2:** [Cu(1,3-YBDC)]·xH<sub>2</sub>O reactions with HAuCl<sub>4</sub> using centrifugation in the work-up.

The samples MOF/Au10\_Bu1h, MOF/Au10\_Bu24h, MOF/Au10\_Me1h and MOF/Au10\_Me24h were analysed by AAS to determine the total amount of gold in them (Table 4.5). The procedure is described in detail in Section 2.2.

**Table 4.5:** Gold content in samples MOF/Au10\_Bu1h, MOF/Au10\_Bu24h, MOF/Au10\_Me1h and MOF/Au10\_Me24h.

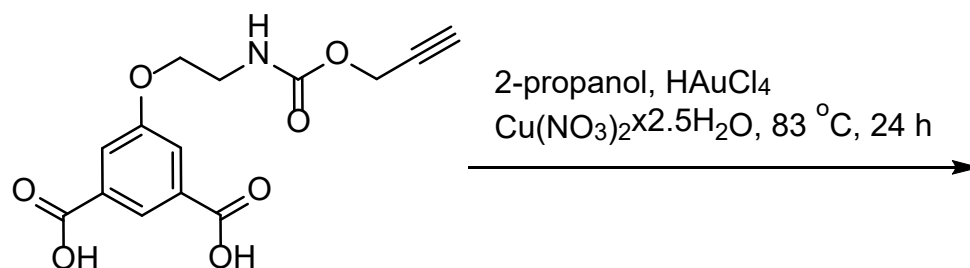
Sample	Weight of the sample (mg)	Abs	Au concentration (ppm)	%Au w/w
SAuMethanol_1h	10.5	0.018	0.62	0.29
SAuMethanol_24h	10.0	0.019	0.65	0.33
SAuButanol_1h	9.9	0.011	0.35	0.18
SAuButanol_24h	9.9	0.011	0.35	0.18

The gold content in these samples is way lower than that determined before on MOF/Au5\_1, MOF/Au10\_1, MOF/Au50\_1, and MOF/Au12.2\_1 and is also lower than the content found on MOF/Au5\_1, MOF/Au10\_1, MOF/Au50\_1, and MOF/Au12.2\_1 surfaces through XPS analysis. There is no significant distinction between the amount of gold in MOF/Au10\_Me1h and MOF/Au10\_Me24h. The same is also true for MOF/Au10\_Bu1h and MOF/Au10\_Bu24h. This means that the gold retained by the MOF does not leach out in 24 hours, indicating a strong interaction between the MOF surface and gold. XPS studies are currently in progress on these sample.

## 4.2 All in one pot synthesis

The crystallochemical analysis based on XRD data showed that the extra coordination of the carbamate group to copper could be the cause of the low surface area, low pore volume and cavity size. It also highlighted the fact that the cavities are too small to accommodate AuNPs, and that these particles could only form on the external surface. The purpose of adding H<sub>2</sub>AuCl<sub>4</sub> to the reaction mixture was to try to synthesize AuNPs before the MOF formation, so that the carbamate group is no longer present when the coordination of the ligand to copper occurs. If that is the case, the problem of the extra coordination could be solved and the MOF would already contain AuNPs in its cavities. Because no data on the reaction kinetics were obtained, two different experiments were performed:

- All in one pot synthesis **1 (AOPS1)**: where H<sub>2</sub>AuCl<sub>4</sub> was added to the reaction mixture containing 1,3-H<sub>2</sub>YBDC and Cu(NO<sub>3</sub>)<sub>2</sub>·2.5H<sub>2</sub>O (Scheme 4.3);



Scheme 4.3: AOPS1 reaction scheme.

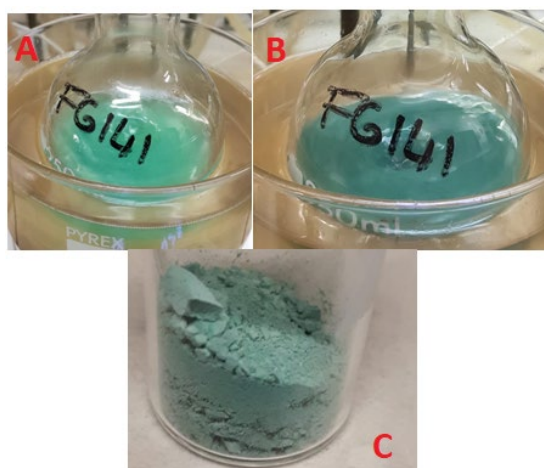
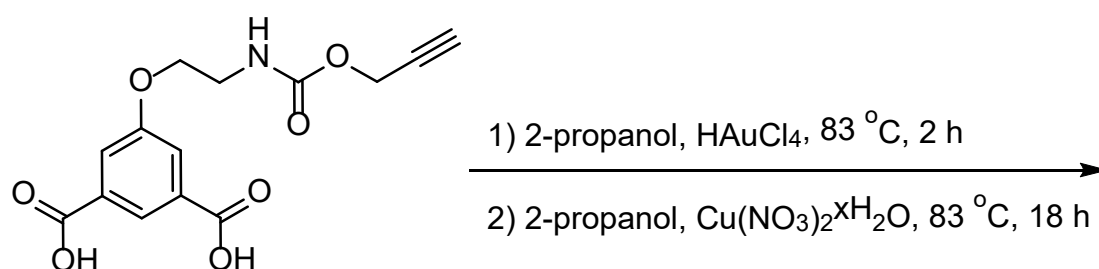
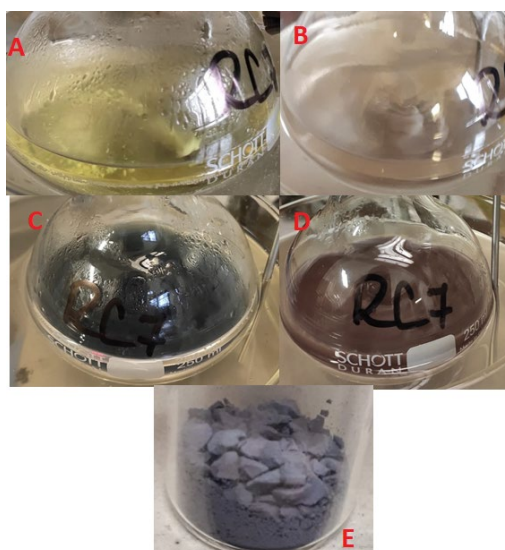


Figure 4.4: (A) reaction mixture at the start of the reaction; (B) reaction mixture at the end of the reaction; (C) solid obtained after work-up.

- All in one pot synthesis **2 (AOPS2)**: where Cu(NO<sub>3</sub>)<sub>2</sub>·2.5H<sub>2</sub>O was added after 2 h to a reaction mixture containing the linker 1,3-H<sub>2</sub>YBDC and H<sub>2</sub>AuCl<sub>4</sub>, in order to be sure that the Au(III) reduction would occur before the copper complexation (Scheme 4.4).



**Scheme 4.4:** AOPS2 reaction scheme.



**Figure 4.5:** (A) reaction mixture at the start of step 1; (B) reaction mixture at the end of step 1; (C) reaction mixture at the start of step 2; (D) reaction mixture at the end of step 2; (E) solid obtained after work-up.

The reduction of Au(III) by the solvent used for the synthesis is not uncommon. Yadav et al.<sup>44</sup> synthesized MOF-5 with the incorporation of AuNPs through the addition of H[AuCl<sub>4</sub>] in the reaction mixture. In their case, the reduction of Au (III) was performed by the aldehydic group of DMF, employed as the solvent with EtOH. In step 1 of AOPS2 reaction, 1,3-H<sub>2</sub>YBDC and H[AuCl<sub>4</sub>] were stirred at 83 °C for two hours; during this period the typical yellow colour of H[AuCl<sub>4</sub>] (Figure 4.5.A) faded to colourless (Figure 4.5.B). In order to observe if 2-propanol was able to reduce Au(III) in the same conditions as step 1 of the reaction AOPS2, a vial of 2-propanol containing H[AuCl<sub>4</sub>] was treated in the same way. The solution did not turn transparent as step 1 of the AOPS2 but remained yellow. Hence, it could be said that the reduction of Au(III) is mostly done by 1,2-H<sub>2</sub>YBDC.

The IR spectra of the products of the reaction AOPS1 and AOPS2 (Figure 4.6) are mostly similar to that of the previously synthesized MOF. The main difference can be observed in the 1500-1730 cm<sup>-1</sup> region of the spectra (Figure 4.7).

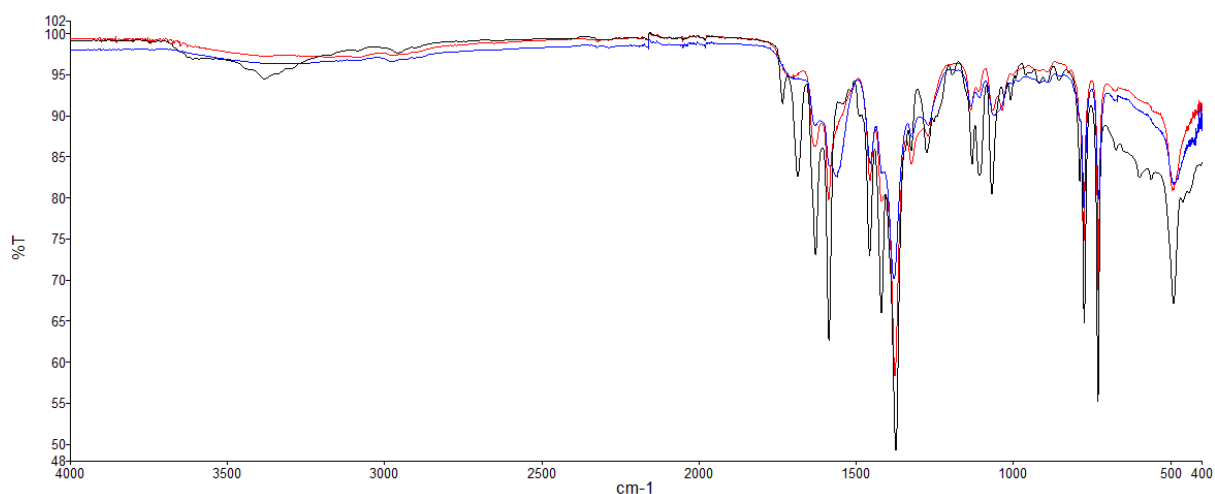


**Figure 4.6:** IR spectra of  $[\text{Cu}(1,3\text{-YBDC})]\cdot x\text{H}_2\text{O}$  (black line); IR spectra of the product of AOPS1 (blue line); IR spectra of the product of AOPS2 (red line).

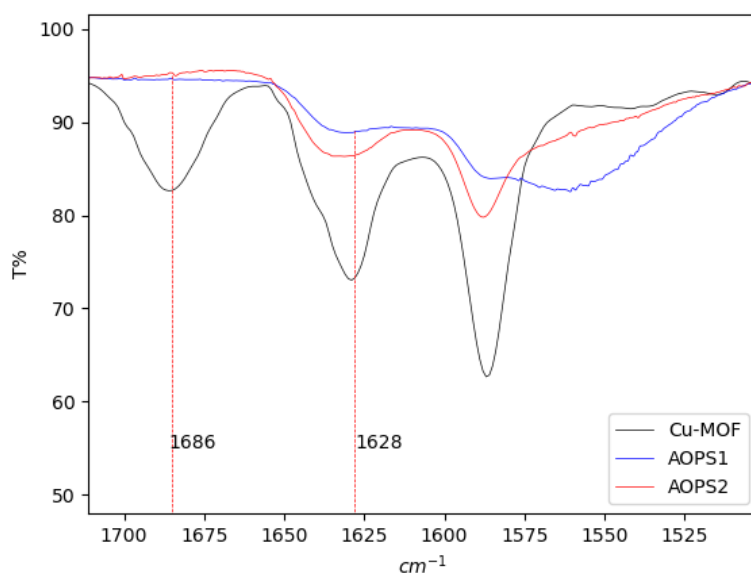


**Figure 4.7:**  $1500\text{-}1730\text{ cm}^{-1}$  region of the IR spectra of  $[\text{Cu}(1,3\text{-YBDC})]\cdot x\text{H}_2\text{O}$  (black line); product of AOPS1 (blue line); product of AOPS2 (red line).

The peak at  $731\text{ cm}^{-1}$  suggests the presence of Cu-O bonds in both samples, indicating that they are probably both MOFs. The peak at  $1628\text{ cm}^{-1}$ , attributed to the presence of carbamate groups coordinated to copper metal centers, is present in both AOPS1 and AOPS2 spectra, but it has a lower intensity. The presence of this peak can be explained by the fact that the amount of  $\text{HAuCl}_4$  (0.16 eq) was sub-stoichiometric in the AOPS1 and AOPS2 reaction mixtures. Because of that, most of 1,3- $\text{H}_2\text{YBDC}$  molecules did not react with Au(III) and their carbamate groups were able to coordinate copper as in  $[\text{Cu}(1,3\text{-YBDC})]\cdot x\text{H}_2\text{O}$ .

Also, it is unlikely that the products of AOPS1 and AOPS2 reactions are crystalline, as the linker is present in the reaction mixture in both its oxidised and un-oxidized forms. The peak at  $1686\text{ cm}^{-1}$ , present in both the linker and  $[\text{Cu}(1,3\text{-YBDC})]\cdot x\text{H}_2\text{O}$  infrared spectra completely disappears in those of AOPS1 and AOPS2 reaction products. This could indicate the presence of carbamate groups inside  $[\text{Cu}(1,3\text{-YBDC})]\cdot x\text{H}_2\text{O}$  that are not coordinated to copper metal centres, which are likely situated on the external surface of the material.

These findings further confirm what was previously observed in a preliminary study carried out by dissolving equimolar amounts of 1,3- $\text{H}_2\text{YBDC}$  and  $\text{HAuCl}_4\cdot 3\text{H}_2\text{O}$  in  $\text{CD}_3\text{OD}$  in a J.Young NMR tube at room temperature. The reaction, monitored by  $^1\text{H}$  and  $^{13}\text{C}$  NMR spectroscopy, showed that within 24 h the peaks attributed to the propargyl group  $-\text{C}(\text{O})\text{OCH}_2\text{C}\equiv\text{CH}$  [ $^1\text{H}$  NMR: 4.67 (d), 2.85 (t);  $^{13}\text{C}$  NMR: 159.0, 79.6, 75.8, 53.2 ppm] completely disappeared leaving two triplets at 4.12 (68.5) and 3.52 (41.40) ppm assigned to the  $-\text{OCH}_2\text{CH}_2\text{NH}_2$  moiety. The transformation of 1,3- $\text{H}_2\text{YBDC}$  into 5-(2-aminoethoxy)isophthalic acid (Figure 4.8) was further confirmed by the ESI (+/-) MS analyses of the crude material. These observations are also perfectly in accordance with our previous SSNMR study.<sup>45</sup>

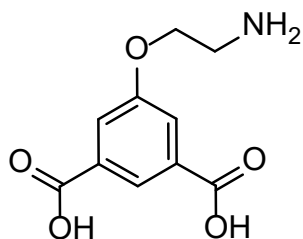


**Figure 4.8:** 5-(2-aminoethoxy)isophthalic acid.

## CHAPTER 5

### 5 Electrochemical characterization and applications of [Cu(1,3-YBDC)]·xH<sub>2</sub>O

A Glassy Carbon (GC) electrode coated with [Cu(1,3-YBDC)]·xH<sub>2</sub>O (hereafter abbreviated **GC/Cu-MOF**, Fig 5.1B) was characterized electrochemically through cyclic voltammetry in different electrolyte solutions. Successively, such modified electrode was employed as a nitrite sensor.

Due to the affinity of gold to the alkyne group of the MOF's linker, the GC/Cu-MOF electrode was successively modified through AuNPs incorporation. The electrode named **GC/Cu-MOF/Au** was prepared by making the MOF deposited on the electrode surface to adsorb Au(III) from a HAuCl<sub>4</sub> solution and then, after washing the electrode with ethanol, the Au(III) retained by the MOF was reduced to Au(0) through the application of a potential of 0.05 V. The GC/Cu-MOF/Au electrode was also characterized and tested for nitrite detection.

In order to acquire SEM images of **GC/Cu-MOF** and **GC/Cu-MOF/Au** screen printed electrodes (SPEs) were also used (Figure 5.1C).

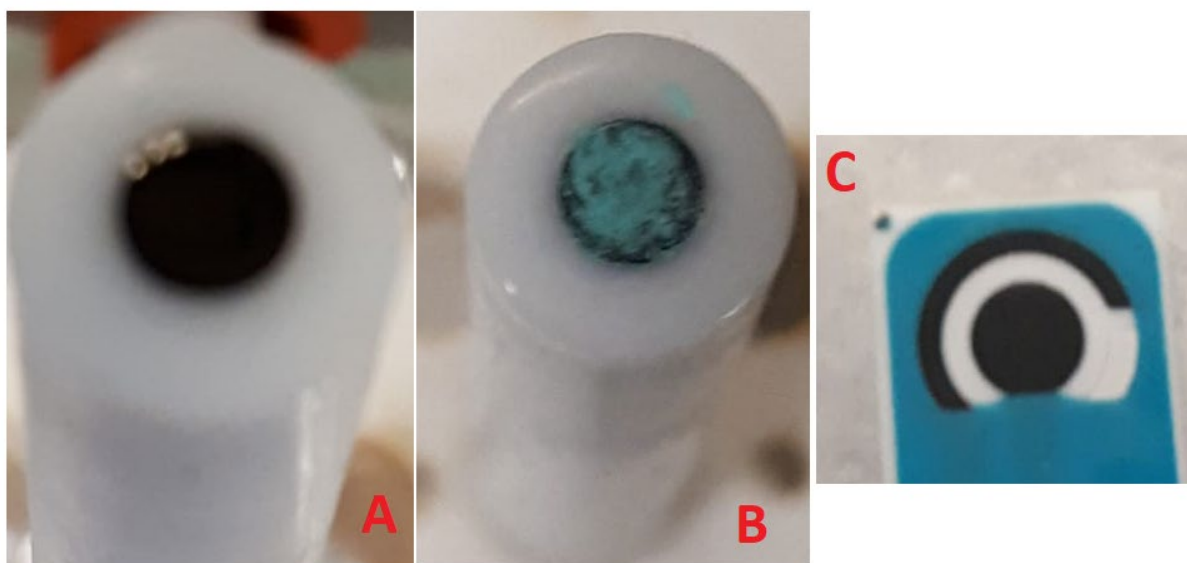


**Figure 5.1:** (A) Bare GC electrode; (B), GC/Cu-MOF electrode; (C) Screen printed electrode.

## 5.1 GC/Cu-MOF SEM-EDX

A SEM analysis was performed on modified SPEs (see Section 2.7) before the electrochemical characterization. Figure 5.2 shows the SEM of Cu-MOF deposited on a glassy carbon surface in which the lamellar structure of  $[\text{Cu}(1,3\text{-YBDC})]\cdot x\text{H}_2\text{O}$  is barely distinguishable (Figure 5.2.A).

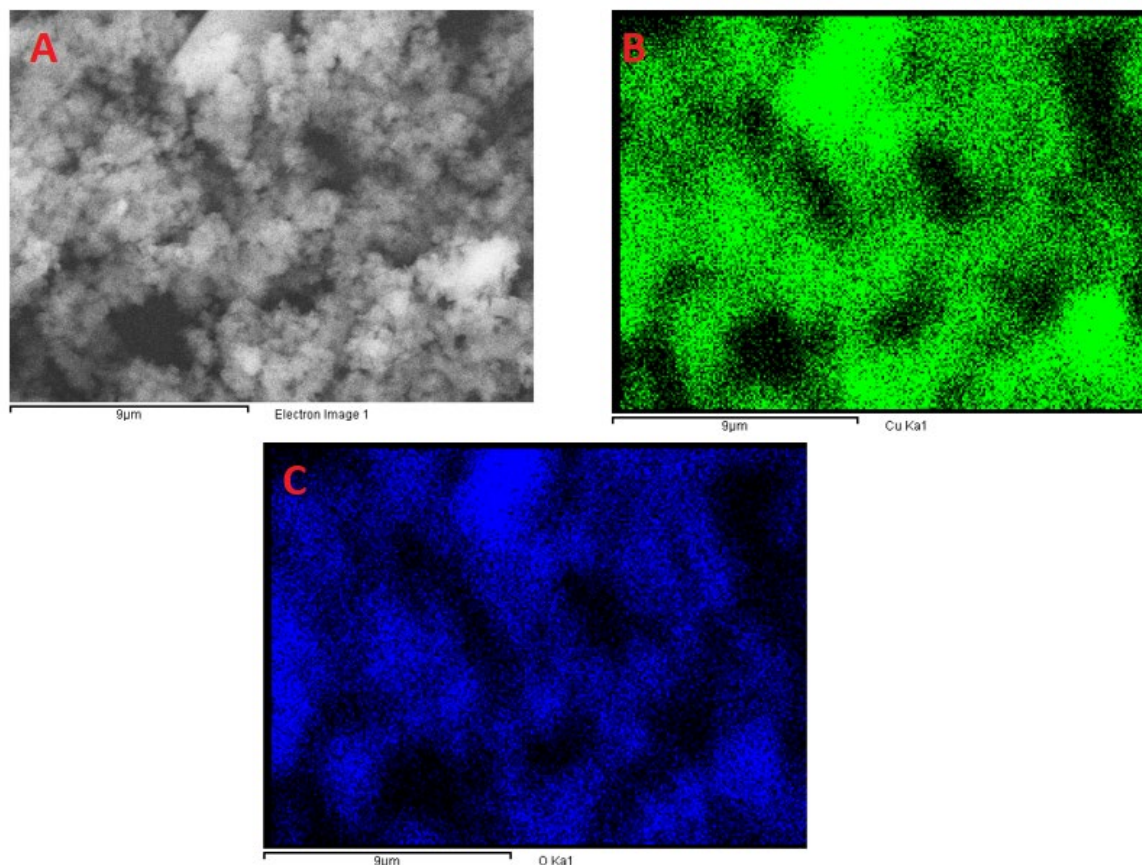


**Figure 5.2:** (A) SEM image of a GC/Cu-MOF electrode surface (B) mapping of copper, (C) mapping of oxygen.

## 5.2 GC/Cu-MOF electrochemical characterization

The electrochemical behaviour of GC/Cu-MOF was preliminary studied in different electrolyte solutions: (i) NaCl 0.1 M; (ii) Tris(hydroxymethyl)aminomethane (TRIS) buffer (pH 7.2) 0.1 M; (iii) PBS buffer (pH 7.2) 0.1 M. The cyclic voltammogram of the GC/Cu-MOF electrode in NaCl 0.1 M electrolyte solution is shown in Figure 5.3.

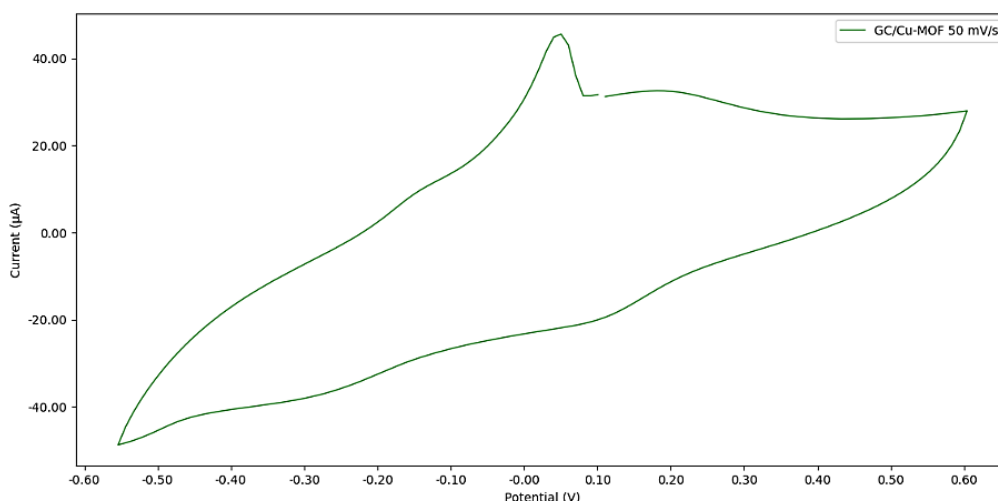


**Figure 5.3:** CV of GC/Cu-MOF at a scan-rate of 50 mV/s in NaCl 0.1 M electrolyte solution.

A table containing peak potentials is showed below:

**Table 5.1:** peaks table for GC/Cu-MOF in NaCl 0.1M electrolyte solution at 50 mV/s.

Potential (V)	Description
<b>Oxidation peaks</b>	
-0.15	Cu(0)-Cu(I)
0.05	Cu(0)-Cu(II), stripping
0.20	Cu(I)-Cu(II)
<b>Reduction peaks</b>	
0.10	Cu(II)-Cu(I)
-0.27	Cu(I)-Cu(0)

In the cathodic part of the voltammetric path two peaks at 0.10 and -0.27 V are visible, attributable to the reduction from Cu(II) to Cu(I) and from Cu(I) to Cu(0), respectively. The Cu(I) redox peaks at 0.10 V is due to the ability of Cl<sup>-</sup> ions to stabilize copper in the +1 oxidation state through complexation.<sup>46</sup> In the anodic part of the voltammetric path a sharp oxidation peak at 0.05 V due to the oxidation of Cu(0) is well evident.

A cyclic voltammogram of the GC/Cu-MOF electrode in TRIS buffer 0.1 M (pH 7.2) is shown in Figure 5.4.

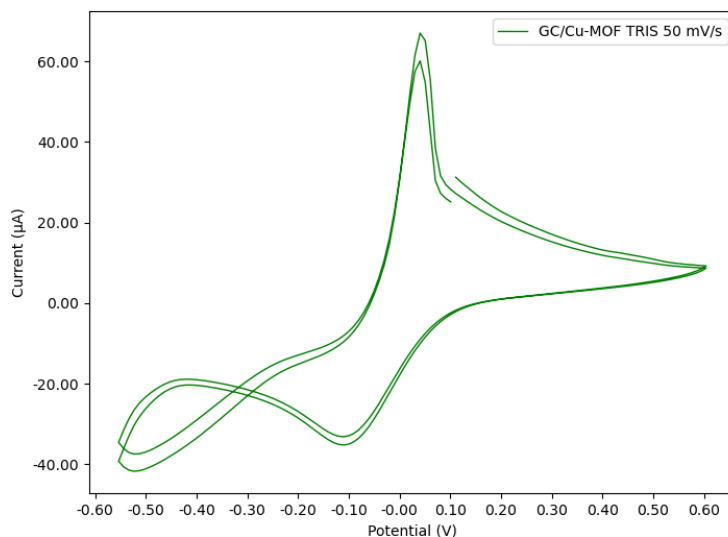


**Figure 5.4:** CV of GC/Cu-MOF at a scan-rate of 50 mV/s in TRIS buffer 0.1 M (pH 7.2).

Even in this case, the presence of  $\text{Cl}^-$  ions stabilized the Cu(I) redox peaks at a potential of -0.10 V. In table 5.2 are reported the peak potentials.

**Table 5.2:** peaks table for GC/Cu-MOF in TRIS buffer 0.1M (pH 7.2) at 50 mV/s.

Potential (V)	Description
<b>Oxidation peaks</b>	
-0.24	Cu(0)-Cu(I)
0.05	Cu(0)-Cu(II), stripping
<b>Reduction peaks</b>	
-0.10	Cu(II)-Cu(I)
-0.52 during anodic scan	Cu(I)-Cu(0)

The main difference between the CVs made in NaCl and in TRIS buffer is in the cathodic peak positions. In TRIS buffer, both reduction peaks are shifted toward higher cathodic potentials and this could be explained by the slow diffusion of the counter-ion  $\text{TRIS}^+$  within the small pores of the MOF during copper reduction.

The electrochemical behaviour of GC/Cu-MOF electrodes in PBS buffer solutions were also studied. PBS 0.1M electrolyte solutions are typically used for nitrite oxidation

experiments.<sup>29,47</sup> The choice of working at pH 7.2 was based on the stability of the MOF: as reported in the introduction (Section 1.4.1), low pH values could lead to MOF deterioration due to protonation of the linker (Figure 5.5 B), while high pH values could lead to copper oxides and hydroxides formation (Figure 5.5 A).

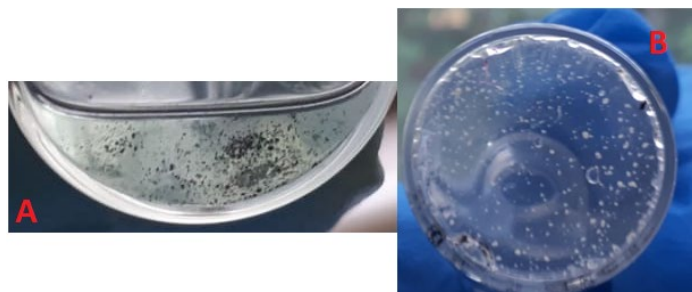


**Figure 5.5:** MOF in a (A) 1M NaOH aqueous solution; (B) MOF in a 0.5M H<sub>2</sub>SO<sub>4</sub> aqueous solution.

The voltammetric path in this electrolyte results different as reported in Figure 5.6 only the Cu(0)-Cu(II) oxidation peak at 0.00 V, and the Cu(II)-Cu(0) reduction peak at -0.2 V are well evident.

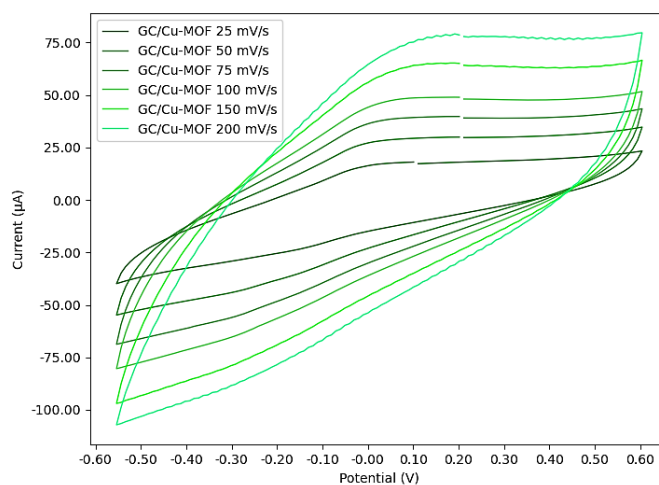


**Figure 5.6:** CVs of GC/Cu-MOF electrode at different scan-rates from 25 mV/s to 200 mV/s in 0.1M PBS (pH 7.2).

In order to investigate the effect of cycling in a 0.1 M PBS (pH 7.2) buffer solution on the GC/Cu-MOF electrode we have studied the surface with SEM microscopy after 100 cycling at 50 mV/s (Figure 5.7)

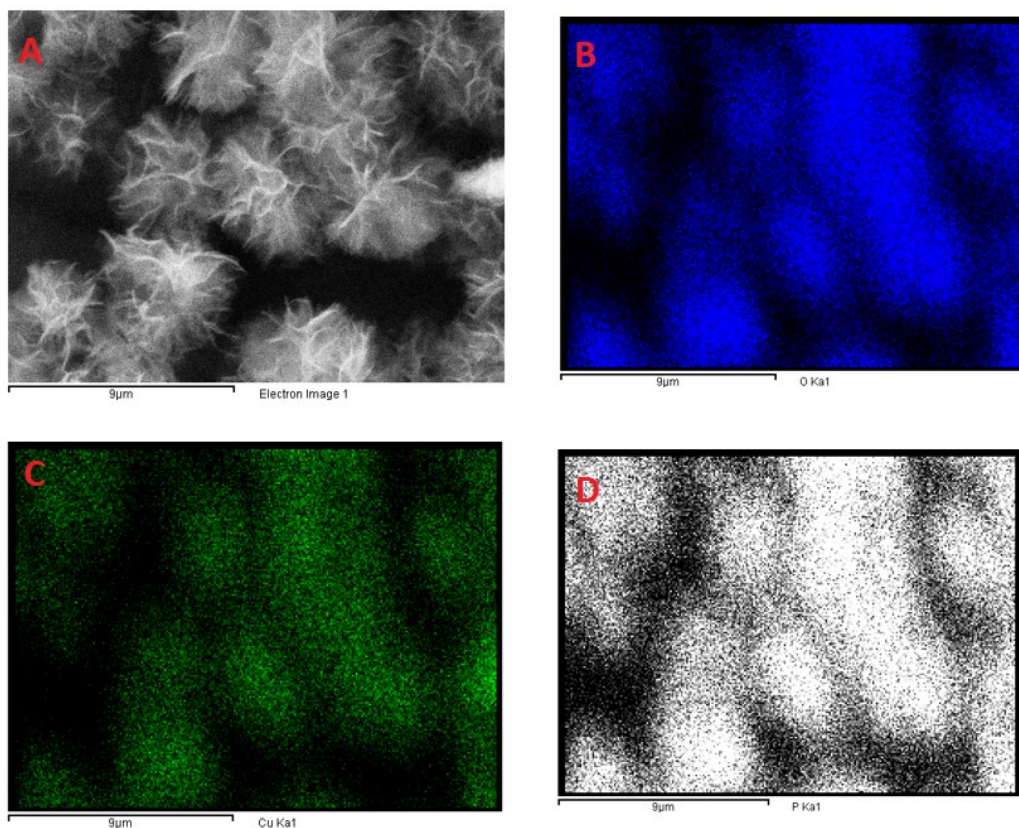


**Figure 5.7:** (A) SEM image of  $[\text{Cu}(1,3\text{-YBDC})]\cdot x\text{H}_2\text{O}$  on a glassy carbon screen-printed electrode after 100 cycles in 0.1 M PBS (pH 7.2) at a scan-rate of 50 mV/s; (B) mapping of copper, (C) mapping of oxygen; (D) mapping of phosphorus.

After being exposed to the PBS electrolyte solution the surface results are very different from the one of  $[\text{Cu}(1,3\text{-YBDC})]\cdot x\text{H}_2\text{O}$  in Figure 3.18 and 5.2.A, and it seems very similar to the one of copper phosphate reported in literature.<sup>48</sup> The EDX mapping, shown in Figure 5.7.D, put in evidence the presence of phosphorus in the exact same spots where copper and oxygen are present.

## 5.3 Nitrite oxidation

### 5.3.1 Nitrite oxidation on a glassy carbon electrode

The performance of the GC electrode towards nitrite oxidation was performed through cyclic voltammetry at a scan-rate of 50 mV/s in a PBS 0.1M (pH 7.2) electrolyte solution. As shown in Figure 5.8, the nitrite oxidation peak reaches a maximum at 0.997 V at a scan-rate of 50 mV/s.

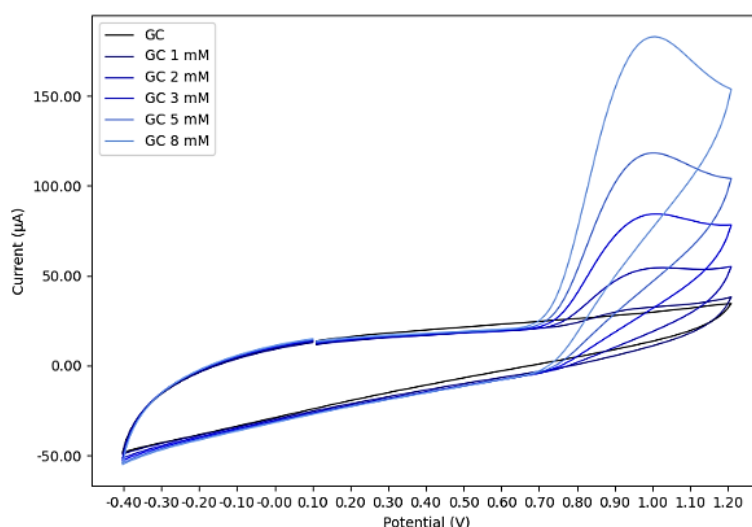


**Figure 5.8:** CV of GC electrode at different nitrite concentrations, from 0 to 8 mM.

No reduction peak was observed. Kozub et al.<sup>49</sup> reported that the nitrite oxidation is a one-electron reaction that leads to nitrogen dioxide formation, which rapidly disproportionate in water to yield nitrite and nitrate ions. The EC mechanism (eq. 5.1 and 5.2),<sup>49</sup> with a fast chemical reaction, could explain the absence of a reduction peak in the CVs.



The need for a buffer solution is justified by the release of  $\text{H}^+$  ions from the disproportionation reaction, as a change of pH during the analysis could affect its reproducibility.

In order to acquire more information on the nitrite oxidation reaction at the GC electrode, CVs at different scan-rate were performed while nitrite 5 mM was present in the electrolyte solution (Figure 5.9).

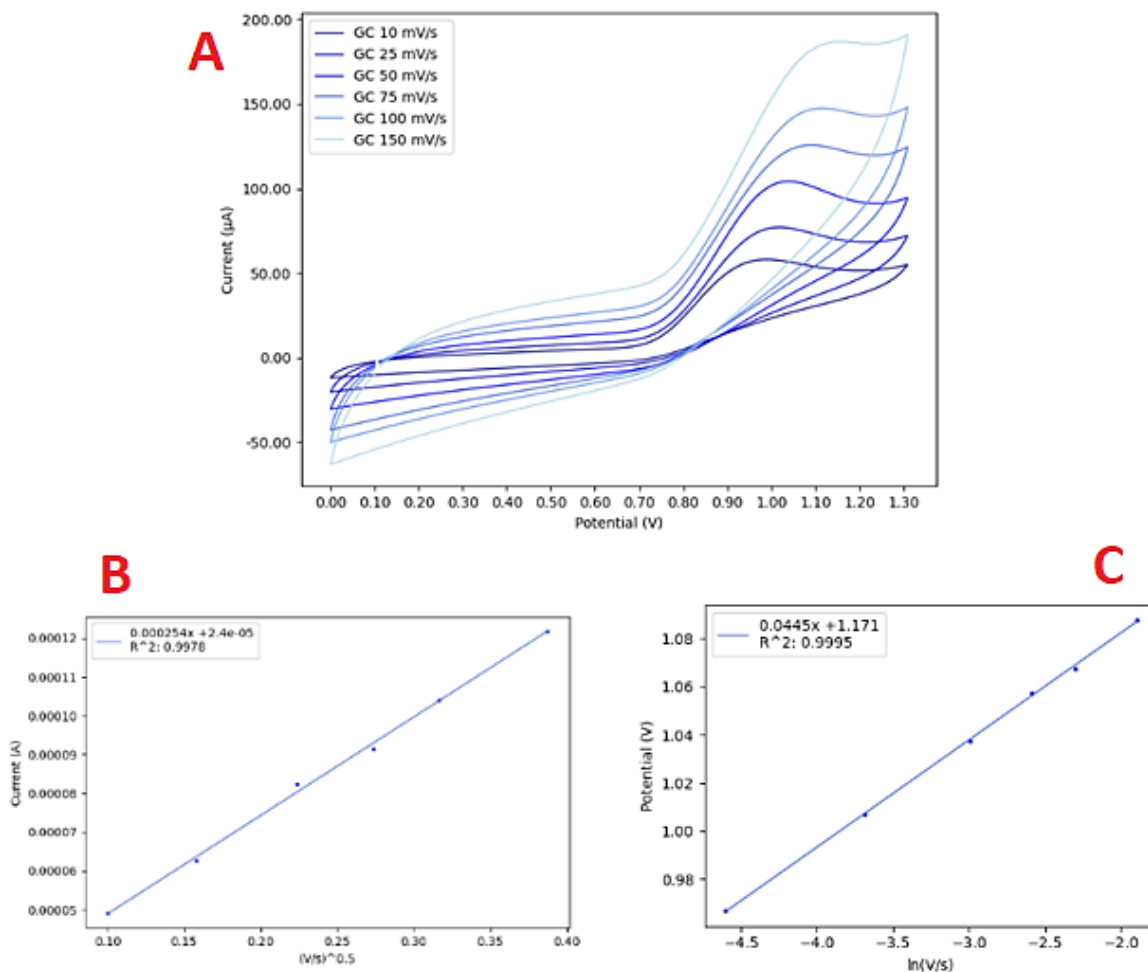


**Figure 5.9:** (A) CVs at different scan-rates from 10 mV/s to 150 mV/s, nitrite 5 mM, PBS 0.1M (pH 7.2);  
 (B) correlation between peak current and square root of the scan-rate;  
 (C) correlation between peak potential and natural logarithm of the scan-rate.

Equations 5.3 and 5.4 describe the effect of the scan rate on peak potential ( $E_{pa}$ ) and peak current ( $I_{pa}$ ) for an irreversible reaction.<sup>50</sup>

$$E_{pa} = E0' + \frac{RT}{\beta F} \left[ 0.780 + \ln \left( \frac{\sqrt{D_r}}{k_0} \right) + \ln \ln \left( \sqrt{\frac{\beta F}{RT}} \right) \right] + \frac{RT}{2\beta F} \ln(\nu) \quad (5.3)$$

$$I_{pa} = 0.4958 \sqrt{\frac{\beta F}{RT}} F A C_r^* \sqrt{D_r} \sqrt{\nu} \quad (5.4)$$

Where  $E0'$  is the formal potential of the redox couple,  $R$  is the gas constant,  $T$  is the temperature,  $D_r$  is the diffusion coefficient of the reduced species,  $C_r^*$  is the concentration of the reduced species in the bulk of the solution,  $\nu$  is the scan-rate and  $A$  is the area of the electrode.

The peak potential of nitrite oxidation on the GC electrode is a linear function of the natural logarithm of the scan-rate ( $R^2 = 0.9995$ , slope =  $0.0445 \text{ V}/\ln(\text{V}/\text{s})$ , intercept =  $1.171 \text{ V}$ ). For this reason, the reaction appears to be irreversible, meaning that the electron transfer process is the limiting step, being way slower than nitrite diffusion. The peak current shows a linear correlation with the square root of the scan-rate ( $R^2 = 0.9978$ , slope =  $2.54 \times 10^{-4} \text{ A}/\sqrt{\text{V}/\text{s}}$ , intercept =  $2.4 \times 10^{-5} \text{ A}$ ). This means that nitrite ions were freely diffusing species. They were not adsorbed on the GC electrode surface before exchanging electrons.<sup>51,49,52</sup>

### 5.3.2 Nitrite oxidation on GC/Cu-MOF and GC/Cu-MOF/Au

Both GC/Cu-MOF and GC/Cu-MOF/Au electrodes were tested as sensors in PBS 0.1M (pH 7.2) solution, at 50 mV/s in presence of nitrite 5 mM. The CVs paths are reported in Figure 5.10.

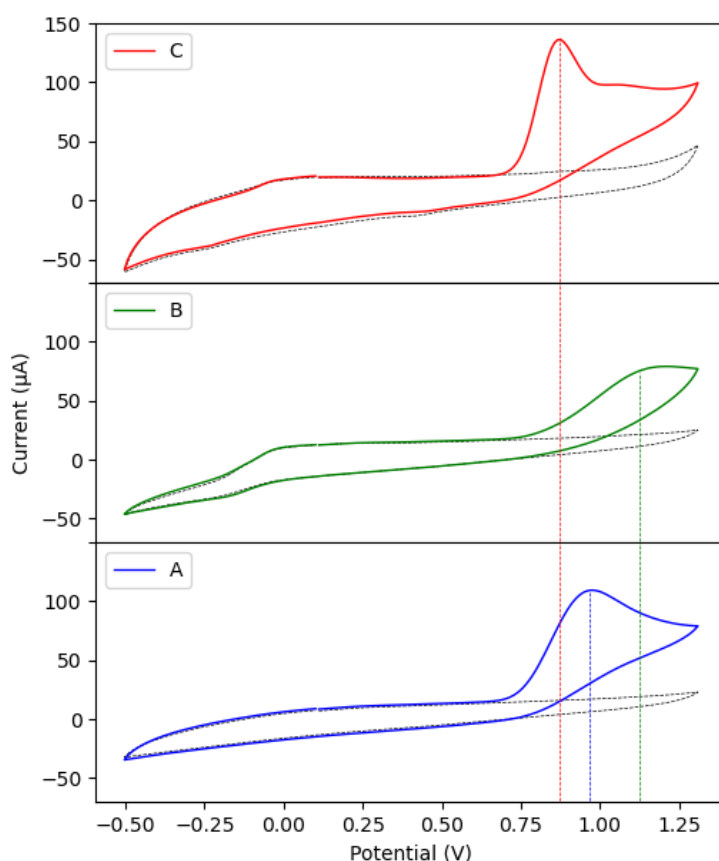


**Figure 5.10:** CVs at 50 mV/s in 0.1 M PBS (pH 7.2) contains 5 mM nitrite on: C) GC/Cu-MOF/Au; B) GC/Cu-MOF; A) bare GC electrode.

In table 5.3 the nitrite oxidation peak potential is reported for each electrode.

**Table 5.3:** nitrite oxidation peak potentials.

Electrode	Nitrite oxidation peak potential (V)
GC	0.97
GC/Cu-MOF	1.13
GC/Cu-MOF/Au	0.87

The higher peak potential for nitrite oxidation observed with GC/Cu-MOF, is probably due to the low conductivity and low pore volume of our MOF. On the contrary the presence of Au nanoparticles gives a shift of the oxidative potential towards a lower value.

As a blank test (Figure 5.11), we compared the CV of a GC electrode modified with Au nanoparticles (GC/Au) following the procedure reported in Section 2.8.2.

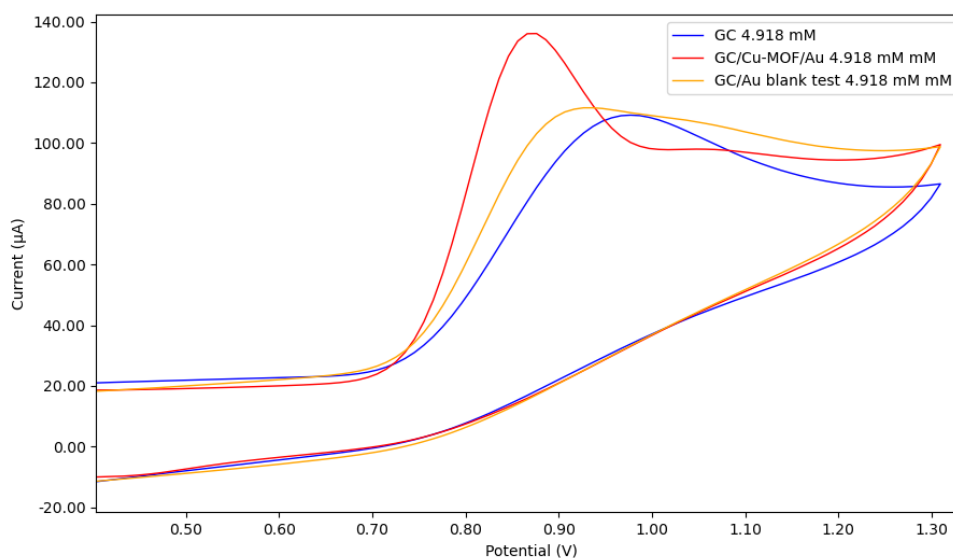


**Figure 5.11:** 50 mV/s in PBS 0.1M (pH 7.2) in the presence of nitrite 5 mM; (red) GC/Cu-MOF/Au; bare GC (blue); glassy carbon electrode modified for the blank test (orange).

In respect with GC, the GC/Au electrode shows a lower nitrite oxidation peak. However, only when GC/Cu-MOF/Au was used, an increase in the current and a significant shift in the

potential became evident. This suggest a synergic effect between the Cu-MOF and the AuNPs.

CVs at different scan-rates were performed in PBS buffer electrolyte solution with 5 mM nitrite concentration. The results are reported in Figure 5.12.

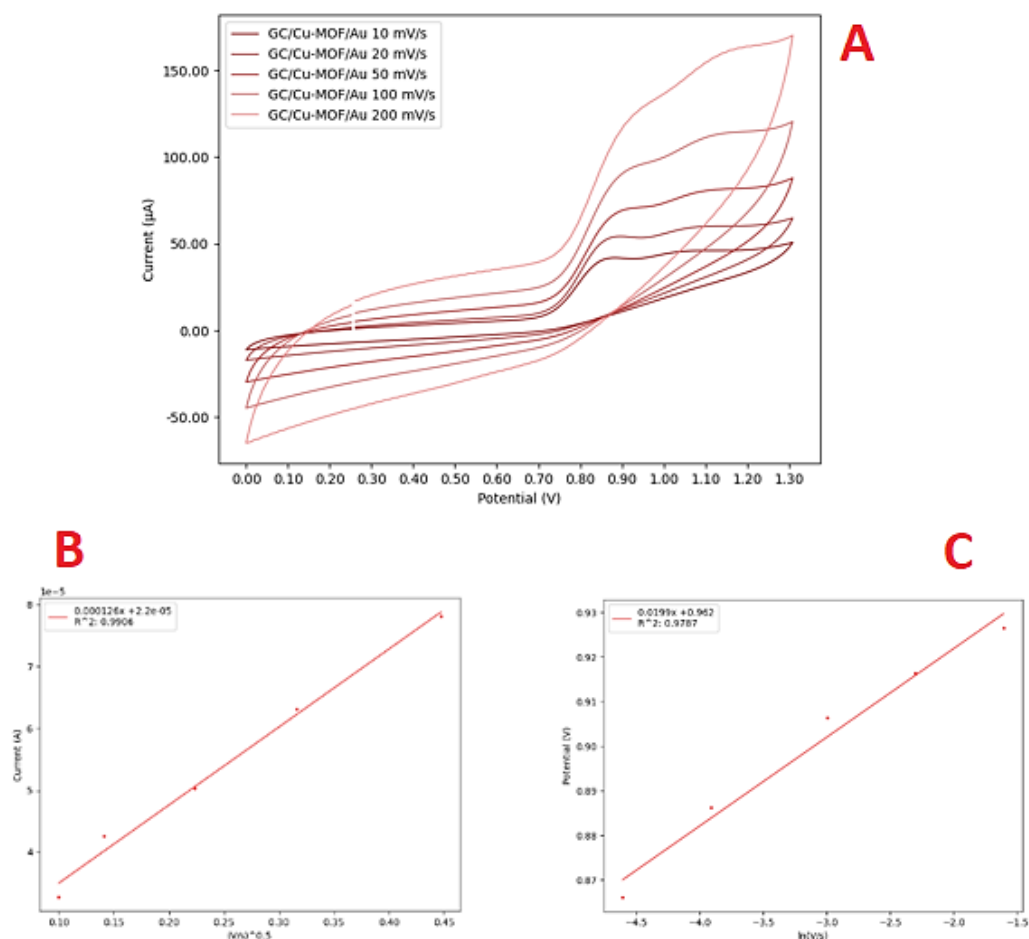


**Figure 5.12:** (A) CVs of GC/Cu-MOF/Au electrode at different scan-rates from 10 to 200 mV/s in PBS 0.1M (pH 7.2) with nitrite 5mM; (B) correlation between peak current and square root of the scan-rate; (C) correlation between peak potential and natural logarithm of the scan-rate.

The peak current for the oxidation of nitrite shows a linear correlation with the square root of the scan rate ( $R^2 = 0.9906$ , slope =  $0.000126 \text{ A}/\sqrt{\text{V/s}}$ , intercept =  $2.2 \times 10^{-5} \text{ A}$ ), confirming a diffusive process. The peak potential for nitrite oxidation slightly shifts toward higher oxidation potentials with the increase of the scan rate. The correlation of the peak potential is linear with the natural logarithm of the scan rate ( $R^2 = 0.9787$ , slope =  $0.0191 \text{ V}/\ln(\text{V/s})$ , intercept =  $0.962 \text{ V}$ ), meaning that the electron transfer step is still the slowest step. The shift of the oxidation peak towards lower anodic potentials found for the GC/Cu-MOF/Au electrode can be attributed to the acceleration of the charge transfer caused by the AuNPs.

Chronoamperometric tests were performed with different nitrite additions in PBS 0.1M (pH 7.2), at an applied potential of 0.9 V under stirring with GC, GC/Cu-MOF and GC/Cu-MOF/Au electrodes. The results are reported in Figures 5.13 and 5.14 and Table 5.3.

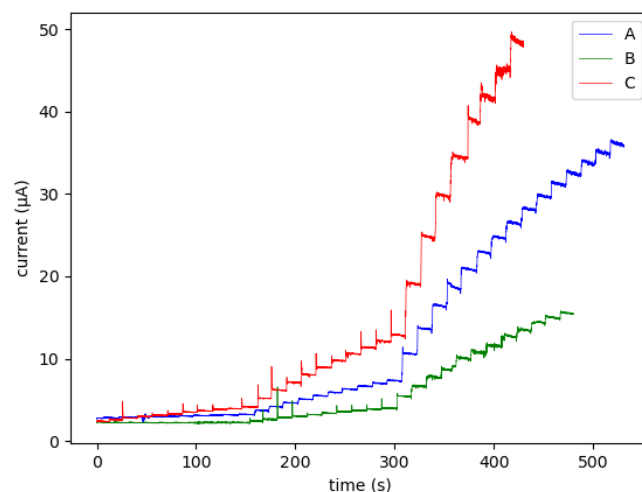


**Figure 5.13:** Chronoamperometric response of A) GC (blue), B) GC/Cu-MOF (green), C) GC/Cu-MOF/Au (red).

**Table 5.3:** Slopes, intercepts,  $R^2$ , linearity ranges and LODs of the different electrodes.

Electrode	Slope ( $\mu\text{A mM}^{-1} \text{cm}^{-2}$ )	Intercept ( $\mu\text{A}$ )	$R^2$	Linearity range ( $\mu\text{M}$ )	LOD ( $\mu\text{M}$ )
<b>GC</b>	(2) 59.59	(2) 2.50	(2) 0.9975	(2) 160-1200	36
	(3) 44.12	(3) 4.73	(3) 0.9916	(3) 1200-8000	
	(1) 24.92	(1) 1.98	(1) 0.9929	(1) 160-1200	
<b>GC/Cu-MOF</b>	(3) 20.18	(3) 2.66	(3) 0.9932	(3) 1200-8000	67
	(2) 24.92	(2) 1.98	(2) 0.9929	(2) 160-1200	
	(1) 24.92	(1) 1.98	(1) 0.9929	(1) 160-1200	
<b>GC/Cu-MOF/Au</b>	(3) 96.63	(3) 5.49	(3) 0.9955	(3) 1200-5000	5
	(2) 126.46	(2) 2.56	(2) 0.9953	(2) 160-1200	
	(1) 129.58	(1) 2.42	(1) 0.9986	(1) 20-160	

*\*(1) linear regression performed in the 20-160  $\mu\text{M}$  concentration range; (2) linear regression performed in the 160-1200  $\mu\text{M}$  concentration range; (3) linear regression performed for concentrations higher than 1200  $\mu\text{M}$*

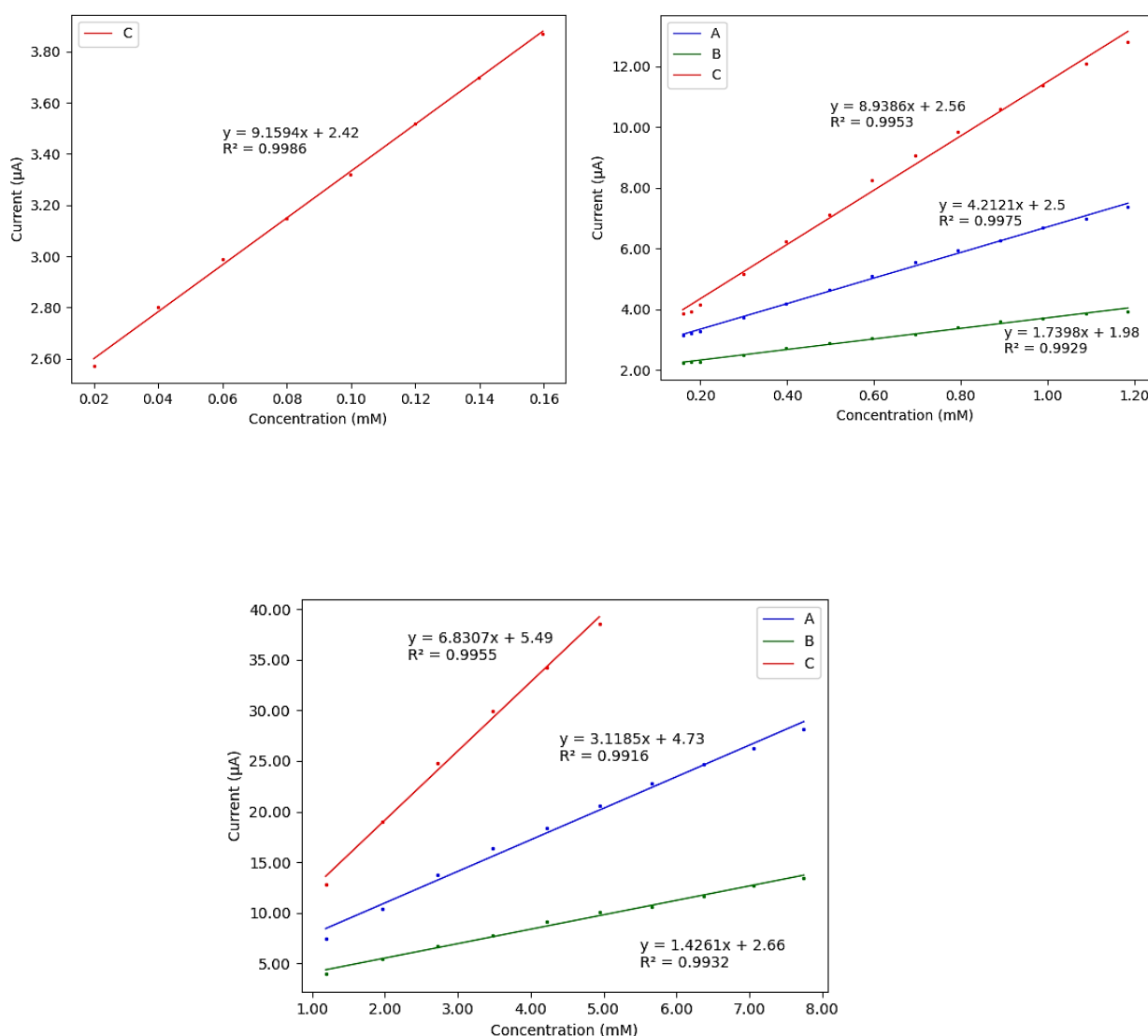


**Figure 5.14:** Calibration curves: GC/Cu-MOF/Au (red, C); GC/Cu-MOF (green, B); bare GC (blue, A).

The results agree with the ones observed with cyclic voltammetry. The sensitivity of the GC/Cu-MOF/Au electrode toward nitrite is higher (more than double) than both the GC and GC/Cu-MOF electrode. Moreover, a lower LOD (calculated as  $\text{LOD} = 3.3\sigma$  where  $\sigma$  is the standard deviation of the intercept)<sup>53</sup> is obtained with GC/Cu-MOF/Au electrode. The LOD value around one order of magnitude higher than those reported in literature for similar modified electrodes could be due to the lower porosity of this MOF.

#### 5.4 EIS characterization

To better understand the electrochemical behaviour of the electrodes, the impedance spectra of the GC, GC/Cu-MOF, GC/Cu-MOF/Au electrodes were acquired from  $10^5$  to 1 Hz at an equilibrium potential of 0.22 V. The potential amplitude applied to the electrodes was 10 mV.

The electrolytic solution utilized was KCl 0.1 M containing  $K_4Fe(CN)_6$  2 mM. The choice of  $K_4Fe(CN)_6$  as an electroactive species was based on its well-known reversible behaviour. The results and equivalent circuit are reported in Figure 5.15 and 5.16 respectively.

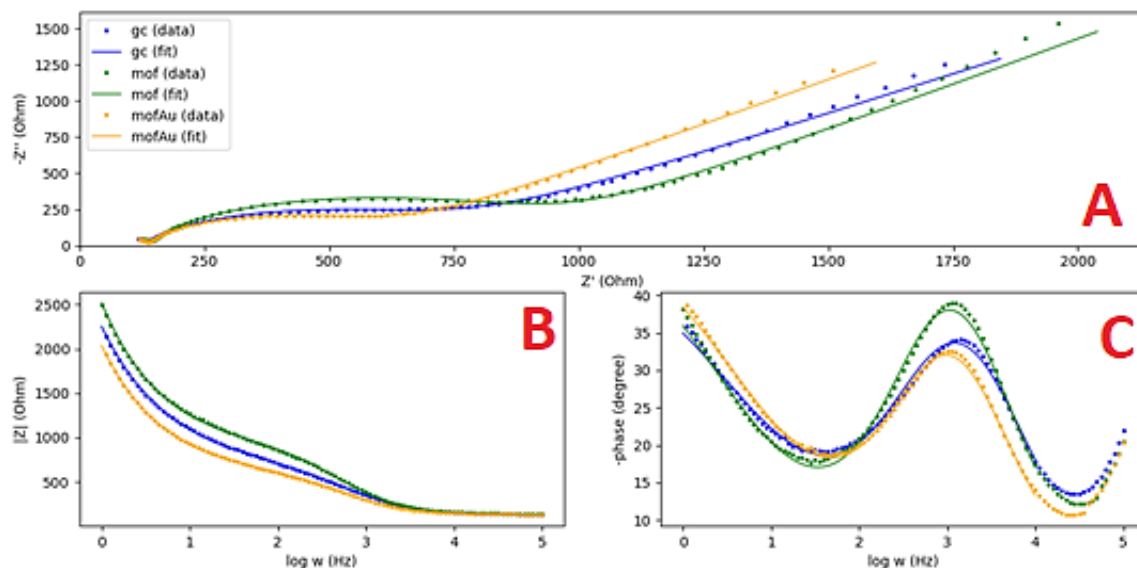


**Figure 5.15:** (A) Nyquist plot for the GC (blue), GC/Cu-MOF (green), GC/Cu-MOF/Au (orange) electrodes: dotted line = impedance data, continuous line = fitted model; (B) impedance module against the base 10 logarithm of the frequency; (C) phase plot.

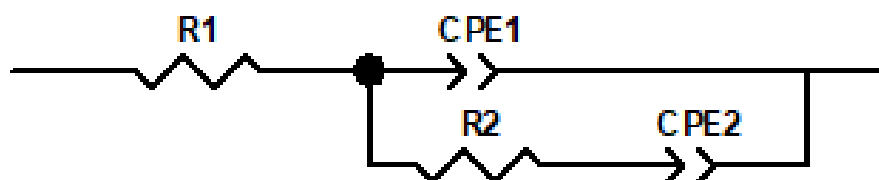


**Figure 5.16:** equivalent circuit used to fit impedance data.

**Table 5.4:** fitting parameters for the equivalent circuit.

	GC	GC/Cu-MOF	GC/Cu-MOF/Au
<b>R1 (<math>\Omega</math>)</b>	123.5	137.3	131.1
<b>CPE1 T(<math>s^P/\Omega</math>)</b>	$3.4668 \times 10^{-6}$	$2.0871 \times 10^{-6}$	$3.2246 \times 10^{-6}$
<b>CPE1 P</b>	0.77744	0.82918	0.81755
<b>R2 (<math>\Omega</math>)</b>	625	800.1	502
<b>CPE2 T(<math>s^P/\Omega</math>)</b>	$2.1531 \times 10^{-4}$	$1.8424 \times 10^{-4}$	$2.148 \times 10^{-4}$
<b>CPE2 P</b>	0.53352	0.57721	0.57099

The equation 5.5 shows the impedance for a constant phase element (CPE).

$$Z = \frac{1}{T(i\omega)^P} \quad (5.5)$$

Where  $i = \sqrt{-1}$ ,  $\omega$  = frequency of the AC current ( $s^{-1}$ ),  $T$  ( $s^P/\Omega$ ) and  $P$  are parameters. The resistance  $R1$  is attributable to the resistance of the electrolyte solution. The resistance  $R2$  is the resistance to the electron transfer process. The constant phase element CPE1 was used instead of a pure capacitor to take into account the deviation from an ideal double layer capacitor. This deviation is caused by the roughness of the surface of the electrodes.<sup>54</sup> The Chi-squared values for the fits are  $2.3 \times 10^{-4}$ ,  $6.6 \times 10^{-4}$ , and  $2.3 \times 10^{-4}$  for the GC, GC/Cu-MOF and GC/Cu-MOF/Au electrodes respectively, indicating good fitting procedures. As expected from the electrochemical results, the resistance to the electron transfer process ( $R2$ ) follows the order:

$$GC/Cu-MOF > GC > GC/Cu-MOF/Au$$

The MOF acts as a semi-conductor, lowering the rate of electron transfer, while the incorporation of AuNPs on the electrode makes the charge transfer faster. This finding agrees with what the CVs and chronoamperometries previously shown.

## 5.5 Reproducibility studies

### 5.5.1 Reproducibility on GC/Cu-MOF electrode preparation

Assuming the homogeneity of the  $[\text{Cu}(1,3\text{-YBDC})]\cdot x\text{H}_2\text{O}$  suspension used to drop-coating the electrodes, the amount of  $[\text{Cu}(1,3\text{-YBDC})]\cdot x\text{H}_2\text{O}$  deposited should be  $1.25 \times 10^{-2}$  mg, so that the theoretical amount of copper deposited is  $1.96 \times 10^{-3}$  mg (considering copper being 15.70% of the MOF weight). In order to investigate the reproducibility of the electrode drop-casting, four cyclic voltammograms of the GC/Cu-MOF electrode were performed in TRIS buffer 0.1M (pH 7.2). This electrolytic solution was chosen because of the stabilizing effect of chloride ions on Cu (I), so that the amount of electrons exchanged in the first reduction peak at 0.08V was known and from the area of this peak the determination of the amount of reduced Cu was possible through equation 5.6:

$$m_{\text{Cu}} = \frac{\text{reduction peak area (C)}}{n(\text{mol}) F(\text{C/mol})} AW_{\text{Cu}} (\text{g/mol}) \quad (5.6)$$

Where the reduction peak area is the area of the peak at 0.08V in the cyclic voltammetry (see Figure 5.17),  $n$  is the number of exchanged electrons which is equal to one,  $F$  is the Faraday constant, and  $AW_{\text{Cu}}$  is the atomic weight of copper.

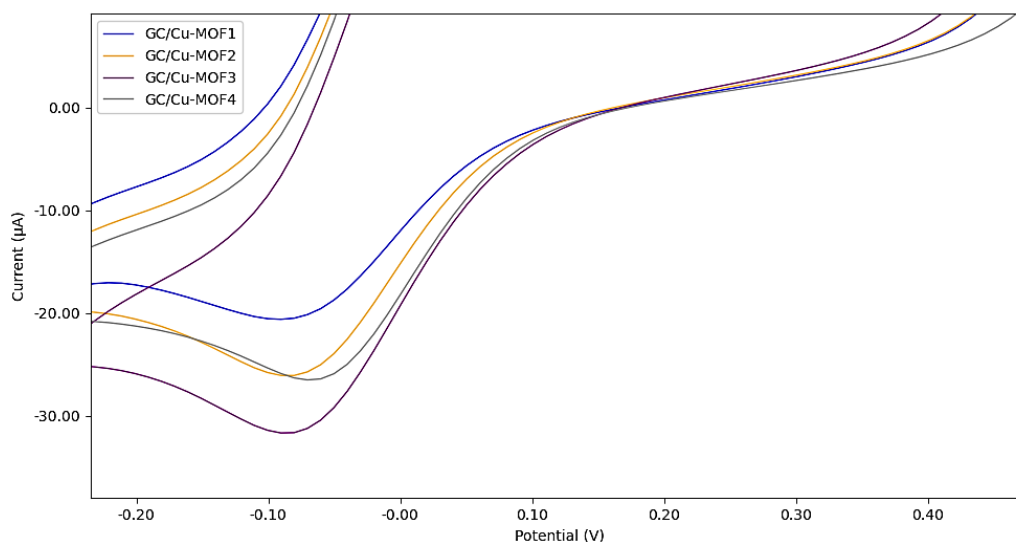


**Figure 5.17:** Reduction peak at 0.08V in the CV of the GC/Cu-MOF electrode in TRIS 0.1M (pH 7.2).

The mean area of the peak is  $5.02 \times 10^{-2}$  C so the amount of reduced Cu(II) is  $3.31 \times 10^{-5}$  mg, with an RSD% of 23.27. The discrepancy between the amount of reduced copper and the theoretical amount of copper deposited could derive from the fact that only the copper atoms very close to the glassy carbon surface are reduced. The high value of RSD% obtained could be attributed to:

- the non-homogeneity of the  $[\text{Cu}(1,3\text{-YBDC})] \cdot x\text{H}_2\text{O}$  suspension used to modify the electrode;
- the non-homogeneity of the distribution of  $[\text{Cu}(1,3\text{-YBDC})] \cdot x\text{H}_2\text{O}$  particles on the glassy carbon surface, as evidenced by the SEM characterizations of the electrodes.

### 5.5.2 Reproducibility on GC/Cu-MOF/Au electrode preparation

The nitrite oxidation signal was used for investigation by cyclic voltammetry in PBS 0.1M (pH 7.2) of the reproducibility of GC/Cu-MOF/Au electrode preparation. Five different GC/Cu-MOF/Au electrodes were tested in the presence of nitrite 5 mM and the nitrite oxidation peak currents were compared (see Figure 5.18).

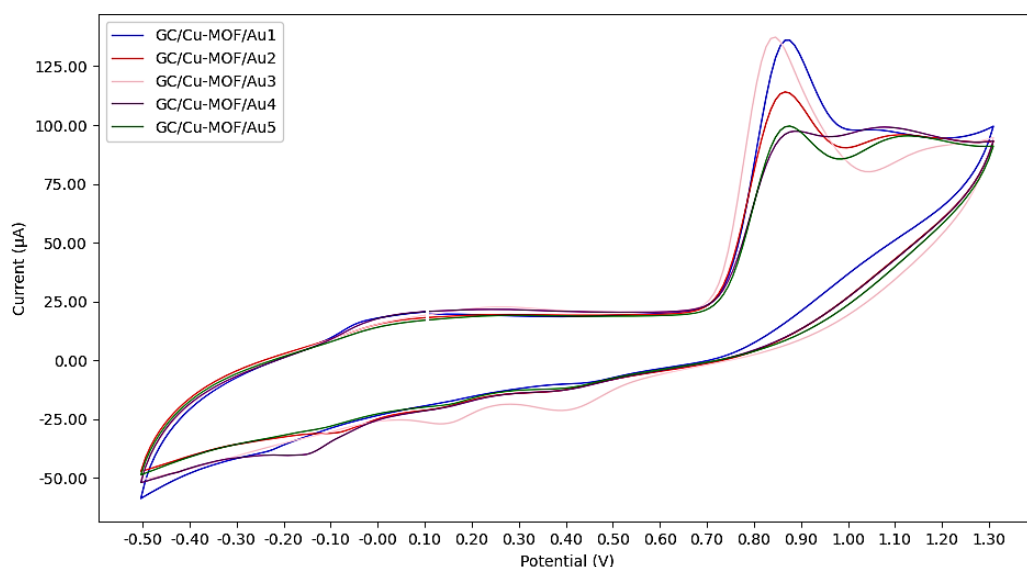


**Figure 5.18:** cyclic voltammetry of five different GC/Cu-MOF/Au electrodes in PBS 0.1M (pH 7.2) in the presence of nitrite 5 mM.

The average peak current for nitrite oxidation is  $1.18 \times 10^{-4}$  A with an RSD% value of 14.2%. The low reproducibility of the peak current for the oxidation of nitrite could be explained by the low reproducibility of the amount of gold electrodeposited on the electrode. As reported in the literature (2), the reproducibility of the modifications through the drop-coating technique

is very low due to the non-homogeneity of the deposition itself. The AuNPs electrodeposition procedure can only further decrease the reproducibility of the electrode preparation.

# CHAPTER 6

## 6 Conclusions and Future Work

The main results described in this thesis are summarized below.

- ✓ Synthesis of the novel 5-substituted organic linker 5-(2-{{(prop-2-yn-1-yloxy)carbonyl]-amino}ethoxy)isophthalic acid (abbreviated as 1,3-H<sub>2</sub>YBDC) bearing a propargylcarbamate substituent (Figure 6.1).

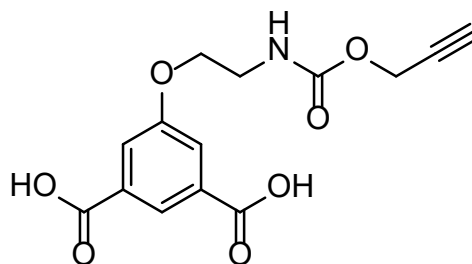


Figure 6.1: 1,3-H<sub>2</sub>YBDC

- ✓ High yield preparation of a new metal organic framework named [Cu(1,3-YBDC)]·xH<sub>2</sub>O (also abbreviated as Cu-MOF) that contains a complex network of 5-substituted isophthalate anions bound to Cu(II) centers belonging to the common paddlewheel dimeric structure with a short Cu...Cu distance of 2.633(4) Å.

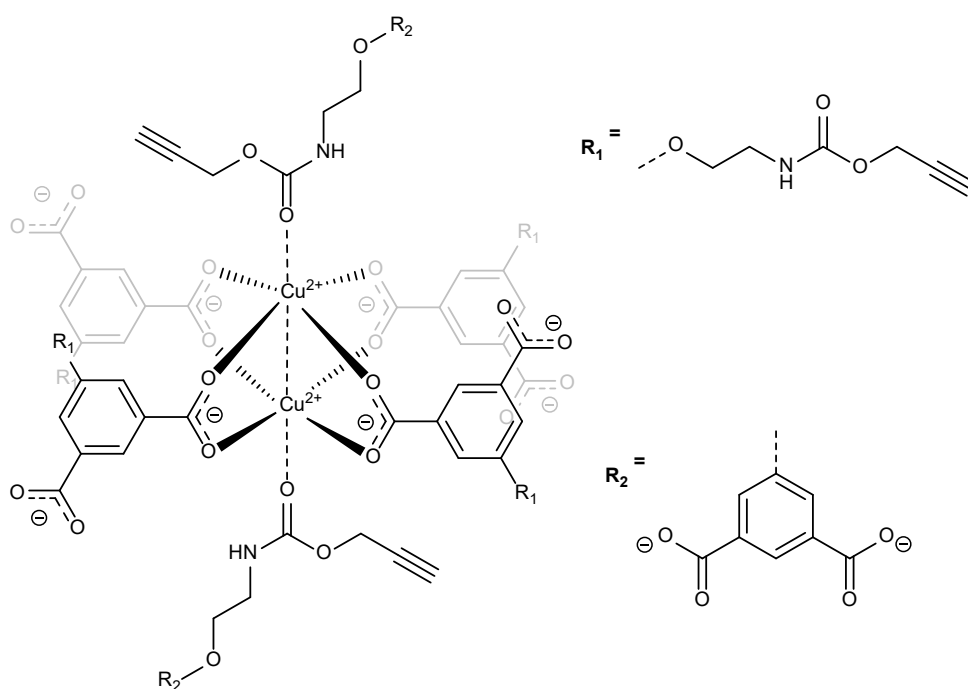


Figure 6.2: [Cu(1,3-YBDC)]·xH<sub>2</sub>O

The apical atom in the paddlewheel structure belongs to the carbonyl atom of the propargylcarbamate functionality and such extra coordination by the propargylcarbamate groups drastically reduces the MOF porosity.

- ✓ Although this evidence suggests that the internal pores of the material are available only to a small extent to host reactive gold species, this material could nonetheless be envisaged to be used for generation and anchoring of reduced gold species due to its dense, even array of propargyl-carbamate residues branching out from the MOF surface and acting as binding sites able to capture Au(III) ions and subsequently forming Au(0) clusters. Several experiments showed that Au(III) is indeed captured by the Cu-MOF, although to a small extent, being the quantity of adsorbed gold very low (ca. 0.3 wt%); however, the reduction of Au(III) occurs only partially, leading to a material in which all the gold oxidation states (III, I and 0) are present in ratios depending on the reaction conditions.
- ✓ The electrochemical properties and nitrite sensing performance of [Cu(1,3-YBDC)]·xH<sub>2</sub>O were tested through the modification of a glassy carbon electrode by drop-casting a MOF suspension directly onto the electrode (Figure 6.3).



**Figure 6.3:** GC/Cu-MOF electrode

Due to the low surface area and pore volume of the Cu-MOF, the modified electrode showed a higher peak potential and a lower peak current for the nitrite oxidation reaction than the bare glassy carbon electrode. Upon incorporation of AuNPs within the MOF through electrodeposition, the nitrite sensing performance of the modified electrode improved beyond that of the glassy carbon electrode. Cyclic voltammetry and EIS characterization of the

electrodes confirmed the semiconductor behavior of the MOF and the ability of AuNPs to compensate for that by increasing the charge transfer rate. However, due to the drop-casting technique employed in the electrode modification, they showed poor reproducibility in terms of nitrite sensing performance.

Based on these results, the future work will focus on the following issues.

- Design and synthesis of a new propargylcarbamate-functionalized ligand having the carboxylate groups more spaced apart with the aim of preparing a Cu-MOF with higher porosity.
- Improvement of the MOF-modified electrodes reproducibility by means of new modification techniques involving the in-situ growth of MOFs onto the electrode surface.

## BIBLIOGRAPHY

1. Parise C, Ballarin B, Barreca D, et al. Gold nanoparticles supported on functionalized silica as catalysts for alkyne hydroamination: A chemico-physical insight. *Appl Surf Sci.* 2019;492(March):45-54. doi:10.1016/j.apsusc.2019.05.192
2. Giorgetti M, Aquilanti G, Ballarin B, et al. Speciation of gold nanoparticles by Ex situ extended X-ray absorption fine structure and X-ray absorption near edge structure. *Anal Chem.* 2016;88(13):6873-6880. doi:10.1021/acs.analchem.6b01524
3. Fazzini S, Cassani MC, Ballarin B, et al. Novel synthesis of gold nanoparticles supported on alkyne-functionalized nanosilica. *J Phys Chem C.* 2014;118(42):24538-24547. doi:10.1021/jp507637m
4. Stock N, Biswas S. Synthesis of metal-organic frameworks (MOFs): Routes to various MOF topologies, morphologies, and composites. *Chem Rev.* 2012;112(2):933-969. doi:10.1021/cr200304e
5. Frameworks D. Zn(CN)<sub>2</sub>. Published online 1990:1546-1554.
6. Yaghi, Omar M., Kalmutzki, Markus J., Diercks, Christian S. & MJK& CSD. *Introduction to Reticular Chemistry*. John Wiley & Sons, Inc.; 2019. <https://book.global/book/5411479/d01795>
7. Low JJ, Benin AI, Jakubczak P, Abrahamian JF, Faheem SA, Willis RR. Virtual High Throughput Screening Confirmed Experimentally: Porous Coordination Polymer Hydration. *J Am Chem Soc.* 2009;131(43):15834-15842. doi:10.1021/ja9061344
8. Ockwig NW, Delgado-Friedrichs O, O'Keeffe M, Yaghi OM. Reticular chemistry: Occurrence and taxonomy of nets and grammar for the design of frameworks. *Acc Chem Res.* 2005;38(3):176-182. doi:10.1021/ar020022l
9. Jiang HL, Makal TA, Zhou HC. Interpenetration control in metal-organic frameworks for functional applications. *Coord Chem Rev.* 2013;257(15-16):2232-2249. doi:10.1016/j.ccr.2013.03.017
10. Barin G, Krungleviciute V, Gutov O, Hupp JT, Yildirim T, Farha OK. Defect creation by linker fragmentation in metal-organic frameworks and its effects on gas uptake properties. *Inorg Chem.* 2014;53(13):6914-6919. doi:10.1021/ic500722n

11. Hermenegildo García SN. *Metal-Organic Frameworks: Applications in Separations and Catalysis*. Wiley; 2018.
12. Decoste JB, Peterson GW, Schindler BJ, Killops KL, Browe MA, Mahle JJ. The effect of water adsorption on the structure of the carboxylate containing metal-organic frameworks Cu-BTC, Mg-MOF-74, and UiO-66. *J Mater Chem A*. 2013;1(38):11922-11932. doi:10.1039/c3ta12497e
13. Farha OK, Hupp JT. Activation of Metal - Organic Framework Materials. Published online 2010.
14. Lee YR, Kim J, Ahn WS. Synthesis of metal-organic frameworks: A mini review. *Korean J Chem Eng*. 2013;30(9):1667-1680. doi:10.1007/s11814-013-0140-6
15. Lv D, Chen Y, Li Y, et al. Efficient Mechanochemical Synthesis of MOF-5 for Linear Alkanes Adsorption. *J Chem Eng Data*. 2017;62(7):2030-2036. doi:10.1021/acs.jced.7b00049
16. Ameloot R, Vermoortele F, Vanhove W, Roeyfaers MJB, Sels BF, De Vos DE. Interfacial synthesis of hollow metal-organic framework capsules demonstrating selective permeability. *Nat Chem*. 2011;3(5):382-387. doi:10.1038/nchem.1026
17. He Y, Qiao Y, Chang Z, Zhou H. The potential of electrolyte filled MOF membranes as ionic sieves in rechargeable batteries. *Energy Environ Sci*. 2019;12(8):2327-2344. doi:10.1039/c8ee03651a
18. Carson CG, Brown AJ, Sholl DS, Nair S. Sonochemical synthesis and characterization of submicrometer crystals of the metal-organic framework Cu[(hfpbb)(H<sub>2</sub>hfpbb)<sub>0.5</sub>]. *Cryst Growth Des*. 2011;11(10):4505-4510. doi:10.1021/cg200728b
19. Zhang X, Chen Z, Liu X, et al. A historical overview of the activation and porosity of metal-organic frameworks. *Chem Soc Rev*. 2020;49(20):7406-7427. doi:10.1039/d0cs00997k
20. Lemire C, Meyer R, Shaikhutdinov S, Freund H-J. Do Quantum Size Effects Control CO Adsorption on Gold Nanoparticles? *Angew Chemie Int Ed*. 2004;43(1):118-121. doi:10.1002/anie.200352538
21. Jiang T, Mowbray DJ, Dobrin S, et al. Trends in CO oxidation rates for metal nanoparticles and close-packed, stepped, and kinked surfaces. *J Phys Chem C*.

- 2009;113(24):10548-10553. doi:10.1021/jp811185g
22. Mikami Y, Dhakshinamoorthy A, Alvaro M, García H. Catalytic activity of unsupported gold nanoparticles. *Catal Sci Technol*. 2013;3(1):58-69. doi:10.1039/c2cy20068f
  23. Zhong RY, Sun KQ, Hong YC, Xu BQ. Impacts of organic stabilizers on catalysis of Au nanoparticles from colloidal preparation. *ACS Catal*. 2014;4(11):3982-3993. doi:10.1021/cs501161c
  24. Kreno LE, Leong K, Farha OK, Allendorf M, Van Duyne RP, Hupp JT. Metal-organic framework materials as chemical sensors. *Chem Rev*. 2012;112(2):1105-1125. doi:10.1021/cr200324t
  25. Mao Y, Bao Y, Han DX, Zhao B. Research Progress on Nitrite Electrochemical Sensor. *Chinese J Anal Chem*. 2018;46(2):147-155. doi:10.1016/S1872-2040(17)61066-1
  26. Zhou Y, Li C, Hao Y, Ye B, Xu M. Oriented growth of cross-linked metal-organic framework film on graphene surface for non-enzymatic electrochemical sensor of hydrogen peroxide in disinfectant. *Talanta*. 2018;188(March):282-287. doi:10.1016/j.talanta.2018.05.078
  27. Shahrokhian S, Khaki Sanati E, Hosseini H. Direct growth of metal-organic frameworks thin film arrays on glassy carbon electrode based on rapid conversion step mediated by copper clusters and hydroxide nanotubes for fabrication of a high performance non-enzymatic glucose sensing platform. *Biosens Bioelectron*. 2018;112:100-107. doi:10.1016/j.bios.2018.04.039
  28. Badea M, Amine A, Palleschi G, Moscone D, Volpe G, Curulli A. New electrochemical sensors for detection of nitrites and nitrates. *J Electroanal Chem*. 2001;509(1):66-72. doi:10.1016/S0022-0728(01)00358-8
  29. Yuan B, Zhang J, Zhang R, et al. Cu-based metal-organic framework as a novel sensing platform for the enhanced electro-oxidation of nitrite. *Sensors Actuators, B Chem*. 2016;222:632-637. doi:10.1016/j.snb.2015.08.100
  30. Brauer G. *Handbook of Preparative Inorganic Chemistry*. Accademic Press; 1963.
  31. Mohideen MIH, Xiao B, Wheatley PS, et al. Protecting group and switchable pore-

- discriminating adsorption properties of a hydrophilic-hydrophobic metal-organic framework. *Nat Chem.* 2011;3(4):304-310. doi:10.1038/nchem.1003
32. Azhar MR, Hussain G, Tade MO, Silvester DS, Wang S. Electrodeposited Metal Organic Framework toward Excellent Hydrogen Sensing in an Ionic Liquid. *ACS Appl Nano Mater.* 2020;3(5):4376-4385. doi:10.1021/acsanm.0c00503
  33. Feng L, Chen Z, Zeller M, Luck RL. Polymorphs or solvates? Coordination of 3,5-dihydroxybenzoate to copper and zinc metal centers. *Inorganica Chim Acta.* 2013;394:729-740. doi:10.1016/j.ica.2012.09.036
  34. Zhang YM, Yang LZ, Lin Q, Wei TB. Preparation and crystal structure of a new Cu(II) complex of the N-ethoxycarbonyl-O-ethyl-N'-(2,4,6-trichlorophenyl)-isourea. *Transit Met Chem.* 2005;30(8):944-947. doi:10.1007/s11243-005-6245-y
  35. Prestipino C, Regli L, Vitillo JG, et al. Local structure of framework Cu(II) in HKUST-1 metallorganic framework: Spectroscopic characterization upon activation and interaction with adsorbates. *Chem Mater.* 2006;18(5):1337-1346. doi:10.1021/cm052191g
  36. Hofmann DWM. Fast estimation of crystal densities. *Acta Crystallogr Sect B Struct Sci.* 2002;58(3):489-493. doi:10.1107/S0108768101021814
  37. Briggs D. Handbook of X-ray Photoelectron Spectroscopy C. D. Wanger, W. M. Riggs, L. E. Davis, J. F. Moulder and G. E. Muilenberg Perkin-Elmer Corp., Physical Electronics Division, Eden Prairie, Minnesota, USA, 1979. 190 pp. \$195. *Surf Interface Anal.* 1981;3(4):v-v. doi:10.1002/sia.740030412
  38. Li X, Wan J, Ma Y, Zhao JR, Wang Y. Mesopores octahedron GCNOX/Cu<sub>2</sub>O@C inhibited photo-corrosion as an efficient visible-light catalyst derived from oxidized g-C<sub>3</sub>N<sub>4</sub>/HKUST-1 composite structure. *Appl Surf Sci.* 2020;510(January):145459. doi:10.1016/j.apsusc.2020.145459
  39. Barreca D, Carraro G, Gasparotto A. Cu x O - TiO<sub>2</sub> Composites (x=1, 2) Studied by X-ray Photoelectron Spectroscopy. *Surf Sci Spectra.* 2009;16(1):1-12. doi:10.1116/11.20110101
  40. Ghamari Kargar P, Aryanejad S, Bagherzade G. Simple synthesis of the novel Cu-MOF catalysts for the selective alcohol oxidation and the oxidative cross-coupling of

- amines and alcohols. *Appl Organomet Chem.* 2020;34(12). doi:10.1002/aoc.5965
41. University C. XPS analysis reference pages - Gold.  
<http://sites.cardiff.ac.uk/xpsaccess/reference/gold/>
  42. Casaletto MP, Longo A, Martorana A, Prestianni A, Venezia AM. XPS study of supported gold catalysts: the role of Au<sup>0</sup> and Au<sup>+δ</sup> species as active sites. *Surf Interface Anal.* 2006;38(4):215-218. doi:10.1002/sia.2180
  43. Chang FW, Yu HY, Selva Roselin L, Yang HC. Production of hydrogen via partial oxidation of methanol over Au/TiO<sub>2</sub> catalysts. *Appl Catal A Gen.* 2005;290(1-2):138-147. doi:10.1016/j.apcata.2005.05.024
  44. Yadav DK, Ganesan V, Sonkar PK, Gupta R, Rastogi PK. Electrochemical investigation of gold nanoparticles incorporated zinc based metal-organic framework for selective recognition of nitrite and nitrobenzene. *Electrochim Acta.* 2016;200:276-282. doi:10.1016/j.electacta.2016.03.092
  45. Ballarin B, Barreca D, Boanini E, et al. Supported Gold Nanoparticles for Alcohols Oxidation in Continuous-Flow Heterogeneous Systems. *ACS Sustain Chem Eng.* 2017;5(6):4746-4756. doi:10.1021/acssuschemeng.7b00133
  46. Loera-Serna S, Oliver-Tolentino MA, De Lourdes López-Núñez M, et al. Electrochemical behavior of [Cu<sub>3</sub>(BTC)<sub>2</sub>] metal-organic framework: The effect of the method of synthesis. *J Alloys Compd.* 2012;540:113-120. doi:10.1016/j.jallcom.2012.06.030
  47. Chen H, Yang T, Liu F, Li W. Electrodeposition of gold nanoparticles on Cu-based metal-organic framework for the electrochemical detection of nitrite. *Sensors Actuators, B Chem.* 2019;286(September 2018):401-407. doi:10.1016/j.snb.2018.10.036
  48. Luo Y-K, Song F, Wang X-L, Wang Y-Z. Pure copper phosphate nanostructures with controlled growth: a versatile support for enzyme immobilization. *CrystEngComm.* 2017;19(22):2996-3002. doi:10.1039/C7CE00466D
  49. Kozub BR, Rees N V., Compton RG. Electrochemical determination of nitrite at a bare glassy carbon electrode; why chemically modify electrodes? *Sensors Actuators, B Chem.* 2010;143(2):539-546. doi:10.1016/j.snb.2009.09.065

50. Faulkner AJB and LR. *Electrochemical Methods: Fundamentals and Applications*. Wiley; 2001. doi:<https://doi.org/10.1023/A:1021637209564>
51. Elgrishi N, Rountree KJ, McCarthy BD, Rountree ES, Eisenhart TT, Dempsey JL. A Practical Beginner's Guide to Cyclic Voltammetry. *J Chem Educ*. 2018;95(2):197-206. doi:10.1021/acs.jchemed.7b00361
52. Alam MS, Rahman MM, Marwani HM, Hasnat MA. Insights of temperature dependent catalysis and kinetics of electro-oxidation of nitrite ions on a glassy carbon electrode. *Electrochim Acta*. 2020;362:137102. doi:10.1016/j.electacta.2020.137102
53. Brunetti B DE. About Estimating the Limit of Detection by the Signal to Noise Approach. *Pharm Anal Acta*. 2015;06(04). doi:10.4172/2153-2435.1000355
54. Zhang Y, Li X, Li D, Wei Q. A laccase based biosensor on AuNPs-MoS<sub>2</sub> modified glassy carbon electrode for catechol detection. *Colloids Surfaces B Biointerfaces*. 2020;186(November 2019):110683. doi:10.1016/j.colsurfb.2019.110683